# Imitating human motion using humanoid upper body models

Chioniso Dube



**Thesis**
Presented for the degree of
**Master of Science in Engineering**
In the
Department of Electrical Engineering
University of Cape Town

March, 2012

**Declaration**

I know the meaning of plagiarism and declare that all the work in the document, save for that which is properly acknowledged, is my own.

**Abstract**

This thesis investigates human motion imitation of five different humanoid upper bodies (comprised of the torso and upper limbs) using human dance motion as a case study. The humanoid models are based on five existing humanoids, namely, ARMAR, HRP-2, SURALP, WABIAN-2, and WE-4RII. These humanoids are chosen for their different structures and range of joint motion.

Human motion capture data is transfered to the humanoid upper body models by scaling the human motion to the humanoid dimensions and mapping the motion to the number of joints of each humanoid. In order to account for missing data from the data set used, a method to estimate the missing data for the sternum location is developed in this thesis. The sternum location estimation is shown to provide a good estimate to the actual sternum location. Inverse differential kinematics, employing the damped least squares jacobian and a joint limit weighing matrix is used to transfer human motion capture data to the humanoids. To determine the effects of self collisions, a self collision detection scheme that models the humanoid body using elliptical capsules is formulated in this thesis. The self collision detection scheme is shown to be simple while providing a good representation of the humanoid form.

The error between the desired humanoid posture and the actual posture attained is used to determine how well each humanoid imitates the human motion. The error distributions, the maximum and minimum error regions, and the mean and standard deviation of the error for each joint of each humanoid are compared. Factors such as the number of joints, the range of joint motion, self collisions of the limbs with the body, and location of the joints are investigated to determine their effects on the motion imitation results. It is found that the waist joints and shoulder girdle joints are highly important for human motion imitation of humanoid upper bodies.

**Acknowledgments**

My thanks to my supervisors, Mohohlo Tsoeu and Jonathan Tapson, for their guidance, advice and insights.

With thanks to the CSIR for sponsoring my Masters studies. Thank you to everyone at MIAS who took an interest in my work. Thanks to Ajith Gopal for organising the motion capture of the dance. I am also grateful to all those not mentioned, who have helped me in various ways throughout the course of this thesis.

I am thankful to my parents and siblings for their boundless support and encouragement. Thanks to my friends for their moral support. I thank my husband for his invaluable help, love, and confidence in me.

To my wonderful husband Sepo and our lovely daughter Luyando, I dedicate this thesis.

# Contents

# List of Figures

# List of Tables

# Chapter 1

# Introduction



The idea of a dancing robot conjures up images of a stiff, mechanical being performing angular, abrupt movements. Can a robot move with the grace and rhythm of a human dancer? Humanoid robots such as QRIO [1] [2] and HRP-2 [3] have shown that it is possible for robots to attain such flowing dance forms. This thesis aims to use humanoid upper body models to imitate human dance movements. Motion imitation results of the humanoids will be compared to determine which of the humanoid upper body structures is best able to mimic the human motion.

## 1.1 The importance of humanoid robots

The next question would surely be; what use is it to build a complex, expensive piece of machinery such as a humanoid robot and then make it dance? An obvious answer would be for entertainment. But aside from what value a performing robot may have, making a humanoid dance, indeed building a humanoid robot itself has numerous benefits in other applications. These applications include; the development of service robots, health care robots, household robots, and the development and analysis of prosthetic devices. Health care robots that help rehabilitate stroke patients are in use [4], [5], [6], [7]. Service robots are in development in various institutes [8], [9], [10], [11], [12], [13]. Robotic arms such as the Manus ARM [14], [15] and KARES [16] are designed to be mounted onto wheelchairs to assist the occupant to perform tasks that would normally be outside the range of the occupants abilities.

Humanoid robots are chosen for these applications because the anthropomorphic shape and range of motion of humanoids is convenient for human environments such as homes and hospitals, since such environments are specifically designed for the human structure and motion. The lower body of the humanoids provides the robot with the ability for locomotion through human environments while the upper body allows the humanoid to interact with the environment, the people and objects within it. The arm in particular is probably one of the most useful parts of the human or humanoid body as it is the arms that are involved in performing the actual tasks. The design of humanoid arms and their motion characteristics is thus of great importance. The motion of the entire upper body affects the arm positioning and orientation and so the upper body as a whole is studied in this thesis.

Service, health care and household robots are required to perform a variety of tasks. The humanoid upper body therefore has to encompass a wide range of motion abilities. The benefits of making a humanoid robot perform a dance as a case study in humanoid motion, stem from the range of motions possible through dance. Dancing, in general, has most elements of human movement needed for various tasks and activities. Dance contains simple and intricate movements, as well as different motion and speed patterns, and differing degrees of accuracy in positioning. A robot that has an anthropomorphic structure and can copy human motion such as dance would thus be able to fit in and function well in a human space, for human assistive tasks. This thesis therefore investigates the motion capabilities of five existing humanoid robot upper bodies through modeling the upper body structures and transferring human dance motion to the humanoid upper body models.



### 1.1.1 Modeling humanoid robot upper bodies

By definition, humanoid robots mimic the human form, size, and range of motion. In the human body, the muscular, skeletal and joint configurations determine the types and range of motion possible for each body segment. Muscles provide the motion of the skeleton and joints, while the brain and nervous system control the actual motion. In a humanoid robot, actuators and transmission perform the function of human muscles, providing and transmitting the forces needed to move the robot. The joint and linkage structure performs the function of the human skeleton and joints, their configuration and the number and range of the joints determining the possible range of motion for the robot. Computers, electronics and

control systems of the humanoid perform the function of the brain and nervous system, providing the commands necessary for the robot to execute the desired motion.

All these elements affect the upper body motion to varying degrees, however this thesis focuses on the models of the joint and linkage structure as the main contributors to the upper body's motion capabilities. The models incorporate the number of joints, the configuration of links and actuators, and the effects of physical constraints such as joint limits and self collisions of the arm with the body on the overall range of motion of the arm and torso. Velocity and acceleration profiles of the dance motion, which are determined by the capacity of the humanoid actuators, are not investigated. The hand and fingers are vital for manipulation and interaction with objects. However, object manipulation is outside the scope of this thesis. Thus, while the motion required to position the hand will be studied, the different hand and finger models and their motion will not be studied.

To generate human motion for the humanoid robot to imitate, a popular method used in robotics and computer graphics is human motion capture. Through human motion capture, the motion of the body and limbs is recorded through tracking of motion markers, and the motion capture data is then transferred to the humanoid robot. Motion capture has been widely used to imitate human motion for animation, for human movement understanding, sports science, in addition to generating motion for robots. [17] [18] [19] [20]

Despite the fact that humanoids attempt to mimic the human body, there are still huge differences between humanoids and humans. Motion capture of humans therefore has to be processed to fit the humanoid structure [17]. The process of transferring human motion data to different humanoid upper bodies is thus also investigated. The transfer process results in a range of humanoid joint angles that attempt to match the human posture at each time instant in the motion capture of the human motion. The resultant position of each link of the humanoid is compared to the desired human configuration. The distance between the desired and actual positions gives an indication of how well the humanoid imitates the human motion. Factors such as the number and position of joints, the motion limits of the joint and self collisions are investigated to determine how they affect the resultant robot motion.

## 1.2 Thesis objectives

This Master's thesis focuses on the modeling of the upper body structures of humanoid robots to follow human dance motion obtained from human motion capture. The five humanoids chosen are ARMAR, HRP-2, SURALP, WABIAN-2, and WE-4RII. They have different structured waist and shoulder joints and have different ranges of joint motion. The aim is to determine which humanoid upper body structure is best suited for human motion imitation. The objectives of this thesis are therefore to:

1. Model five different humanoid robot upper body structures,
2. Use the humanoid upper body models to imitate a captured human dance,
3. Compare the motion imitation abilities of the humanoid upper body models.

### 1.2.1 Research gap

Few studies, to date, deal with motion imitation performance of humanoids. Studies typically investigate the capabilities and limitations of individual humanoids without any comparative study. For instance a humanoid robot was used in [17] to mimic the actions of the song 'I'm a little teapot' and the limitations of the particular humanoid's performance were discussed. The dance performance of a Sarcos humanoid was discussed in [18]. HRP-1S was used by in [19] [20] in their motion transfer of a traditional dance.

While these studies highlight limitations of certain humanoids, they do not provide a comparison with other humanoids or an analysis on which of the limitations are the most significant. This thesis therefore undertakes a comparative study of the human motion imitation of five different humanoid upper bodies in order to contribute to this field. Models of each humanoid will be used to simulate the humanoid motion.

Constraints such as self collision are an important input into humanoid workspace and motion models. Existing self collision detection schemes either pose numerous challenges in implementation and have a large computational cost or do not provide a good representation of the humanoid bodies. In this thesis a new collision detection scheme is developed that aims to provide a good representation of the humanoid body while being simple to implement. Transferring human motion to

humanoids requires a sufficient number of motion capture markers. However, in some cases, relevant motion capture markers are missing from the data. A method to estimate missing sternum motion markers is therefore developed in this thesis.

### 1.2.2 Thesis structure

To model the humanoid robot upper body and imitate human motion, it is important to understand the human and humanoid upper body structures. This thesis begins with an overview of the main features of the human upper body and human upper body movements (Chapter 2), as these movements provide the context from which humanoid robots stem. Chapter 2 describes the type and range of upper body movements and highlights the importance of the shoulder girdle to human arm movements. Humanoid robot upper bodies that currently exist are then investigated in terms of their structure and range of motion (Chapter 3). The main features, advantages and disadvantages of two commonly found arm structures, parallel and serial arms, are described and compared to the human arm. The existing methods of transferring human motion to humanoids are then described and motion imitation attempts of some individual humanoid robots and their results are discussed.

Modeling of humanoid upper bodies is discussed in Chapter 4. The humanoid pose and motion modeling used in this thesis is described as well as motion transfer of human motion. A self collision detection scheme for humanoid robots is developed. Chapter 5 describes the humanoid robots and the human motion capture data of the dance used in this study. A technique for estimating relevant missing motion data from the human motion capture for transfer to the humanoid is developed. Comparisons of the motion imitation capabilities of the different humanoid upper bodies are carried out in Chapter 6. The conclusions on the findings and recommendations for future work are presented in Chapter 7.

# Chapter 2

# The Human Upper Body Anatomy and Movements



At the basis of humanoid robotics is the goal of imitating the human structure and performance. It should be noted, however, that in the design of a humanoid robot, the aim is not to replicate the human but to gain an understanding that allows one to imitate the human's functionality and the basic appearance. In view of this, the important anatomical features and movements of the human upper body are examined in this chapter.

## 2.1 Human upper body anatomy

The human upper body is made up of the upper limb and the torso. The human arm, along with the shoulder girdle and hand, forms part of the human upper limb shown in figure 2.1. The upper limb is a complex and highly mobile structure capable of a wide range of movements. The torso starts at the sacrum and is made up of the rib cage and the highly flexible vertebral column, also referred to as the spine. The upper body consists of a skeletal structure of bones, which act as levers, connected together by joints. Joints are supported and reinforced by ligaments and muscles (See figure 2.2). Muscles, attached to the bones via tendons and arranged in a complex network, actuate the joints; producing various movements of the upper body segments. For smooth and efficient motion of the upper body to take place, interaction between the various parts of the upper upper body is necessary. [21] [22]

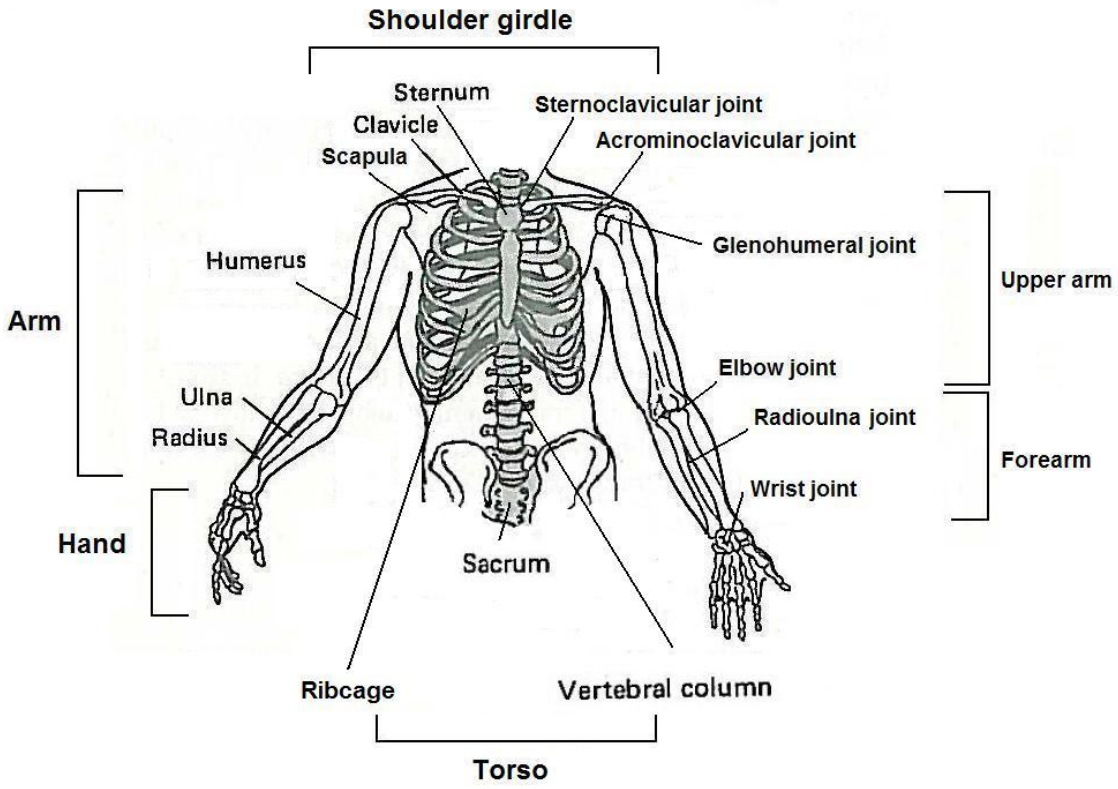


Figure 2.1: Human upper body skeletal and joint anatomy, showing bones and joints at the arm, shoulder girdle and spine [22].

### 2.1.1 Human upper body skeletal structure

First in the upper limb is the shoulder girdle which consists of the clavicle and scapula bones (See figure 2.1). The clavicle is joined to the sternum by the streno-clavicular joint. This joint, incidentally, forms the only point of connection of the upper limb to the thorax, providing the arm with its high mobility. The scapular is not directly connected to the thorax but 'floats' on muscles that form the scapulothoraic interface. The scapula is joined to the clavicle by the acrominoclavicular joint. [21] [22]

The arm itself is made up of two segments, the upper arm and the forearm. The upper arm begins at the glenohumeral joint, which links the arm to the shoulder girdle. The glenohumeral joint is a ball and socket joint, connecting the scapular bone of shoulder girdle and the humerus bone of the upper arm. The glenohumeral joint is made up of the spherical head of the humerus and the glenoid cavity of the scapular. [21] [22]

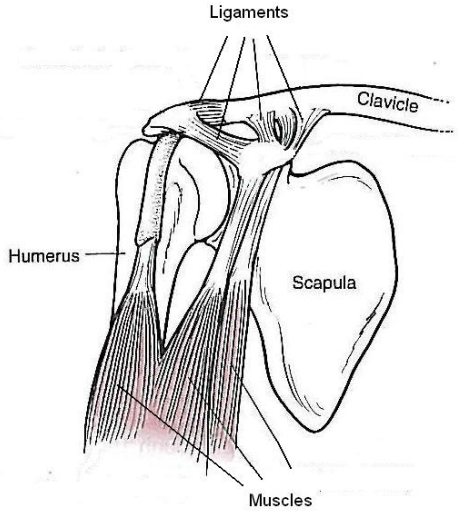


Figure 2.2: Muscles, ligaments and other soft tissue supporting the glenohumeral joint [21].

The forearm begins at the elbow joint, followed by the radius and ulna bones, and ends with the wrist joint. The elbow joint is made up of two joints, a hinge joint between the humerus and ulnar, and a restricted ball and socket joint between the humerus and radius. However because of the way ligaments restrict the ball and socket joint it behaves as a hinge joint and so the elbow as a whole can be described as a hinge joint. The radioulnar joint consists of two pivot joints between the radius and the ulnar bones. The wrist or radiocarpal joint is an ellipsoid joint between the radius and two carpals. [21] [22]

The rib cage is made up of, on average, twelve ribs on either side with joints that allow very little motion. It provides protection for the chest organs and support for the shoulder girdle. The spine is made up of twenty four vertebra, separated by spinal discs and connected by facet joints that allow a small amount of relative movement between the bones. The spine not only allows movement of the torso but provides support for the entire body and protection for the spinal cord. [21] [22]

Average dimensions of the male upper limb segments taken from anthropometric texts [23] are shown in table 2.1.

Table 2.1: Average human upper limb dimensions [23].

| Segment | Average value (mm) |
|---|---|
| Upper arm length | 365 |
| Forearm length | 270 |
| Shoulder girdle width | 465 |
| Hand length | 190 |
| Upper body length | - |
| Upper arm circumference | 316 |
| Wrist circumference | 167 |
| Forearm circumference | 265 |
| Shoulder girdle depth | 270 |
| Hand width | 85 |
| Chest depth | 250 |
| Abdominal depth | 270 |

### 2.1.2 Human upper body muscles

Muscles provide the actuation of the bones and joints of the upper body. The muscles can be attached either directly to the bones or attached to the bones by tendons. Muscles of the glenohumeral joint pass either from the chest or the scapular to the arm. Those of the elbow are located at the upper arm and those of the wrist are located at the forearm. Some muscles have a large base on the torso or scapular but meet at a relatively small point on the arm bone, for example the pectoralis major is fan shaped from the chest, converging to a flat tendon on the humerus. [21] [22]

Muscles provide actuation by contracting, decreasing their length while providing a pulling force, and relaxing returning to their original length. Since muscles can only providing a pulling force, two or more muscles that can pull in different directions are needed for a joint to be able to move. Such muscle groupings are termed antagonistic muscles. Some muscles contract while others relax to generate the required motion. For example, as shown in figure 2.4, when the bicep contracts and the triceps is relaxed, the elbow joint is flexed. When the triceps is contracted and the bicep relaxed, the elbow joint is extended. When both the triceps and bicep contract, the elbow is stiff and does not give easily. When both the muscles relax the arm is compliant - the opposite of stiff and the arm gives under force. Compliance is an important human characteristic in terms of safety and interaction with objects. [21] [22] [24] [25]

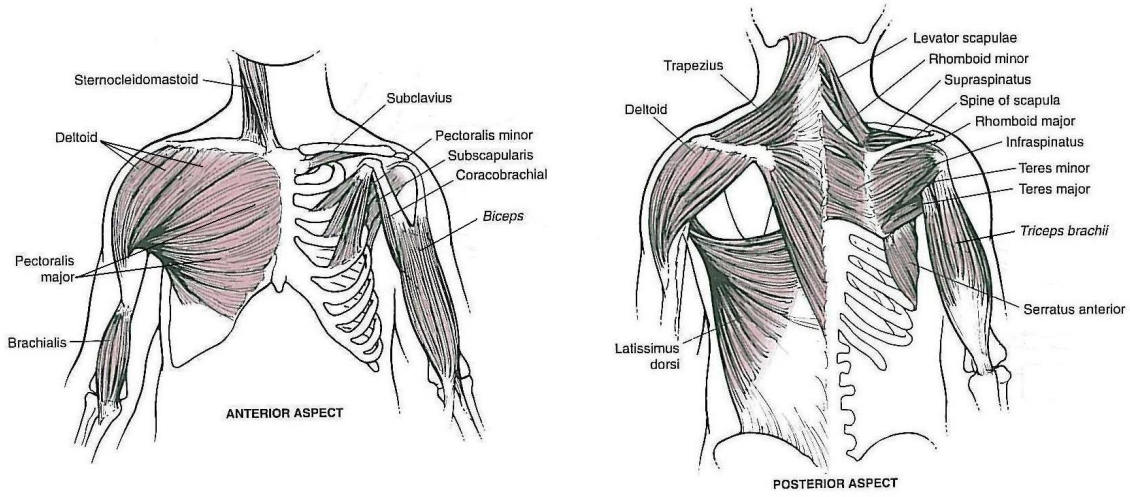


Figure 2.3: Human upper limb muscles [21].

Figure 2.5 shows the action of various arm and shoulder girdle muscles. A muscles or set of muscles can be involved in producing more than one different movement of a joint. For example, the rotar cuff muscle group and deltoid produce several movements of the glenohumeral joint. At the same time, some movements of a joint may require different muscle sets. For example, rotation of the arm in one direction, the infraspinatus and teres minor are used but rotation in the opposite direction is produced by the sub-scapularis, latissimus dorsi, teres major, and portions of the pectoralis major. [21]

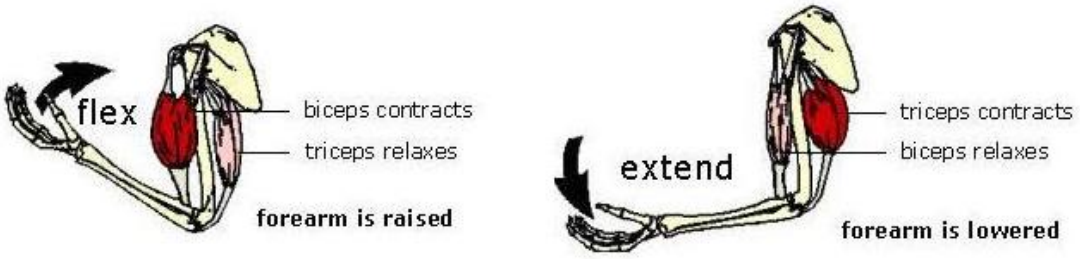


Figure 2.4: Antagonistic action of the forearm muscles [24].

In some cases, for different speed of a particular motion, different sets of muscles are used. For lifting the arm, the rotar cuff applies a force to keep the humeral head stabilized while the deltoid applies a force to raise the arm. If the arm is slowly lowered the same muscles are used. However, for rapid lowering, the latissimus dorsi, teres major and the sternal portion of the pectoralis major are used. [21]

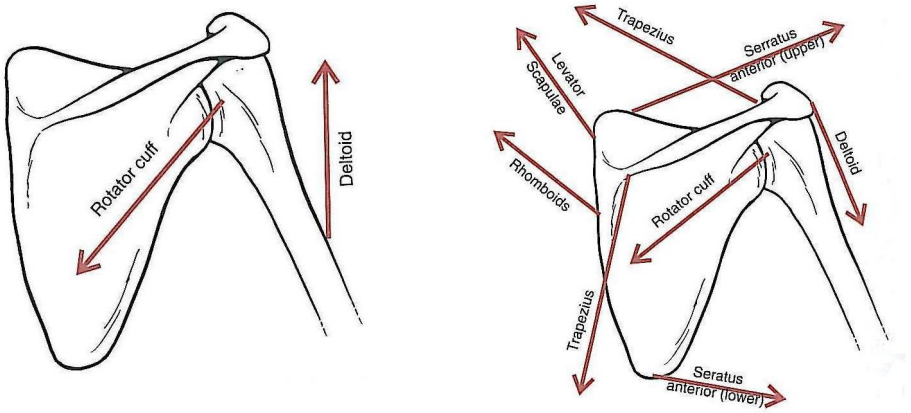


Figure 2.5: Action of human upper limb muscles. For rising and lowering the arm, the rotor cuff muscles and the deltoid work together. To keep the arm in resting positions various arm and shoulder girdle muscles pull in different directions [21].

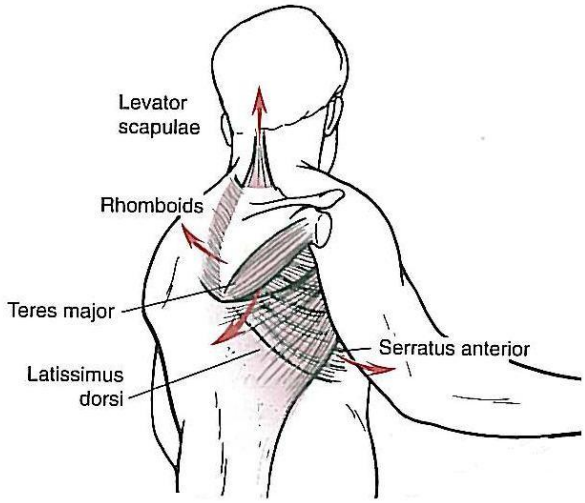


Figure 2.6: Action of human upper limb muscles. The latissimus dorsi, teres major and the sternal portion of the pectoralis major are used for quick lowering of the arm [21].

## 2.2 Movement classification

Any movement of a human upper body is made up of combinations of basic arm joint, shoulder girdle joint and spine joint movements. Each mobile joint in the human upper body allows for the movement of its associated body segment. Basic

movements of the upper body can be classified according to the joint that provides the motion, the reference planes axis, and positions of the human body. In order for the various movements of the human body to be classified, they are measured in reference to some standard starting position and reference plane. Starting or neutral positions used in kinesiology and biomechanics are shown in figure 2.7 and figure 2.8. These positions are the anatomical and the fundamental standing positions. [21]

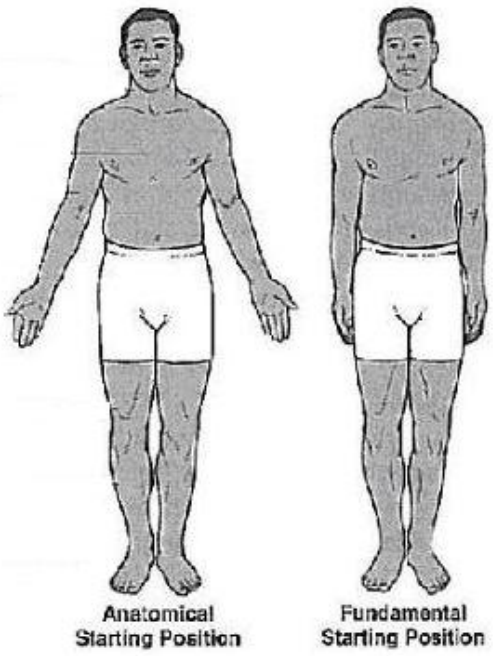


Figure 2.7: Anatomical and fundamental reference starting positions for human movement measurements [21].

In the anatomical standing position, the body is in an erect stance, head is facing forwards, arms at the side of trunk, elbows fully extended, palms facing forward, legs together, feet facing forward. This position is usually accepted as the point of reference for movements of the forearm hands and fingers. In the fundamental standing position, the body is erect with feet slightly separated and parallel, the arms are in a relaxed posture at the sides with palms facing toward the trunk. This position is usually accepted as a point of reference for all the body segment movements except those of the forearm. [21] [22]

The motion reference planes are the sagittal, transverse and frontal planes and are shown in figure 2.8. The transverse plane divides the body in half - top and bottom. The frontal plane divides the body into left and right halves and the sagittal plane

divides the body into front and back halves. Some movements, while able to occur in any plane, are measured with reference to a particular plane. Movements of the glenohumeral joint are measured in particular body planes. [22]

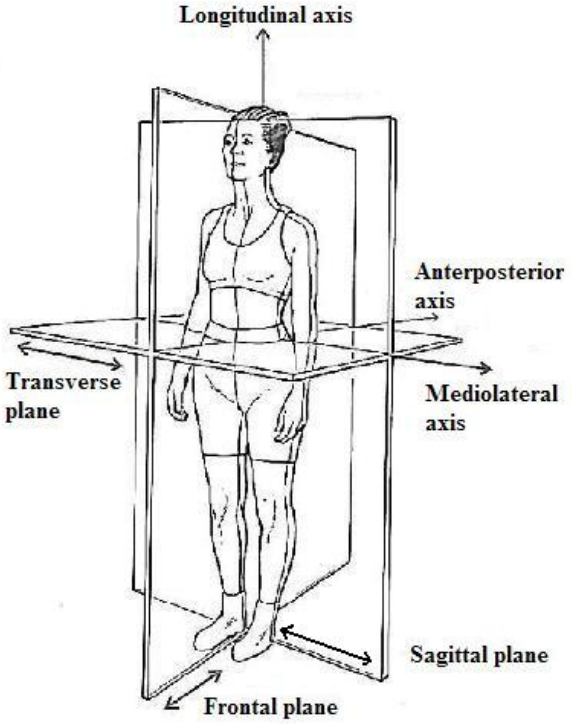


Figure 2.8: Human body reference planes and axis [22].

### 2.2.1 Human arm movements

In total, the human arm has seven degrees of freedom (DOFs) or types of movements. DOFs can be rotations about the x, y, z axis of joints and translations along these axis. The arm DOFs are found at the glenohumeral joint, the elbow joint, the radioulna joint and the wrist joint. Each DOF or type of movement is described fully by two names, one corresponding to the positive movement away from the neutral position and the other corresponding to the negative movement. Antropomophic data texts provide values of human arm movements obtained from sample population sets.

### Glenohumeral joint degrees of freedom

At the glenohumeral joint, movements occur in three rotational directions, giving it three DOFs that position and orient the upper arm. These movements have axis perpendicular to each other and are measured from the fundamental starting position. The movements are shown in figure 2.9. Movements of the glenohumeral joint are; inward and outward rotation, flexion and extension, and adduction and abduction. Adduction and abduction are usually measured in the frontal plane and flexion and extension in the saggital plane. Inward and outward rotations, as shown in figure 2.9 are most easily observable when the elbow is flexed at $90^o$ while the arm is at $90^o$ abduction. [21] [22]

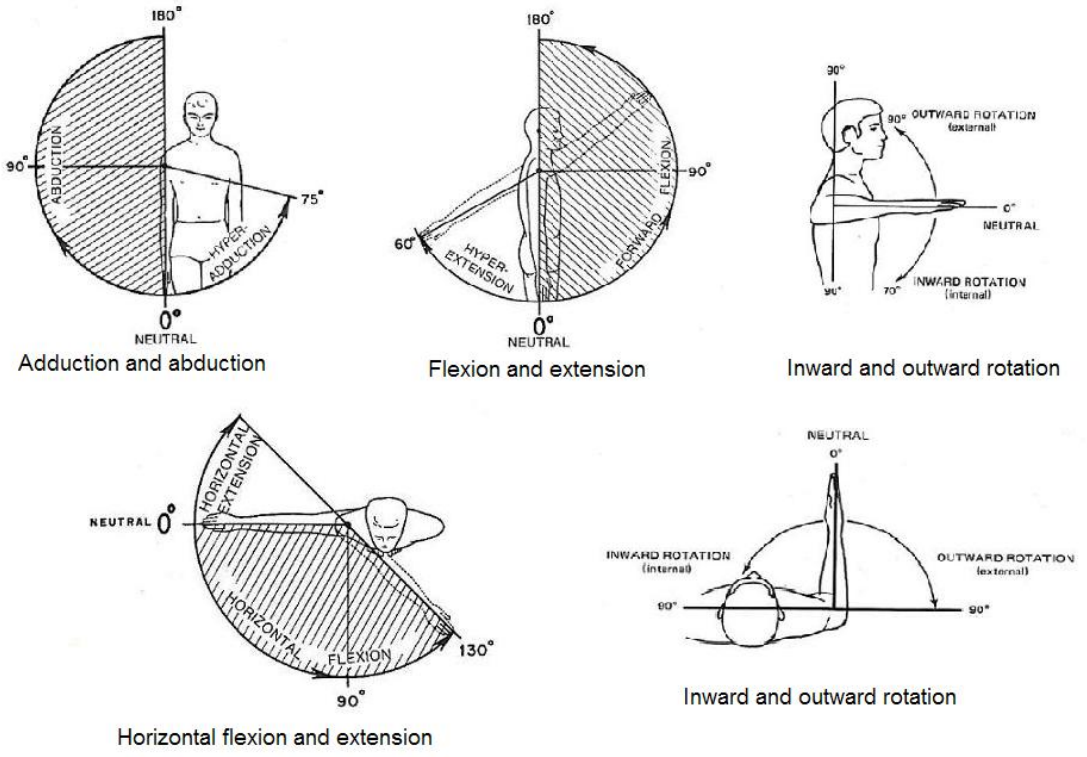


Figure 2.9: Human glenohumeral joint movements [22].

While the glenohumeral joint only has three DOFs, at different positions some movements have special names, for instance horizontal flexion and extension which occurs in the transverse plane when the arm is at $90^o$ abduction. Note how the range of this movement in the transverse plane differs from the range of the same movement in the sagittal plane. This is due to the complex arrangement of muscles, bones and joints. [21] [22]

### Elbow and radioulna joint degrees of freedom

The elbow and radioulna have the function of positioning and orienting the forearm. The elbow joint allows one DOF motion of the forearm called flexion. This is measured from the anatomical starting position. In most people extension of the elbow is not possible or else very small. Figure 2.10. The radioulna joint allows the forearm to move through one DOF, pronation and supination. Pronation and supination are measured from the fundamental starting position. The movement of the radioulna joint is shown in figure 2.10. [21] [22]

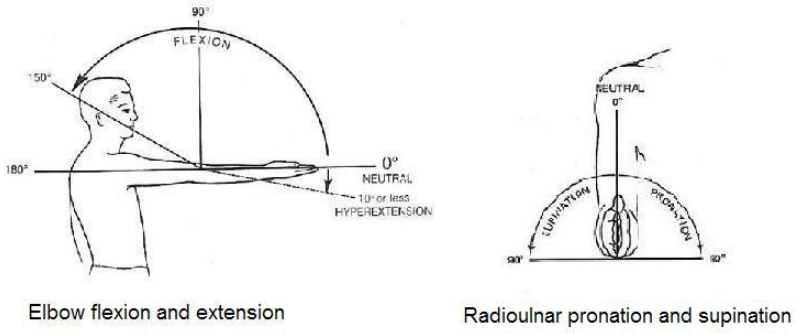


Figure 2.10: Human elbow and radioulna joint movements [22].

### Wrist joint degrees of freedom

The final DOFs of the arm are at the wrist joint and these DOFs position the hand. At the wrist, the movements are flexion and extension and abduction and adduction. These movements are illustrated in figure 2.11. [21] [22]

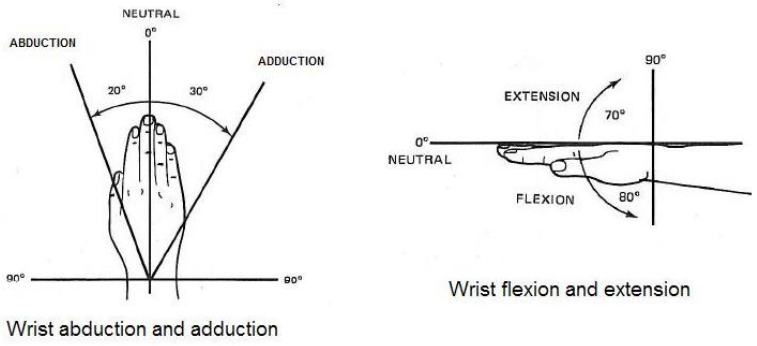


Figure 2.11: Human wrist joint movements [22].

### 2.2.2 Human shoulder girdle movements

The overall positioning of arm is also affected by the shoulder girdle. Indeed, some arm positions would not be possible without involvement of the shoulder girdle. Strictly speaking, the flexion and abduction movements of the humerus are not dependent on the action of the glenohumeral joint alone. After $30^o$ of flexion and $45^o$ of abduction, to continue raising the arm to its full $180^o$ flexion or abduction, the action of the glenohumeral joint is aided by the shoulder girdle as shown in figure 2.12. This action of the humerus, glenohumeral joint and shoulder girdle is called the scapulohumeral rhythm. Other movements of the shoulder girdle also affect the positioning of the humerus by changing the position of the glenohumeral joint and therefore changing the center of rotation of the humerus as shown in figure 2.13. This enables a greater reach of the arm segments. [21] [22]

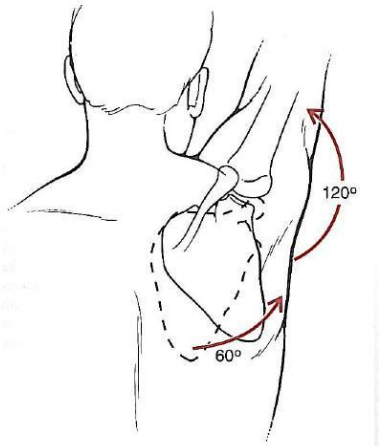


Figure 2.12: Scapulohumeral rhythm - Interaction between the glenohumeral joint and the shoulder girdle movements [21].

#### Human shoulder girdle degrees of freedom

Both the acrominoclavicular and sternoclavicular joints in the shoulder girdle have three DOFs each. These DOFs do not act independently of each other but they combine to form four types of movement of the shoulder girdle. Of these types of movement, upward tilt only occurs because of glenohumeral extension; and upward and downward rotation only occur in conjunction with glenohumeral flexion and extension or abduction and adduction. The remaining two movements of the shoulder girdle, protraction and retraction and elevation and depression,

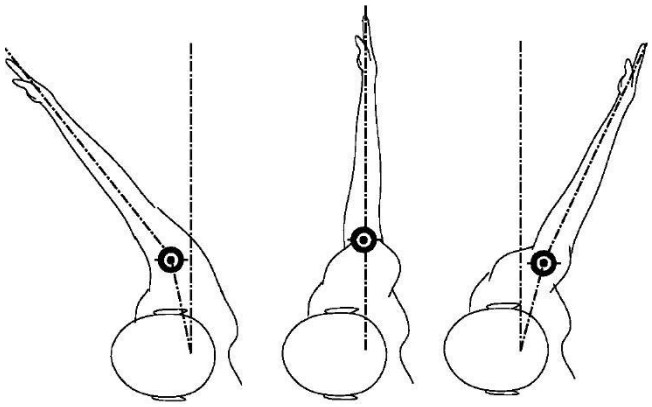

Figure 2.13: Shoulder girdle effect on the upper arm position [26].

are distinct and independently affect the glenohumeral joint position. Shoulder girdle movements are shown in figure 2.14. The movements are best illustrated by changes in the position of the scapular. The initial and final positions of the scapular are represented by a dotted and solid line respectively. [21] [22]

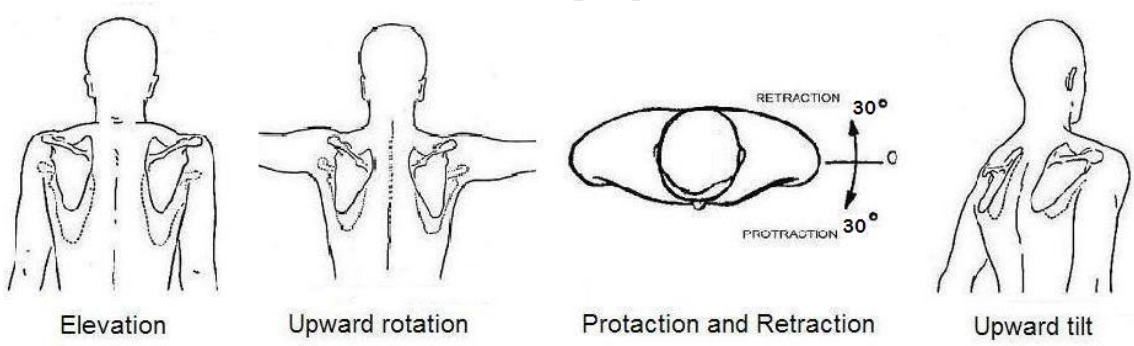


Figure 2.14: Human shoulder girdle movements [22].

### 2.2.3 Human spine movements

Movements of the spine occur at each vertebra of the spine combined to form three DOFs. Spine flexion is the forward bending of the body along the sagittal plane. Lateral flexion is a bending motion to the right or left along the frontal plane. Rotation of the spine occurs about the longitudinal axis of the body. These movements are illustrated in figure 2.15 . [22] [21]

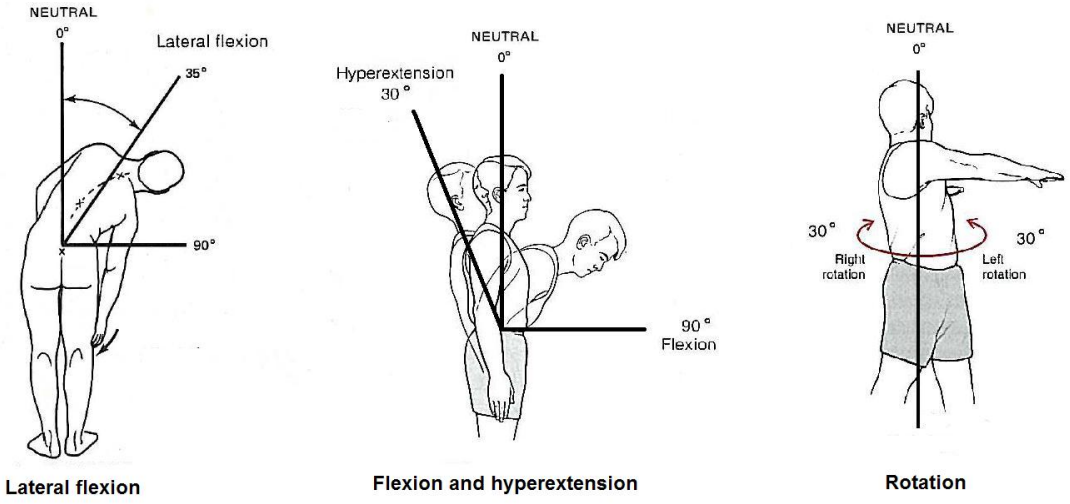


Figure 2.15: Human spine movements [22] [21].

## 2.3 Summary

The human upper body anatomy is made up of bones, joints and is actuated by antagonistic muscles. While human arm has seven DOFs, for smooth motion of the arm, the action of the shoulder girdle is important. The shoulder girdle aids the glenohumeral flexion and abduction movements of the arm and also changes the center of rotation of the humerus. The complex network of muscles in the arm and shoulder girdle allows joints to be moved by the same or different muscle groups for different types, stages and speeds of motion. Due to the arrangement of the muscles, joints and bones, the range of movement of the arm joints can differ at different arm positions or configurations. The spine is made up of numerous joints each with a small range of motion that combine to form three DOFs.

# Chapter 3

# Humanoid Upper Bodies and Motion Imitation



When modeling a dancing humanoid robot, the standard against which the resulting robot motion is measured is ultimately the human motion itself. The important aspects of the human upper body were highlighted in chapter 2. This chapter goes on to examine how humanoids attempt to mimic the important anatomical and functional features of the human upper body. The motion capabilities of the humanoid robot are compared to that of humans. Finally, motion imitation through motion capture is discussed along with a comparison of how well humanoids are able to imitate human movements.

## 3.1 Humanoid upper body structures

The human torso, arm and shoulder girdle are complex mechanisms which would be hard to model and replicate in their entirety. In fact, most humanoids have no shoulder girdle mechanism at all due to its particular complexity. Yet the upper body has to be designed and modeled well enough for the robot to still be able to mimic the full range of human motions while keeping the models as simple as possible. Two different types of humanoid design typically exist; serial structured designs and parallel structured designs.

### 3.1.1 Humanoid arms

Humanoid arm designs receive particular attention because of the importance of the arm in performing tasks. There are a number of different ways in which arms are designed resulting in a wide range of different motion abilities.

#### Serial humanoid arms

Due to their relatively simple design and ease of modeling, serial arm structures are the most commonly found type of arm in humanoid robotics. With serial structured arms, one actuator is assigned to one degree of freedom (DOF). (For convenience, throughout this thesis, the joint that provides each individual DOF of motion will be named using the forward motion only, e.g. the glenohumeral flexion joint). Thus a single human joint with more than one DOF then becomes a cluster of one DOF joints arranged in series. This allows the arm to replicate the types of motion the human arm is capable of without the complexity of the human muscle and joint actuation system. Figure 3.1 shows the structure of a typical seven DOF humanoid arm. The actuators found in serial humanoid robot arms are typically electric DC motors with either gear or cable drives providing rotational motion rather than antagonist pulling action. This is with the exception of Pneumatic Artificial Muscle (PAM) actuated arms where each one DOF joint is actuated by an antagonistic muscle pair.

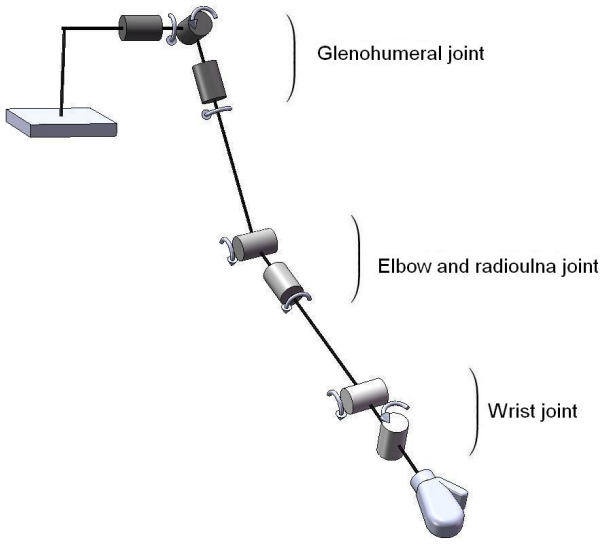


Figure 3.1: Structure of a seven DOF serial humanoid arm.

Humanoid robots that have a serial arm structure are shown in figure 3.2. ASIMO [27], HRP-2 [28], ARMAR [29] [30], Saika-4 [31], HUBO [32], MIA arm [33], TELESAR II [34], Robonaut [35], and the Barret WAM arm [36] [37] all have either six or seven DOF serial arms starting at the glenohumeral joint to the wrist joint. The DOF difference being in the number of DOFs at the radioulna and wrist joint. The whole sensitive arm [38] has four DOFs having no radioulna or wrist.

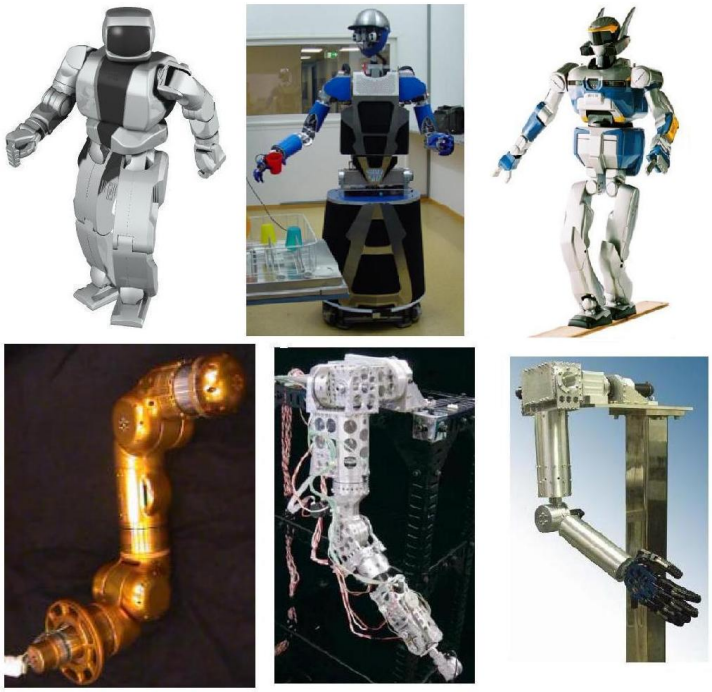

Figure 3.2: Humanoid arms with serial kinematic structures. From left to right starting from top row, HUBO [32], ARMAR [29], HRP [28], Robonaut [35], TELESAR II [34], Whole sensitive arm [38].

A disadvantage of serial structured arms is that splitting a three DOF joint, such as the glenohumeral joint, into three one DOF joints results in a singularity. At a singular position, it is impossible to generate arm velocities in certain directions. The singularity at the glenohumeral joint occurs when two degrees of freedom, flexion and extension and inward and outward rotation, line up thus one DOF is lost. Motions like horizontal flexion and extension become impossible. See figure 3.3 [39]. The lining up happens when the arm is at 90 degrees abduction. ASIMO [27] and WE-4RII [40] address this singularity by raising the shoulder mounting angle for the flexion axis by a few degrees. (See figure 3.3). This raises the singularity point out of the normal range of everyday movement of the robot. In terms of control, reaching the singular point is avoided in the software.

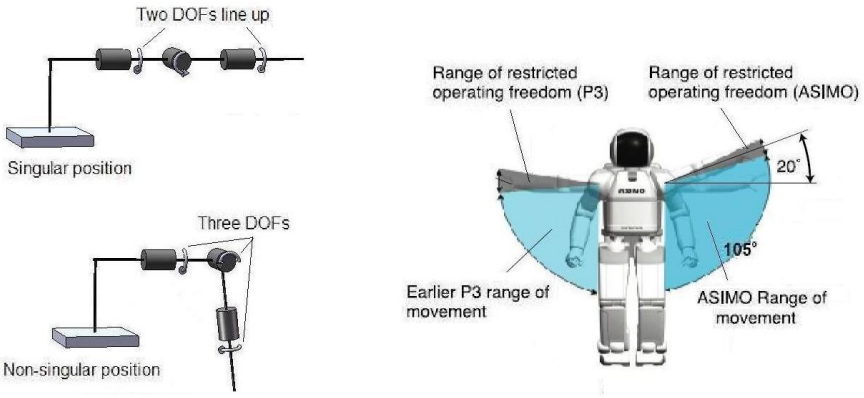


Figure 3.3: Singularity of the glenohumeral joint on serial humanoid arms [27].

While the DC electric motor, commonly used in serial robot arms, provides simple joint linear control, placing motors and gears at the joint makes the arm heavy. The large weight of the arm produces large impact forces, making it unsafe for use in human environments. To reduce the mass and inertia of the arm, cable drives have been used in some cases, with the majority of motors located at the base of the robot arm or thorax of the robot. Cable drives have the limitation of not being very accurate [37]. To increase its accuracy, DM2 [41] uses actuators located at the base combined with a small servo motor directly at the joint which maintains performance without significantly increasing load. Cable routing can be complicated and result in coupling between joints [42]. Though PAMs provide antagonistic actuation, a PAM actuation system needs electric valves and a compressed air generator, which are heavy and large thus are not able to easily be incorporated into the humanoid shape and size [43] [44] [45].

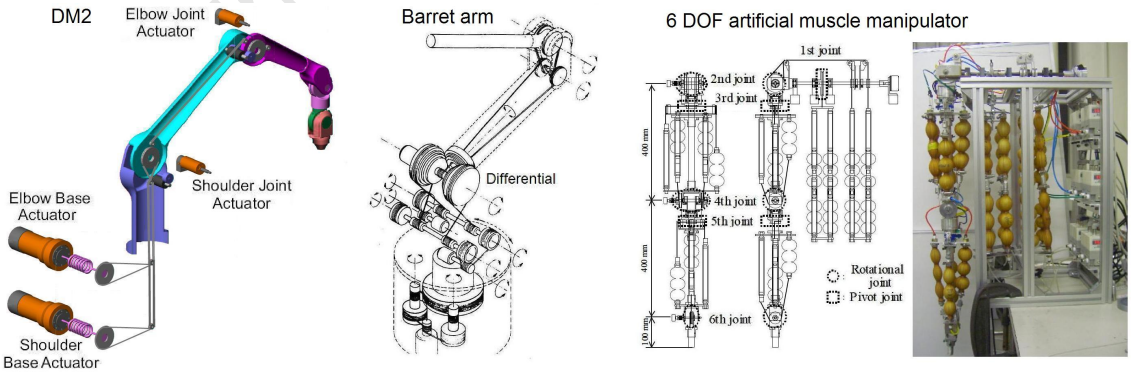


Figure 3.4: Cable driven arms (DM2 [41] and Barret arm [37]) and PAM actuated arm (6 DOF artificial muscle manipulator [43]).

Information on the range of motion of different serial humanoids was obtained from a number of studies, [28][29][30][31][33][34][38][40][45][46][47][48][49][50]. For serial arms, at the elbow and the wrist, the humanoids have motion ranges that compare favorably with that of humans. The humanoid glenohumeral joints, however, have some limitations as shown in figure 3.5. For glenohumeral flexion and glenohumeral rotation, the humanoids' ranges are mainly similar to that of humans. The range of glenohumeral abduction in number of humanoids is much less than that attainable by human arms.

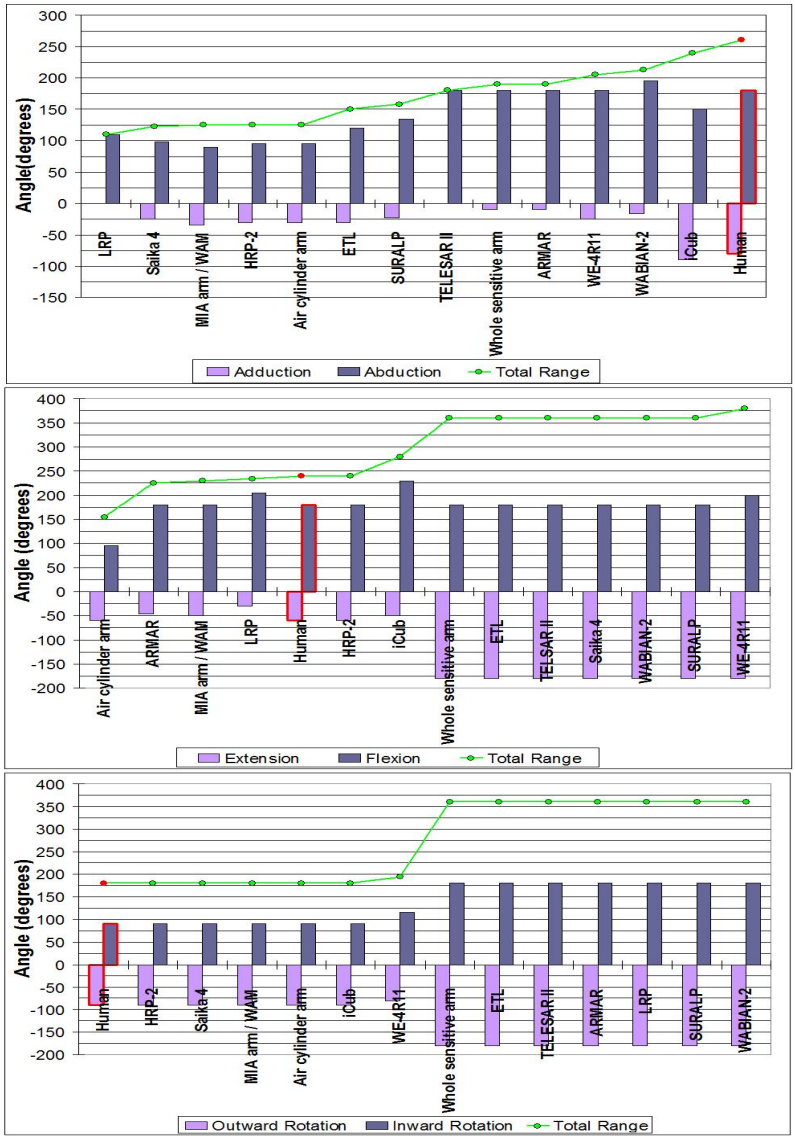


Figure 3.5: Glenohumeral range of motion for serial humanoid robots. Human range highlighted in red. [28][29][30][31][33][34][38][40][45][46][47][48][49][50]

### Parallel humanoid arms

Parallel humanoid arms come closer than serial arms to mimicking the muscle and joint structure of human arms. These arms have antagonistic muscle groupings actuating a single joint to produce more than one DOF of motion of the joint. For most parallel arms, the actuator and joint configuration is still much simpler than that of a humans. Most are made up of modular parallel mechanisms, each mechanism making up one multi-DOF joint. (See figure 3.6). Though parallel arms do not suffer from the glenohumeral joint singularity, they require more actuators per joint than serial arms and are generally more complex to model so they are not as widespread as serial arms. Tendon drives consisting of cables driven by motors and PAMs actuators are common means of actuating parallel arms. The parallel tendon drive structure of these robots allows for the stiffness of the arms to be adjusted, enabling the arm to have compliant characteristics. Joints are usually three DOF spherical joints and two DOF universal joints.

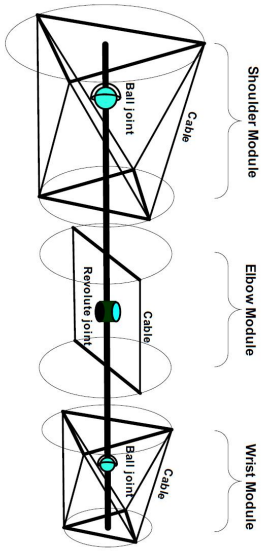


Figure 3.6: Modular parallel structured humanoid robot arm [51].

Figure 3.7 shows some parallel arms. The Pneumatic Artificial Rubber Muscle (PARM) arm has six DOFs [52] and the Strand-Muscle Actuator Robot Arm (StMA-RA) has four DOFs [53]. Two different seven DOF cable driven arms in [54], [51] and [55] have tendon driven structures. All the actuators are located at the base of the arm and tendons transmit the motion to the joints. Kotara is a muscle actuated humanoid that remains true to the human mold with human like skeleton and joints. Unlike the humanoids already discussed, it has a shoulder

girdle with 13 arm and shoulder girdle DOFs in total [56]. As with serial PAM actuated arms, the need for electric valves and a compressed air generator, make the PAM system too large and heavy to be incorporated into the humanoid shape and size. Length change of PAMs limit the range of motion possible for the joint.

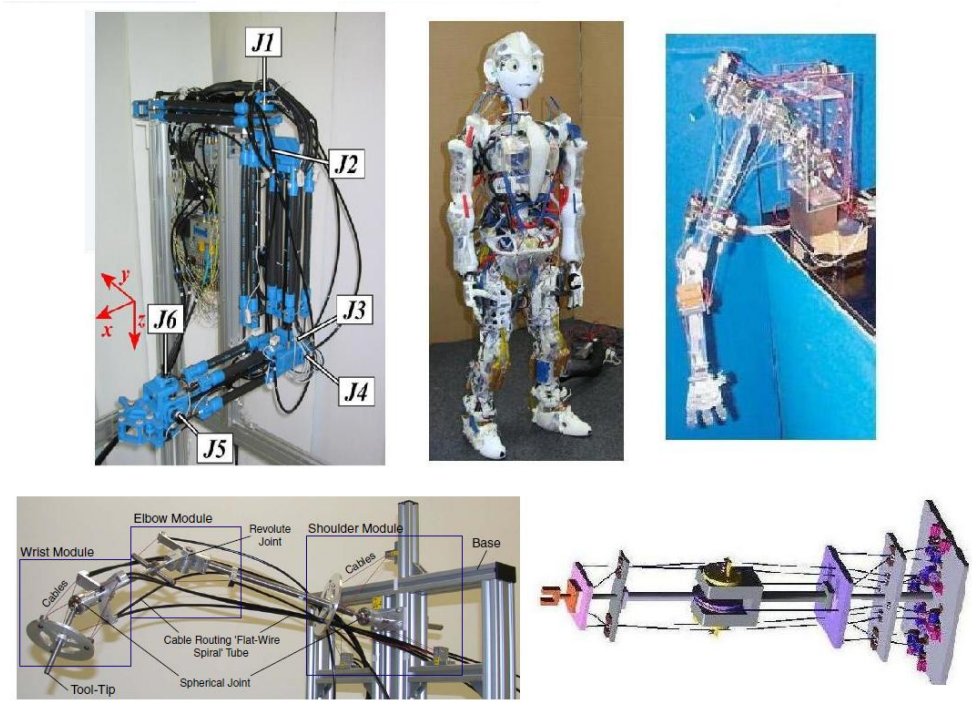


Figure 3.7: Humanoid arms with parallel kinematic structures. From left to right starting from top row; PARM arm [52], Kotaro [56], StMA-RA Arm [53], 7 DOF arm 1 [54], 7 DOF arm 2 [55].

Little literature is available on the range of parallel arms. Three DOF joints such as the spherical joint used in a number of parallel humanoid arms, usually have a limited range of motion, unlike the highly mobile three DOF joints of the human arm. In [57] the PARM driven arm has the range of motion shown in table 3.1.

The range of motion of the PARM arm [57], shown in table 3.1, is markedly less than the human range and less than most serial structured arms, shown in figure 3.5. The PARM's joint range, especially at the glenohumeral joint, is deficient to such an extent that it can be concluded without further modeling that it would not follow human arm motion well. The lack of information on the joint angle range of other parallel arms means that modeling and motion imitation of these arms cannot be carried out. Parallel arms will therefore not be investigated further in this study.

Table 3.1: Range of motion of the PARM parallel arm [57].

| | **Humanoid** | | **Human** | |
|---|---|---|---|---|
| **DOF** | Minimum | Maximum | Minimum | Maximum |
| Wrist flexion | $-22^o$ | $22^o$ | $-70^o$ | $80^o$ |
| Wrist abduction | $-35^o$ | $35^o$ | $-20^o$ | $30^o$ |
| Elbow flexion | $-35^o$ | $35^o$ | $-10^o$ | $150^o$ |
| Radioulna pronation | $-22^o$ | $22^o$ | $-90^o$ | $90^o$ |
| Glenohumeral flexion | $-28^o$ | $28^o$ | $-60^o$ | $180^o$ |
| Glenohumeral abduction | $-28^o$ | $28^o$ | $-75^o$ | $180^o$ |

### 3.1.2 Humanoid shoulder girdles

Most humanoid robots, have an upper limb consisting of an arm with no shoulder girdle, though some shoulder girdle designs do exist. Like the arm, the shoulder girdle can be approximated as a serial mechanism consisting of linkages, as done with Rapilee [58] and the WE-4RII [40] or as a parallel mechanism as done with the Cybernetic shoulder [59] [26], the Biomech shoulder [60] and Kotaro [61]. See figure 3.8.

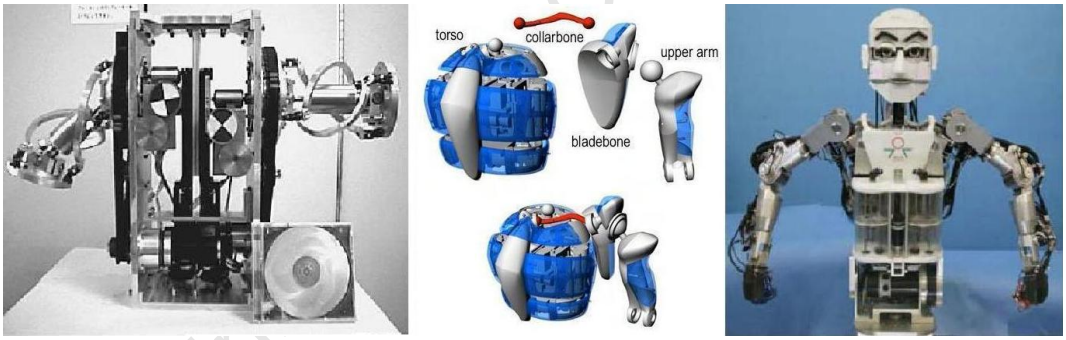


Figure 3.8: Humanoid shoulder girdle designs. From left to right; Cybernetic shoulder [59], Kotaro [61], WE-4RII [40].

Kotaro has a six DOF shoulder girdle with scapular and clavicle similar to a human's [56]. Kotaro's muscle configuration differs from the human configuration as shown in figure 3.9. As mentioned by Stanisic et al [62], because of the dissimilar configuration, some motion of the shoulder girdle may actually not be achieved. The shoulder girdle has low range of motion and yet supports the high loads generated by the arm. Three DOF parallel shoulder girdles such as the cybernetic shoulder and biomech shoulder have an advantage as parallel mechanisms can support high loads. However, they require a large number of actuators and complex control. The cybernetic shoulder, in addition, takes up a lot of space within the

torso. Serial shoulder girdles like that of Rapliee and WE-4RII while simple in design, require large actuator forces to be able to lift the rest of the arm due to the moment arm effect.

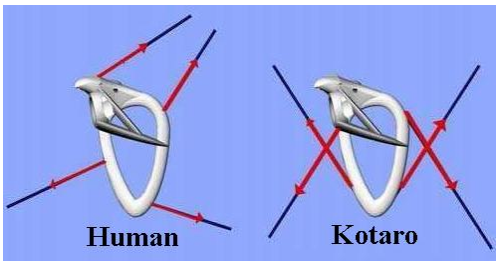


Figure 3.9: Muscle layout of human compared to actuation structure of Kotaro's scapula [56].

Little information is again available on the range of humanoid shoulder girdles. The emotion expression arm WE-4R11 has a range shown in table 3.2. Both shoulder girdle elevation and protraction are higher than the human range.

Table 3.2: Range of motion of WE-4R11 shoulder girdle [40].

| | **Humanoid** | | **Human** | |
|---|---|---|---|---|
| **DOF** | Minimum | Maximum | Minimum | Maximum |
| Shoulder girdle elevation | $0^o$ | $120^o$ | $0^o$ | $35^o$ |
| Shoulder girdle protraction | $-18^o$ | $25^o$ | $-30^o$ | $30^o$ |

The main advantage of a shoulder girdle is that it increases the arm workspace and helps the arm to avoid self collisions with the body. In their study, Lenacic et al [63] found that the shoulder girdle increases the human arm range by 50% when collisions with the body are taken into account. Because of the way the human arm joint range can change at different arm positions, a representation of the full human arm workspace is not easy to obtain and so comparisons of humanoid workspace to the human workspace are difficult. Humanoids with shoulder girdles and those without will be compared in this thesis to determine the effect of the humanoid shoulder girdle on the motion imitation of the arm.

### 3.1.3 Humanoid torsos

Most humanoids do not have a highly flexible spine as found in humans. Typically, humanoids have a waist with three joints, giving the three spine degrees of freedom. Kotaro [56], however has a flexible spine with five spherical joints. Each

vertebra has four tendon attachment points. Kojiro [64] is another humanoid with a flexible spine. ECCE1 [65] has flexible spine with four vertebra actuated by antagonistic muscles placed at four sides of the spine. The torso of most humanoids is used to store the computers and batteries and in some cases, the actuators of the humanoid. SURALP [66] has a one DOF rotational waist joint. HRP-2 [28] and WE-4R11 [67] have two DOFs, flexion and rotation. iCub [49], ETL [50], ARMAR [29] [30], WABIAN-2 [48] all have three DOFs waists. Some humanoids like LRP [28] and Saika-4 [31] have no waist DOFs at all.

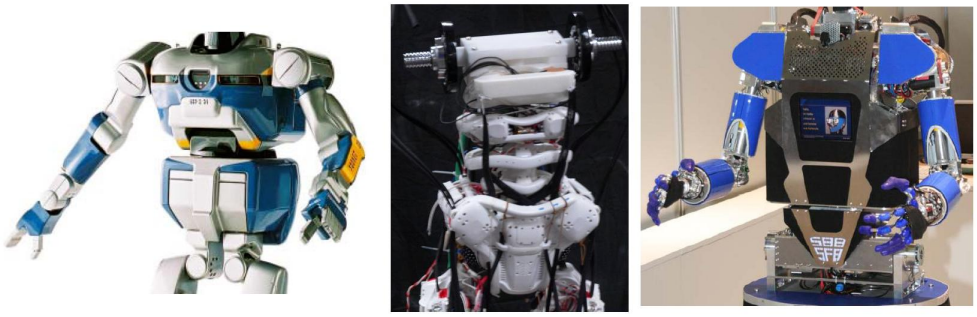

Figure 3.10: Humanoid torsos. Left to right; HRP [28], Kojiro [64], ARMAR [29].

The range of motion of some humanoid robot spines is shown in figure 3.11 [66] [28] [29] [48] [49] [50]. For spine flexion, the humanoids have a range of motion smaller than that of humans. Most humanoids with a lateral flexion DOF have a range of lateral flexion range greater than that of a human. The humanoids studied have a larger spine rotation range than that of humans.

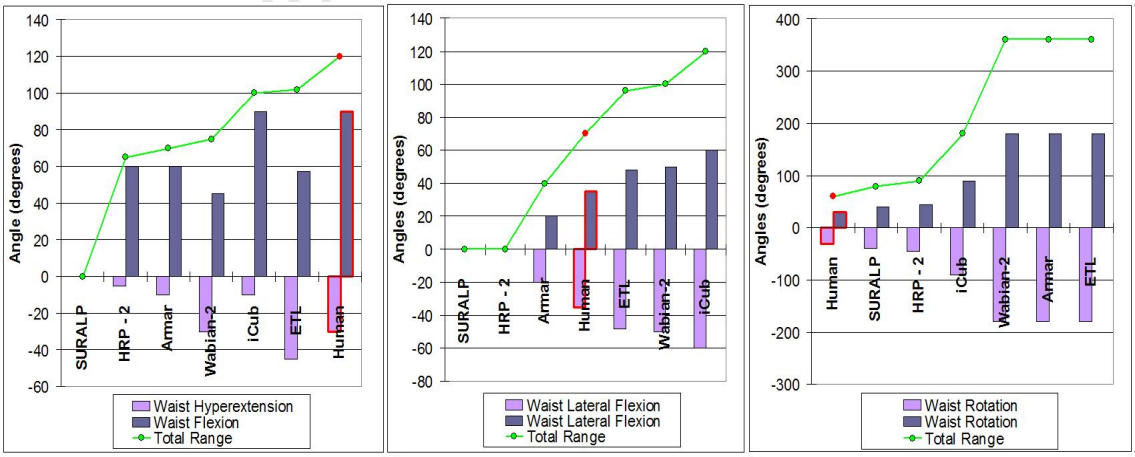


Figure 3.11: Waist motion range for humanoid robots. Human range highlighted in red. [66] [28] [29] [48] [49] [50]

## 3.2 Human motion imitation of humanoids

Motion capture, according to [68], provides timing and subtle elements of the actors performance. In human motion capture of dance movements, markers are placed on the human corresponding with the segments of the human body. Markers can be visual, inertial, reflective, or magnetic. Figure 3.12 shows some motion capture markers. The markers are tracked using cameras to get the positions of various body segments. The number and placement of markers varies with each type of motion capture system.


Figure 3.12: Marker locations for human motion capture [69].

### 3.2.1 Human motion transfer

Human motion capture results in the locations of various body segments at regular intervals throughout the captured motion. Because of the differences in the structure and mechanical limits of humanoids and humans, this motion data cannot be transfered directly to the humanoid.

Pollard et al [17] mapped the human motion capture data to the robot by setting the robot joint angles such that each robot segment matches the orientation of the corresponding human segment. Positions near to the glenohumeral joint singularity were identified and a restricted DOF solution applied. For each individual joint motion that exceeded its joint limit, the joint motion was scaled locally. The velocities of each joint were then scaled to fit the joint velocity limits. Both Nakaoka et al [19] and Nakazawa et al [20] used the method proposed by Pollard et al. While individual joint motions were preserved well using this method, because each joint was scaled independently, the overall configuration of the robot was not

preserved. To address this, Safonova et al [68] used an optimisation procedure that scaled the joint angles at the same time. The procedure contained an objective function that tried to; preserve the oscillations of the original motion, preserve the configuration of the robot and prevent the motion from reaching the joint angle limits. They then added a constraint to avoid self collisions.

Ruchanurucks et al [70] used inverse kinematics to find the required joint angles from the motion capture data. B-Splines were then used to represent the motion of the joints. The B-Spline was then altered with an objective functions that minimise the error of the joint angles, the error of the end effector positions, and maximises manipulability. They incorporated joint angle limits constraints, self-collision avoidance, velocity limits and dynamic force limits to the B-Splines.

Riley et al [18] recovered the required joint angles for the robot using a numerical solution that modeled the robot's kinematics using twist coordinates. They then minimised the difference between the measured marker positions and calculated marker positions by solving the non-linear optimisation problem. The trajectory was then scaled to fit the robot's joint angle limits.

Dariush et al [71] [72] [73] used a singularity robust inverse kinematics method, the damped least squares method to compute the joint angles of the robot from the motion capture data. Joint limit avoidance and self collision avoidance was achieved based on a Weighted Least-Norm solution that was inputed directly into the inverse kinematics. They limited joint velocities by rescaling the motion profile in time. As this method added constraints directly into the inverse kinematics and thus does not require any further constraint and optimisation steps, this method will be used for motion re-targeting in this thesis.



### 3.2.2 Self collision detection

To avoid arm configurations that would result in self collisions of the arm with the body, in [68], the robot's body segments were approximated using circular cylinders capped by spheres and the distance between these shapes was used to determine the proximity of segments. If no two shapes that approximate the body segments intersected, then the motion was considered free of self collisions. This cylinder with end caps is similar to the line swept sphere used in [74] to model the human body for collision detection. Circular cylinders and spheres were also used in [75] to model the robot body and arms. In [70], to generate self collision free motion for a humanoid from human motion, check points were placed inside

the robot's body and the arm was modeled using circular cylinders. The distance between a cylinder and the check points was then used to determine collisions. While these methods may be relatively simple to implement, they do not provide a good fit for the humanoid torso shape.

Other methods that attempt to precisely model the shape of the humanoid include convex hulls [76], [77], [78], [79] and swept-sphere volumes [80], [81], [82], which have been used in real-time collision avoidance schemes. However the convex hulls are computationally intensive and both convex hulls and swept spheres require a detailed model of the humanoid which may not always be available.

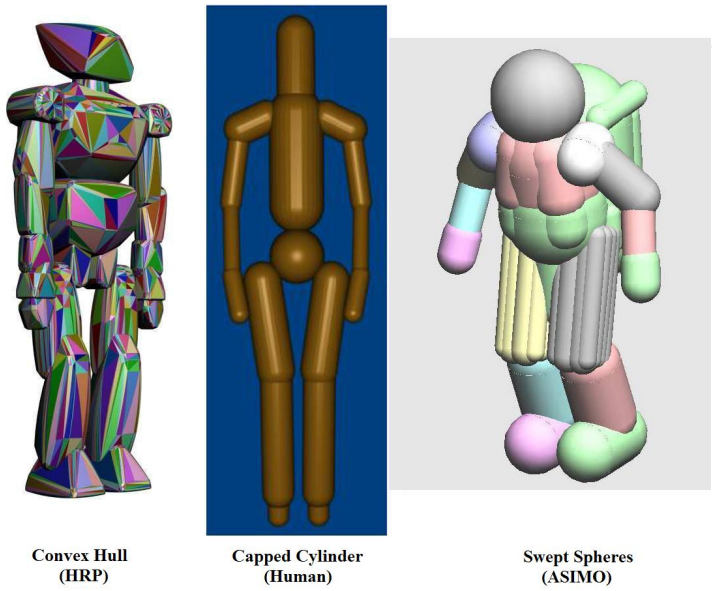


Figure 3.13: Humanoid self collision bounding volumes. From left to right; convex hull [77], capped cylinder [74], swept sphere volume [80].

This thesis therefore will formulate a new self collision detection scheme that aims for simplicity while still providing a close fit to the humanoid torso. The collision detection scheme should have a small number of checks while minimising the difference between the bounding volume and the actual humanoid.

### 3.2.3 Human motion imitation

While dance is a popular means of testing a humanoid's motion capabilities, other types of motion are also used. Pollard et al [17] used the Sarcos humanoid robot ATR(DB) to mimic the actions of the song 'I'm a little teapot'. A Sarcos robot

was also used by Riley et al [18] to perform a human dance. HRP-1S was used by Nakaoka et al [19] [20] in their motion transfer of a traditional dance.

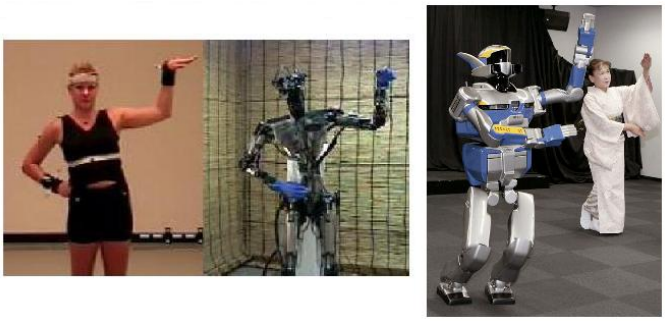

Figure 3.14: Human dance imitation of humanoid robots [68] [83].

Comparing the motion data generated from remapping the human motion data, shows that the robot's motion path differed from the human motion at certain points due to the added robot physical constraints. Using Pollards et al's method for avoiding singularities, Nakaoka et al obtained the joint angle trajectory as shown in figure 3.15. The motion around the singular point was very different from the original motion. Nakaoka et al also found that some motions such as 'stop motions' and certain important postures of the dance could be lost due to modifying the human trajectories to fit the humanoid robot [19] [20]. Certain constraints had to be added to the robot motion to recreate these postures and motions. For Riley et al, the largest differences in trajectory were from trajectory changes made in adjusting to the robot's joint limits [18].

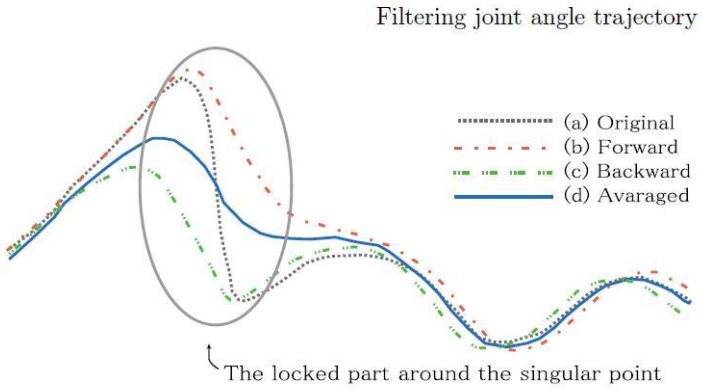


Figure 3.15: Motion imitation results - Nakaoka et al [19].

Pollard et al found the robot motion to be a good match for the human motion in many of the frames. Limited shoulder motion of the robot in how high the robot

could raise its arm and in humeral rotation affected motion in some of the frames. The lack of a shoulder girdle limited humeral rotation and how high or low the robot could raise its arms [17]. Figure 3.16 shows the effect of joint and velocity limits on the motion of raising arms up then rapidly lowering them.

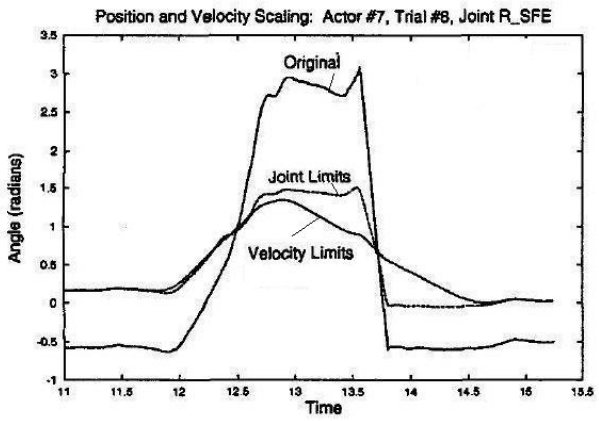


Figure 3.16: Motion imitation results - Pollard et al [17].

These motion imitation attempts do not use humanoids with shoulder girdles and do not compare the motion imitation of humanoids with the same motion data. This thesis will therefore compare the motion of several humanoids with varying degrees of freedom and joint limits using the same motion capture data set.

## 3.3 Summary

The most common structure that humanoids take is that of serial mechanisms. Such a serial structure results in a singularity at the glenohumeral joint, which occurs when two DOFs line up, thus a DOF of the arm is lost. Parallel structured humanoids have some advantages over serial ones, but parallel humanoids have the disadvantage of a very limited range of motion. One of the most common problems found during human motion transfer attempts to humanoids, was of the limited motion range of humanoid joints. Most humanoid glenohumeral joints have acceptable ranges for the glenohumeral flexion joint and glenohumeral rotation joint, however, the glenohumeral adduction range mostly falls below that of a human's. Most humanoids do not have a shoulder girdle, however human motion imitation of some humanoids shows that this lack has a large effect on the imitation abilities of the humanoids.

# Chapter 4

# Modeling of Humanoid Upper Bodies



To transfer human motion to a humanoid and to determine the humanoid capabilities, a model describing the humanoid structure and motion is vital. The forward kinematics model describes the pose and the velocities of the humanoid. Human motion capture data is transfered to the humanoid through inverse kinematics modeling, including physical constraints such as joint limits and self collisions. This chapter details the forward and inverse kinematics models used for the humanoids. The humanoid self collision detection model developed in this thesis is also discussed.

## 4.1 Forward kinematics modeling for motion computation

Forward kinematics modeling, which is split into direct kinematics modeling and differential kinematics modeling, uses the individual properties of the robot's joints to characterise the motion properties of the whole robot. Direct kinematics deals with finding the pose of the robot given the joint angles while differential kinematics describes the motion of the whole robot given the joint velocities.

### 4.1.1 Direct kinematics modeling

The direct kinematics model describes the geometry and computes the position, orientation and workspace of the humanoid robot. To model the geometry of the robot a reference frame is attached to each link of the robot. Each link in the robot is then completely described in space by its position and orientation with respect to a base reference frame. A set of direct kinematic equations for the robot can then be derived by computing the position and orientation of one coordinate frame in relation to the other. The resulting equations are dependent on the coordinate frames chosen. The robot configurations, however, are geometric quantities independent of the frames chosen to describe them. [84] [85]

A coordinate reference frame $O_i$ consists of an origin $O$, and three mutually orthogonal basis vectors $\boldsymbol{x}_i$, $\boldsymbol{y}_i$, $\boldsymbol{z}_i$ of the frame axis. The position of the origin of coordinate frame $O_i$ relative to coordinate frame $O_j$ can be denoted by vector ${}^{j}\boldsymbol{p}_i$. The orientation of frame $O_i$ relative to frame $O_j$ can be denoted by the rotation matrix ${}^{j}\boldsymbol{R}_i$. With homogeneous transformation matrices, position vectors and rotation matrices are combined together in a compact notation ${}^{i-1}\boldsymbol{A}_i$. [85]

$$ {}^{i-1}\boldsymbol{A}_i = \begin{pmatrix} \boldsymbol{R_i} & {}^{i-1}\boldsymbol{p}_i \\ \boldsymbol{0} & 1 \end{pmatrix} \tag{4.1} $$

The $4 \times 4$ homogeneous transformation matrix, ${}^{j}\boldsymbol{T}_i$ gives the position and orientation of link $i$ with respect to link $j$. The matrix ${}^{j}\boldsymbol{T}_i$ transforms vectors from coordinate frame $O_i$ to coordinate frame $O_j$. Its inverse ${}^{j}\boldsymbol{T}_i{}^{-1}$ transforms vectors from coordinate frame $O_j$ to coordinate frame $O_i$. [86] [85]

$$ {}^{0}\boldsymbol{T}_n = {}^{0}\boldsymbol{A}_1 \quad {}^{1}\boldsymbol{A}_2 \quad \ldots \quad {}^{n-1}\boldsymbol{A}_n \tag{4.2} $$

#### The Denavit-Hartenberg convention for coordinate frames

There are two systematic methods for for kinematics modeling that are widely used. These are the Denavit-Hartenberg convention and the Screw theory based method. The Denavit-Hartenberg convention is the most popular method due to its consistency, conciseness and use of a minimal number of parameters [87]. The Screw based method requires a non minimal set of parameters and is more complex

than the Denavit-Hartenberg convention [87]. The Denavit-Hartenberg convention is thus used in this thesis for locating frames on the robot links and is as follows (see figure 4.1) [86] [85]:

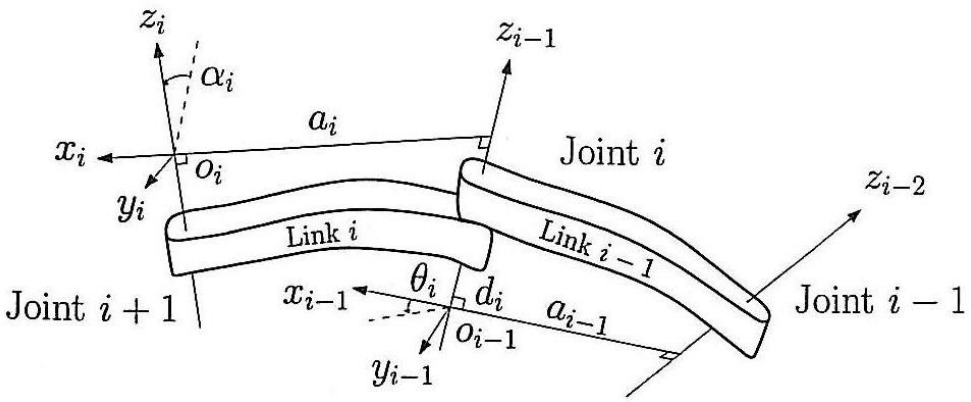


Figure 4.1: Serial humanoid Denavit-Hartenberg model [84].

- The links are numbered from 1 to $n$, with the base numbered 0,
- The joint are numbered from 1 to $n$, with joint $i$ located between link $i-1$ and link $i$,
- The $\boldsymbol{z}_i$ axis of frame $O_i$ is located at the axis of joint $i+1$,
- The $\boldsymbol{x}_i$ axis of frame $O_i$ is located perpendicular to $\boldsymbol{z}_{i-1}$ and $\boldsymbol{z}_i$ with $\boldsymbol{x}_0$ arbitrarily chosen,
- The $\boldsymbol{y}_i$ is found using the right hand rule.

The convention requires four parameters to locate one reference frame relative to another. The four parameters are defined as [86] [85]:

- The link length $a_i$, is the distance between $\boldsymbol{z}_{i-1}$ and $\boldsymbol{z}_i$ along $\boldsymbol{x}_i$,
- The joint offset $d_i$, is the $\boldsymbol{x}_i$ coordinate along $\boldsymbol{z}_{i-1}$,
- The link twist $\alpha_i$, is the angle from $\boldsymbol{z}_{i-1}$ to $\boldsymbol{z}_i$ about the $\boldsymbol{x}_i$ axis, positive rotation is counter-clockwise,
- The joint angle $\theta_i$, is the angle from $\boldsymbol{x}_{i-1}$ to $\boldsymbol{x_i}$ about the $\boldsymbol{z}_{i-1}$ positive rotation is counter-clockwise.

Two of the four parameters, $a_i$ and $\alpha_i$ are always constant and depend only on the geometry of connection between consecutive joints. For revolute joints the $\theta_i$ is variable, while for translational joints, $d_i$ is variable. [85] [84] [86].

${}^{i-1}\boldsymbol{A}_i$ the transformation matrix of frame $O_i$ to frame $O_{i-1}$ is then [85]:

$$\boldsymbol{q} = \begin{pmatrix} \theta_1 & \theta_2 & \dots & \theta_n \end{pmatrix}^T \tag{4.3}$$

$${}^{i-1}\boldsymbol{A}_i = \begin{pmatrix} \cos\theta_i & -\sin\theta_i\cos\alpha_i & \sin\theta_i\sin\alpha_i & a_i\cos\theta_i \\ \sin\theta_i & \cos\theta_i\cos\alpha_i & -\cos\theta_i\sin\alpha_i & a_i\sin\theta_i \\ 0 & \sin\alpha_i & \cos\alpha_i & d_i \\ 0 & 0 & 0 & 1 \end{pmatrix} \tag{4.4}$$

The transformation matrix of frame $n$ to the base is [85]:

$${}^0\boldsymbol{T}_n(\boldsymbol{q}) = \begin{matrix} {}^0\boldsymbol{A}_1(q_1) & {}^1\boldsymbol{A}_2(q_2) & \dots & {}^{n-1}\boldsymbol{A}_n(q_n) \end{matrix} \tag{4.5}$$

where $\boldsymbol{q}$ is the $n \times 1$ vector of joint variables.

### 4.1.2 Differential kinematics modeling

The differential kinematics gives the relationship between joint velocities and the corresponding link's linear and angular velocities. [85]

#### The Jacobian

The relationship between the joint velocities and the link velocities is given by a matrix termed the Jacobian. All possible velocities of the humanoid are linear combinations of the columns of the humanoid's Jacobian matrix $\boldsymbol{J}$. The link linear velocity $\dot{\boldsymbol{p}}$ and angular velocity $\boldsymbol{\omega}$ are expressed as a function of the joint velocities $\dot{\boldsymbol{q}}$ by means of the following relations [85]:

$$\boldsymbol{v} = \begin{pmatrix} \dot{\boldsymbol{p}} \\ \boldsymbol{\omega} \end{pmatrix} = \boldsymbol{J}\dot{\boldsymbol{q}} \tag{4.6}$$

For a serial structured robot with rotational joints, the Jacobian is given by [85]:

$$\boldsymbol{J} = \begin{pmatrix} \boldsymbol{J}_{P1} & \dots & \boldsymbol{J}_{Pn} \\ \boldsymbol{J}_{O1} & \dots & \boldsymbol{J}_{On} \end{pmatrix} = \begin{pmatrix} \boldsymbol{J}_{P} \\ \boldsymbol{J}_{O} \end{pmatrix} \tag{4.7}$$

and

$$\begin{pmatrix} \boldsymbol{J}_{P1} \\ \boldsymbol{J}_{O1} \end{pmatrix} = \begin{pmatrix} \boldsymbol{z}_{i-1} \times (\boldsymbol{p} - \boldsymbol{p}_{i-1}) \\ \boldsymbol{z}_{i-1} \end{pmatrix} \tag{4.8}$$

for a revolute joint. [85]

$\boldsymbol{J}_P$ is the $3 \times n$ matrix relative to the contribution of the joint velocities $\dot{\boldsymbol{q}}$ to the robot's linear velocities $\dot{\boldsymbol{p}}$, while

$\boldsymbol{J}_O$ is the $3 \times n$ matrix relative to the contribution of the joint velocities $\dot{\boldsymbol{q}}$ to the robot's angular velocities $\boldsymbol{\omega}$.

$\boldsymbol{z}_{i-1}$ is the unit vector of axis $\boldsymbol{z}$ of frame $O_{i-1}$ and is given by the third column of the rotation matrix ${}^0\boldsymbol{R}_{i-1}$

$\boldsymbol{z}_0$ is given as:

$$\boldsymbol{z}_0 = \begin{pmatrix} 0 \\ 0 \\ 1 \end{pmatrix} \tag{4.9}$$

$\boldsymbol{p}_n$ is the position vector of the origin of frame $O_n$ and is given by the first three elements of the fourth column of the transformation matrix ${}^0\boldsymbol{T}_n$

$\boldsymbol{p}_{i-1}$ is the position vector of the origin of frame $O_{i-1}$ and is given by the first three elements of the fourth column of the transformation matrix ${}^0\boldsymbol{T}_{i-1}$

$\boldsymbol{p}_0$ is given by:

$$\boldsymbol{p}_0 = \begin{pmatrix} 0 \\ 0 \\ 0 \end{pmatrix} \tag{4.10}$$

## 4.2 Inverse kinematic modeling for motion transfer

Inverse kinematics determines the robot joint angles corresponding to a desired robot position and orientation [85], obtained from motion capture data. If the desired robot pose is not attainable by the joints, the inverse kinematics should be able to estimate joint angles that result in a suitable pose that is close to the desired pose. Inputing the joint angles obtained from the inverse kinematics into the robot's forward kinematics equations gives the resultant pose of the humanoid. Both direct kinematics and differential kinematics can be inverted to find the required joint angles.



### 4.2.1 Direct kinematics inversion

There are two methods that can be used to obtain the solution to direct inverse kinematics, the algebraic method and the geometric method. The algerabic method requires the direct kinematics equations of the robot, while the geometric method, as the name implies, depends on the geometry. Both these methods require the robot to satisfy certain structural conditions in order to be applied to the robot. In general these methods, are suited for six degree of freedom (DOF) systems with a special type of kinematic structure. [86] [84] [85]

Algebraic methods involve identifying the significant equations containing the joint variables and solving the equations. Given the link positions, the inverse kinematics can be calculated algebraically using the homogeneous transform matrix. The set of significant equation to be solved is however, not general but robot dependent. The significant equations are also nonlinear and not always obvious to formulate. In addition, multiple or no solution to the equations may exist. In some cases, solutions may exist but they cannot be represented in closed form. For robots

with high degrees of freedom such as humanoids, the equations become increasingly complex and difficult to formulate and solve, making this method unsuitable for humanoids. [86] [84] [85]

The general idea of the geometric approach is to solve for joint angle $\theta_i$ by projecting the arm onto the $O_{i-1}$ axis and solving the trigonometry problem. Again, the solution is not general, but robot dependent and in some cases cannot be represented in the closed form. Multiple or no solution may again exist. The geometric method is thus not well suited for humanoids. [84] [85] [86]

### 4.2.2 Differential kinematics inversion

Unlike the direct kinematics inversion, differential kinematics inversion presents a linear mapping between the joint variables and the link variables. Joint velocities can be obtained by inverting the Jacobian matrix resulting in the general solution: [85] [39]

$$\dot{\boldsymbol{q}} = \boldsymbol{J}^{-1}\boldsymbol{v} \tag{4.11}$$

Given the joint angles of the initial posture of the robot, the joint angles at each motion time instant can thus be calculated numerically using [85] [39]:

$$\boldsymbol{q}(t_{k+1}) = \boldsymbol{q}(t_k) + \dot{\boldsymbol{q}}(t_k)\Delta t \tag{4.12}$$

where $\Delta t$ is the time interval.

This method provides a general solution to the inverse kinematics of robots and is useful for robots with a large number of degrees of freedom, such as humanoids. A disadvantage of such a numerical method is the tendency to suffer from a small amount of error (numerical drift) from numerical integration. Numerical drift leads to a long term accumulation in error of the robot's overall motion profile from the desired motion profile [39]. While some methods exist that attempt to compensate for such drift, they are not applied in this thesis as it is assumed that all the humanoids will suffer similarly from numerical drift without greatly affecting the motion imitation results. The small time interval used in motion capture, means that the resultant numerical error and its resultant drift would be very small and can be neglected. The robots's motions will however, still be examined for any possible effects of numerical drift.

### Augmented Jacobian for multiple tasks

To specify the motion of more than one link, the augmented jacobian, which combines the tasks for the links, can be used. $\boldsymbol{v}$ is the first task velocity and $\boldsymbol{v}_c$ is the second task velocity. $\boldsymbol{J}$ is the Jacobian for the first set of joints and $\boldsymbol{J}_c$ is the Jacobian for the second set.

The augmented task vector is given by: [39]

$$\boldsymbol{v}_a = \begin{pmatrix} \boldsymbol{v} \\ \boldsymbol{v_c} \end{pmatrix} \tag{4.13}$$

The augmented Jacobian is given by [39]:

$$\boldsymbol{J}_a = \begin{pmatrix} \boldsymbol{J} \\ \boldsymbol{J_c} \end{pmatrix} \tag{4.14}$$

The velocity mapping to solve is thus [39]:

$$\boldsymbol{v}_a = \boldsymbol{J}_a \dot{\boldsymbol{q}} \tag{4.15}$$

### Pseudo and DLS Jacobians for redundant and singular joints

For redundant manipulators such as humanoid arms, there are many solutions to the inverse kinematics. The solutions to $\dot{\boldsymbol{q}}$ that minimise the cost function of the joint velocities can thus be chosen from these solutions. This results in the right pseudo-inverse of $\boldsymbol{J}$, $\boldsymbol{J}^\dagger$, which locally minimises the norm of the joint velocities. [85] [39]

$$\boldsymbol{J}^\dagger = \boldsymbol{J}^T(\boldsymbol{J}\boldsymbol{J}^T)^{-1} \tag{4.16}$$

$$\dot{\boldsymbol{q}} = \boldsymbol{J}^\dagger \boldsymbol{v} \tag{4.17}$$

For the inversion of $\boldsymbol{J}$ to be computed, the Jacobian relating the link linear velocities to the joint angular velocities has to be of full rank, that is, the robot is not near a singular configuration. To overcome the problem of inverting the differential kinematics in the neighborhood of a singularity, the damped least-squares (DLS) inverse can be used. It is given by: [85] [39]

$$\boldsymbol{J}^{\star} = \boldsymbol{J}^{T}(\boldsymbol{J}\boldsymbol{J}^{T} + \lambda^{2}\boldsymbol{I})^{-1} \tag{4.18}$$

where $\lambda$ is a damping constant and $\boldsymbol{I}$ is an identity matrix.

### Weighted DLS for constraints modeling

The null space of $\boldsymbol{J}$ gives the joint velocities that do not produce any link velocities for a particular arm posture. Weighing the Jacobian by the positive definitive matrix $\boldsymbol{W}$ allows constraints such as joint limit constraints and self collision avoidance constraints to be added to the solution. The DLS jacobian then becomes [71] [72] [73]:

$$\boldsymbol{J}^{\star} = \boldsymbol{W}^{-1}\boldsymbol{J}^{T}(\boldsymbol{J}\boldsymbol{W}^{-1}\boldsymbol{J}^{T} + \lambda^{2}\boldsymbol{I})^{-1} \tag{4.19}$$

The positive definitive matrix $\boldsymbol{W}$ can be made up of a number of different weighing matrices combined. In this case, the the joint limit weighing matrix $\boldsymbol{W_{JL}}$ alone is used, thus:

$$\boldsymbol{W} = \boldsymbol{W_{JL}} \tag{4.20}$$

### Joint limit weighing matrix

The joint limit weighing matrix, which keeps the robot from exceeding its joint motion limits, is computed from the joint limit function $\boldsymbol{H}(\boldsymbol{q})$. The gradient of $\boldsymbol{H}$, $\nabla\boldsymbol{H}$, is a vector representing the joint limit gradient function and it points in the direction of the fastest rate of increase of $\boldsymbol{H}$. [71] [72] [73]

$$\nabla \boldsymbol{H} = \frac{\partial \boldsymbol{H}}{\partial \boldsymbol{q}} = \left[\frac{\partial H}{\partial q_1}, \cdots, \frac{\partial H}{\partial q_n}\right] \tag{4.21}$$

where

$$H = \frac{1}{4}\sum_{i=1}^{n} \frac{(q_{iM} - q_{im})^2}{(q_{iM} - q_i)(q_i - q_{im})} \tag{4.22}$$

$$\frac{\partial H}{\partial q_i} = \frac{1}{4}\frac{(q_{iM} - q_{im})^2(2q_i - q_{iM} - q_{im})}{(q_{iM} - q_i)^2(q_i - q_{im})^2} \tag{4.23}$$

$q_{iM}$ is the maximum joint limit, $q_{im}$ is the minimum joint limit.

When the gradient is equal to zero, the joint is at the middle of its range, and as the gradient goes to infinity, the joint is at either limit. The joint limit weighing matrix $\boldsymbol{W_{JL}}$ is then an $n \times n$ diagonal matrix with diagonal elements $w_{JLi}$ [71] [72] [73] :

$$\boldsymbol{W_{JL}} = \begin{pmatrix} w_{JL1} & & \mathbf{0} \\ & \ddots & \\ \mathbf{0} & & w_{JLn} \end{pmatrix} \tag{4.24}$$

where

$$w_{JLi} = \begin{cases} 1 + \left|\frac{\partial H}{\partial q_i}\right| & if\ \nabla \left|\frac{\partial H}{\partial q_i}\right| \geq 0 \\ 1 & if\ \nabla \left|\frac{\partial H}{\partial q_i}\right| < 0 \end{cases} \tag{4.25}$$

$\nabla \left|\frac{\partial H}{\partial q_i}\right|$ represents the change in magnitude of the gradient function. A positive value means that the joint is moving towards its joint limit. When this occurs, the weighing factor goes towards infinity causing the joint motion to slow down. A negative value means the joint is moving away from its limit. [71] [72] [73]

## 4.3 Self collision detection

Self collisions of the various body segments of the humanoid can cause damage to the humanoid, thus self collision detection is important. The closest distance and closest points between two body segments has to be computed in order to detect potential self collisions. Segments of the humanoid are typically represented using a bounding volume that encompasses the entire segment. The distance between two bounding volumes thus gives an estimate of the self collision distance. Self collision detection schemes found in literature either provide an overly simple representation of the humanoid body resulting in the loss of feasible postures; or provide a detailed representation of the humanoid form that gives more accurate self collision detection, but tend to be computationally expensive. The detailed bounding volumes also require a 3D model or detailed drawings of the robot which are not generally available.

In this thesis a new collision detection scheme using elliptical capsules as bounding volumes to represent the humanoid form is formulated (presented in [88]). The human and humanoid torsos are modeled using elliptical capsules, defined here as an elliptical cylinder capped at either end by ellipsoids (see figure 4.2). This formulation aims to give a better fit than other simple bounding volumes typically used to model the humanoid torso shape for self collision detection, while still being simpler to implement and less computationally expensive than more detailed bounding volumes used in some collision detection attempts.

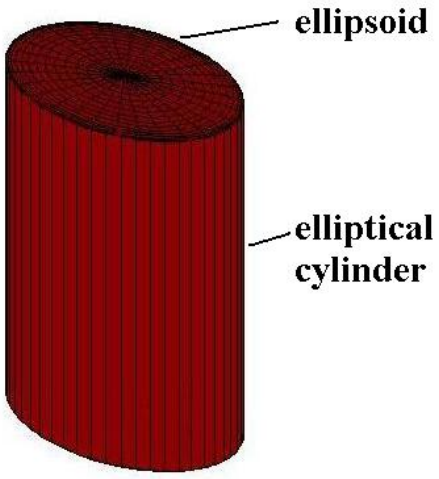


Figure 4.2: Elliptical capsule bounding volume for humanoid self collision detection.

### 4.3.1 Comparison of collision bounding volumes

Simple bounding volumes including circular capsules or sphere-swept lines (a circular cylinder capped by spheres) are used by a number of researchers for self collision detection of humanoids [74]. Convex hulls are a precise type of bounding volume used in a number of motion transfer attempts [79], [77], [78]. Swept sphere volumes [82] are a type of bounding volume that aim at being more precise than simpler bounding volumes while being less computationally intensive than convex hulls.

These three bounding volumes are compared with the elliptical capsule to find out how well the elliptical capsule performs in relation to other bounding volumes. As detailed models of humanoids are not available for comparison, a number of simple shapes are used to compare the bounding volumes. The shapes to be tested fall into three categories, cylinders, frustums and unit shapes. Three profiles are used for each category; a circle, rectangle and ellipse. Thus the shapes are; circular, elliptical and rectangular cylinders; circular, elliptical and rectangular frustums; a cube, sphere and ellipsoid.

The percentage difference in magnitude of volume between the shape and each bounding volume are computed as well as the number of faces making up the volume. The difference in volume gives an indication of tightness of fit while the number of faces gives an indication of computational cost. The number of faces can be used to give an idea of computational cost since for a single shape to be considered free of collisions, each face has to be checked for potential collisions thus the number of faces could be considered as being proportional to the computational cost of determining collisions.



#### Fitting the bounding volumes

Fitting the circular capsule and elliptical capsule bounding volumes to a shape is simple. For the circular capsule, the circle of smallest radius that would completely circumscribe the profile of the shape is found. For a rectangular profile this is half the length of the diagonal. For an ellipse profile it is value of the major axis. The minimum height of the circular capsule that would fit the shape is then found. Fitting elliptical capsules to a rectangular profile; the coordinates of the vertices can be substituted into the equation of an ellipse and solved to find the length of the two ellipse axes $a$ and $b$. The third axis $c$ of the ellipsoid cap is then equal to 1. For circular profile, both $a$ and $b$ are equal to the radius of the circle. The

height of the elliptical capsule is then the height of the cylinder or frustum. The equation of an ellipse is:

$$1 = \frac{x^2}{a^2} + \frac{y^2}{b^2} \tag{4.26}$$

A convex hull of a set of points is the smallest convex polygon or polyhedral containing the set of points. Each test shape is thus converted into a set of points. A built in MATLAB function implementing the convex hull algorithm is then used to fit a convex hull to the set of points. For the rectangular profile, the vertices of the shape are used as the set of points. For the circular and elliptical profiles, the circumference is divided into segments of equal angles from the center of the profile and the vertices of each segment are used. For the sphere and ellipsoid, the spiral point algorithm [89] [90] is used to distribute points on the surface of the shape. For $N$ points on the surface of a sphere, the spiral point algorithm for the point $\boldsymbol{k}$ is [89]:

$$\boldsymbol{k} = [\cos(l_k)r_k,\ \sin(l_k)r_k,\ z_k] \tag{4.27}$$

where:

$$r_k = \sqrt{1 - z_k^2} \tag{4.28}$$

$$z_k = z_{k-1} - dz \tag{4.29}$$

$$l_k = l_{k-1} + \frac{s}{r_k} \tag{4.30}$$

The initial values are:

$l_1 = 0$

$$z_1 = 1 - \frac{dz}{2} \tag{4.31}$$

And the constants are:

$$dz = \frac{2}{N} \tag{4.32}$$

$$s = \frac{3.6}{\sqrt{N}} \tag{4.33}$$

Fitting swept sphere volumes to a shape, again, requires a representation of the shape. The number of swept sphere lines used also affects the overall magnitude of the bounding volume. There are numerous ways of fitting swept sphere bounding volumes to a shape but no formal method of finding the best fit. For this study, each of the top and bottom profile is represented by spheres. For the square profiles, four spheres are used, the rectangular profiles use six spheres, elliptical profiles use three spheres and the circular profiles use a single sphere. The height between the top and bottom profiles is encompassed either by cylinders or spheres as appropriate. For the frustums, the frustum height is divided into four circles with decreasing radius.

Figure 4.3 shows the resulting bounding volumes for each test shape. Overall, the convex hull gives the best representation of the actual geometry of the shape, followed by the swept sphere volume. The circular capsule gives the worst representation of the geometry of the actual shape. The elliptical capsule bounding volume gives a good representation for only some of the shapes.



### Volume computation

The magnitude of the volume encompassed by each bounding volume for each shape is calculated using the following well known equations shown in figure 4.4 and table 4.1. Figure 4.4 shows some of the notations used for the frustums, spheres, spherical caps, ellipsoids and rectangular tube. For the convex bounding volume the volume encompassed is found from the MATLAB convex hull function.

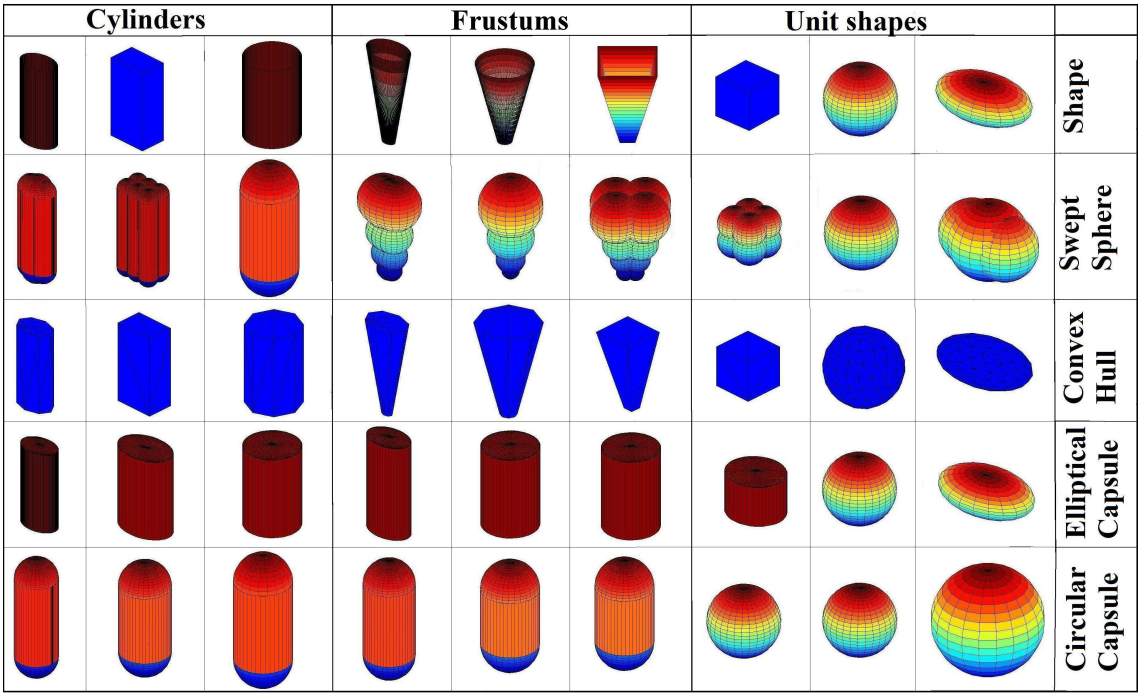


Figure 4.3: Bounding volume representation for test shapes. From left to right; elliptical cylinder, rectangular tube, circular cylinder, elliptical frustum, circular frustum, pyramidal frustum, cube, sphere, ellipsoid.

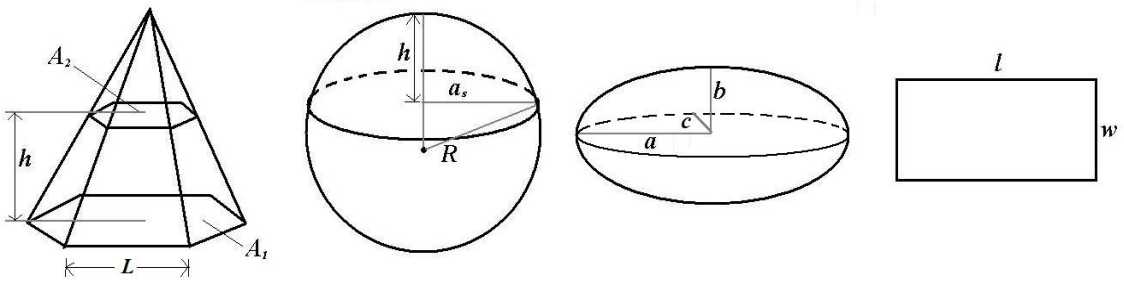


Figure 4.4: Notation for computing volume of frustum, spherical cap, ellipsoid and rectangular tube.

### Bounding volume performance

The bounding volume performance is compared in terms of the number of faces and the magnitude of volume of each bounding volume for the given test shape. For

Table 4.1: Bounding volume computation.

| Volumes | |
|---|---|
| Cylinder | $V = Ah$ |
| Frustum | $V = \frac{h}{3}\left(A_1 + A_2 + \sqrt{A_1 A_2}\right)$ |
| Sphere | $V = \frac{4}{3}\pi R^3$ |
| Spherical cap | $V = \frac{1}{6}\pi h\left(3a_s^2 + h^2\right)$ |
| Ellipsoid | $V = \frac{4}{3}\pi abc$ |
| Cube | $V = l^3$ |
| Areas | |
| Circle | $A = \pi R^2$ |
| Ellipse | $A = \pi ab$ |
| Rectangle | $A = lw$ |
| Regular $n$ sided polygon | $A = \frac{1}{4}nL^2 \cot\left(\frac{pi}{n}\right)$ |



both the convex hull and the swept sphere, different numbers of faces can be used to represent any shape. The different numbers of faces result in different volume magnitudes. The number of convex hull faces that would result in a difference of 5% of the original volume is chosen for comparison.

Figure 4.5 shows the number of faces for each bounding volume for each shape. The elliptical and circular capsules have the lowest number of faces used to represent each shape. Each shape uses three faces, with the exception of the sphere and ellipsoid, and for the circular capsule bounding volume, the cube is also represented by a single face. The average value of faces for the elliptical capsule is 2.6 while that of the circular capsule is 2.3. The convex hull uses the largest number of faces for each shape. Cylinders and frustums use similar numbers of faces while the ellipsoid and sphere use a significantly greater number of faces. The convex hull performs best for rectangular profiles, which require the least number of faces compared to the circular and elliptical profiled shapes. The average number of faces for the test shapes is 71.8 for the convex hull bounding volume. The swept spheres use a slightly higher number of faces for each shape than the two capsule bounding volumes. Swept spheres perform best for circular profiles, followed by elliptical profiles and perform the worst for rectangular profiles. The average number of faces for the swept sphere bounding volumes is 8.2. The convex hull bounding

volumes require a large number of checks, suggesting a high computational cost, while the other three bounding volumes require a much smaller number of self collision checks for each segment, suggesting a much lower computational cost.

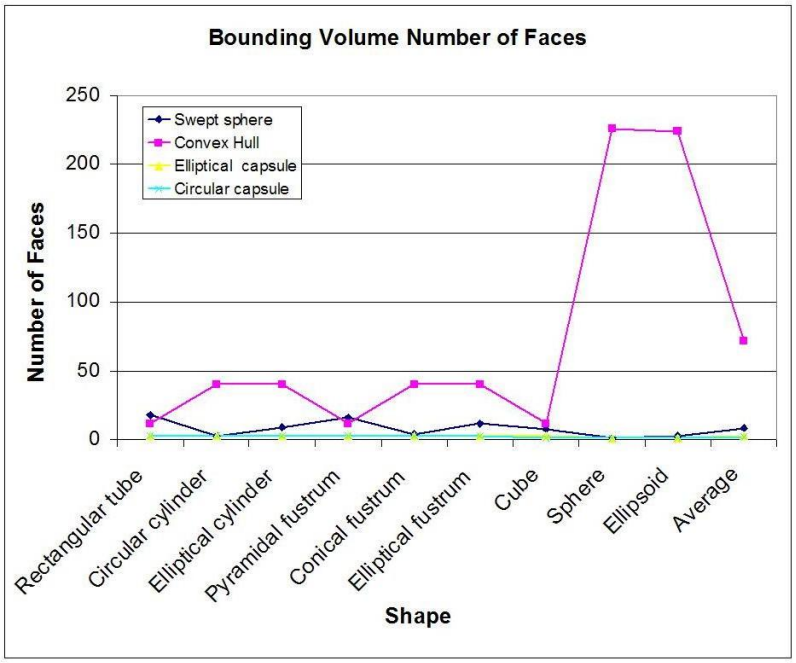


Figure 4.5: Number of faces required for different bounding volumes.

For the volume performance, circular capsules have the worst performance, greatly overestimating the volume of the shape. The circular capsule performs the worst for rectangular and elliptical profiles. On average it over estimates the volume of the shapes by an average difference of 173.0%. Convex hulls give a very good volume estimate of the shape, estimating the volume to within 3.5% difference from the actual volume. Better volume estimates can still be obtained by the convex hull though this requires a much higher number of faces. Both swept spheres and elliptical capsules fall in between the volume performance of the convex hull and circular cylinders. The elliptical capsule on average has a better performance than the swept sphere, having a difference of 75.8% from the actual volume. The swept sphere however performs better than the elliptical capsule when estimating the volume of frustums and the rectangular cylinder. The elliptical capsule performs best for circular and elliptical profiles. The swept spheres have an average volume difference of 93.7% from the actual shape. As with the convex hull, the swept sphere can achieve a better volume performance at the cost of increasing number of faces.

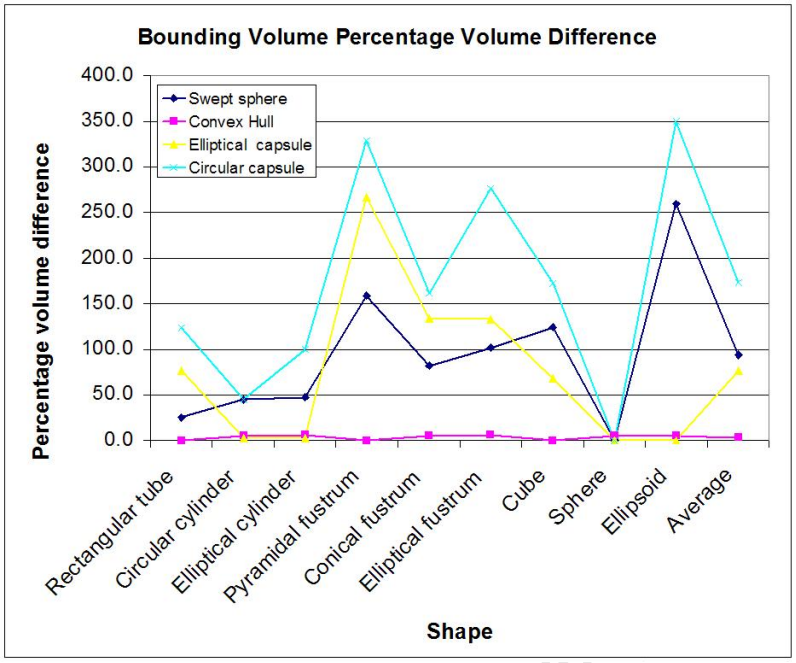


Figure 4.6: Percentage volume encompassed by different bounding volumes.

Table 4.2 shows a summary of the bounding volume performance in terms of geometry fit, number of faces and volume. The convex hull has the best fit to the geometry of the shape and the best volume fit, however it is highly computationally expensive as shown by the large number of faces required to represent the shape. It also has the limitation that a detailed model of the shape or object is required in order to implement the convex hull bounding volume. The circular capsule has the lowest number of faces required to represent the test object, however it has the worst performance with regard to volume and geometry fit. The elliptical capsule closely follows the circular capsule in having a very low number of faces for each object. It performs better than the circular capsule in terms of geometry and volume fit. The elliptical capsule also performs better than the swept sphere for the volume fit however performs worse than the swept sphere for the geometry fit. The elliptical capsule has the advantage of requiring only the major dimensions of an object to represent it unlike the swept spheres and convex hulls which require a detailed model. The elliptical capsule successfully provides a good representation of the object volume while being simple. Like the swept sphere it falls midway between more precise bounding volumes and less precise bounding volumes. It however has a number of advantages over the swept spheres, being easier to implement and providing a better volume fit with fewer number of faces.

Table 4.2: Performance of different bounding volumes.

| | Geometry fit | Average No. faces | Average % volume difference |
|---|---|---|---|
| Convex hull | Excellent | 71.8 | 3.5 |
| Swept sphere | Very Good | 8.2 | 93.7 |
| Elliptical capsule | Fair | 2.6 | 75.8 |
| Circular capsule | Bad | 2.3 | 173.0 |

### 4.3.2 Collision detection scheme

The humanoid collision detection scheme developed in this thesis and presented in [88] is detailed below. The arms and legs of a humanoid are usually circular in profile and so circular capsules can be used effectively as a bounding volume for these segments. The torso however is generally not circular in profile and so the elliptical capsule is better suited for modeling it. As shown in Figure 4.7, the arms, legs and neck of the humanoid are modeled using circular capsules. Spheres are used to represent joints. The body is modeled using elliptical capsules. If the body has a waist joint, two elliptical capsules are used. For the shoulder girdle, the clavicles are modeled using circular capsules surrounded by an ellipsoid.

Each capsule is made up of three sections; two end caps and a cylinder, and has the following properties [88]:

$l$ is the length of the cylinder,

$\boldsymbol{p_0}$ and $\boldsymbol{p_1}$ are the cylinder axis end points,

$\boldsymbol{u}$ is a unit vector in the direction of the cylinder axis.

For circular capsules:

$r$ is the radius of the circular cylinder.

For elliptical capsules:

$a$ is the width of the elliptical cylinder,

$b$ is the depth of the elliptical cylinder,

$c$ is the height of the ellipsoid.

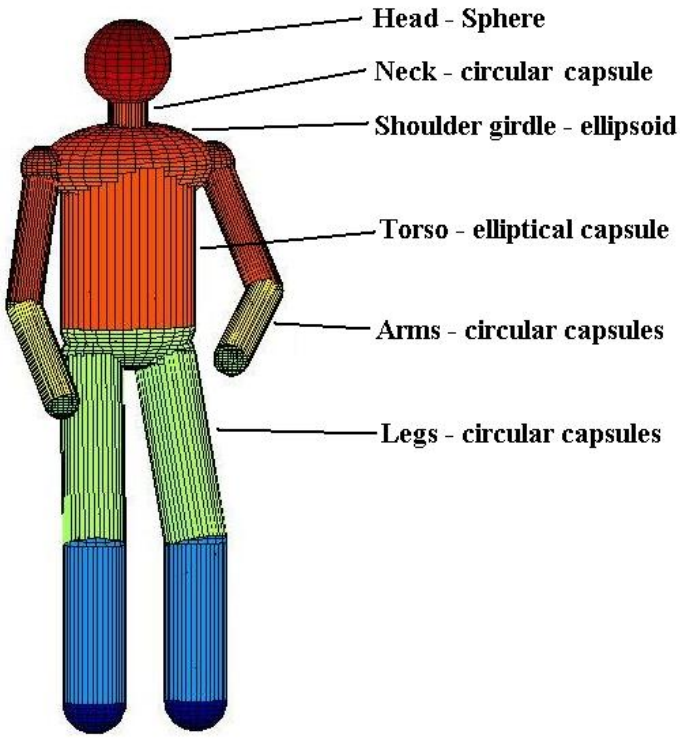


Figure 4.7: Bounding volume model of a typical humanoid body, using circular and elliptical capsules for self collision detection [88].

To apply the capsule models to a humanoid robot, the major dimensions of the humanoid are required. The width and depth of each torso segment of the humanoid are used for the parameters $a$, and $b$ of the elliptical cylinder and the ellipsoid. The width $a$ should also satisfy the condition:

$$a \leq \frac{L_{SG}}{2} - 10 \tag{4.34}$$

where $L_{SG}$ is the shoulder girdle length in millimeters. This is to ensure that the glenohumeral joint is attached to the shoulder girdle while remaining separate from the body to enable self collision detection between the upper arm and body. The length of the elliptical cylinder and the height of the ellipsoid are given by the length $L_T$ of the torso segment. [88]

$$L_T = l + 2c \tag{4.35}$$

The height $c$ of the ellipsoid is determined by the shape of the top and the bottom of the torso. For instance, if the torso is flat towards the top and bottom, a low value of $c$ is used, and if the torso has a curved top and bottom, a higher value of $c$ is used. For the arms and legs, the length and radius of each segment are used as inputs for the circular capsule parameters. [88]

Possible collisions between the humanoid segments are shown in Table 4.3. Depending on the range of the humanoid joint angles, certain segment collisions are unlikely or impossible. For example, collisions between the head and legs is theoretically possible, however due to the limited range of waist and hip joint movements in most humanoids, such a collision usually impossible for those humanoids. For connected segments such as the upper and lower arm, the joint limit of the elbow prevents the two segments from colliding. [88]

Table 4.3: Possible segment collisions. [88]

| | | | | | | | | | | |
|---|---|---|---|---|---|---|---|---|---|---|
| $UA_r$ | | | | | | | | | | |
| $LA_r$ | | | | | | | | | | |
| $UA_l$ | • | • | | | | | | | | |
| $LA_l$ | • | • | | | | | | | | |
| $B$ | • | • | • | • | | | | | | |
| $H, N$ | • | • | • | • | | | | | | |
| $T_r$ | • | • | • | • | ○ | ○ | | | | |
| $L_r$ | ○ | • | ○ | • | ○ | ○ | | | | |
| $T_l$ | • | • | • | • | ○ | ○ | • | • | | |
| $L_l$ | ○ | • | ○ | • | ○ | ○ | • | • | | |
| | $UA_r$ | $LA_r$ | $UA_l$ | $LA_l$ | $B$ | $H, N$ | $T_r$ | $L_r$ | $T_l$ | $L_l$ |

Key: • - likely collision, ○ - unlikely collision
$UA$ - Upper Arm, $LA$ - Lower Arm, $B$ - Body, $H$ - Head, $N$ - Neck, $T$ - Thigh, $L$ - Leg, $_r$ - right, $_l$ - left.



### Capsule collision detection

Each collision check is between two capsules representing the two test segments of the humanoid. The moving segments of the humanoid, the arms and legs, are represented by circular capsules. Collisions can thus be either between a circular capsule with an elliptical capsule or a circular capsule with another circular capsule. (See figure 4.8). For the simpler case of the head and the shoulder girdle, a sphere or an ellipsoid respectively are tested with the circular capsules that represent the moving humanoid segments. [88]

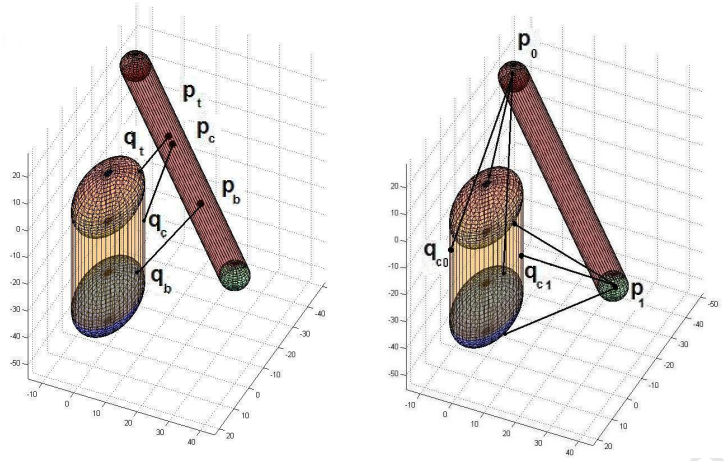


Figure 4.8: Collision test points of two capsules [88].

For collisions between two capsules, each collision check is then reduced to a collision check between a sphere in space and a capsule. This is done by finding the critical points that gives the closest distance between the two test capsules. There are three possible critical points representing the closest distance between the circular capsule (capsule P) with the cylindrical section ($c$) and the top ($t$) and bottom ($b$) end points of the second, circular or elliptical, capsule (capsule Q). A sphere is located at the critical points on the circular capsule P and collision checks are performed using spheres at the critical points as well as the end caps of capsule P. Figure 4.8 illustrates the concept. The algorithm for collision detection between two capsules is (see figure 4.9): [88]

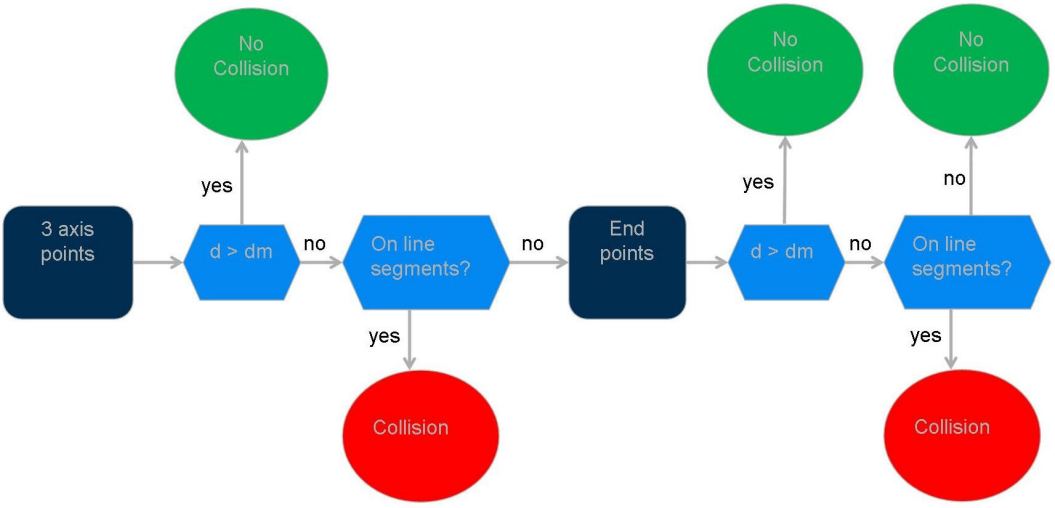


Figure 4.9: Collision detection algorithm for elliptical capsule bounding volume.

1. Find the three critical points $\boldsymbol{p_i}$ ( where $i = t,\ c,\ b$ ) on the axis of capsule P representing the closest points between the two capsules.

2. Find distance $d_i$ between each critical point $\boldsymbol{p_i}$ and the second test capsule, capsule Q.

3. If all of critical point distances are greater than their respective minimum distance $d_m$, no collision possible. i.e. $d_i > d_m$.

4. Else check if the critical points $\boldsymbol{p_i}$ lie within the capsule P line segment. i.e. $|\boldsymbol{p_i} - \boldsymbol{p_0}| + |\boldsymbol{p_i} - \boldsymbol{p_1}| = l_p$.

5. If any critical point lies on the capsule P line segment and its respective distance, $d_i > d_m$, then collision occurs. For the point $\boldsymbol{p_c}$, its corresponding closest point $\boldsymbol{q_c}$ on capsule Q must also lie on the capsule Q line segment for collision to occur. i.e. $|\boldsymbol{q_c} - \boldsymbol{q_0}| + |\boldsymbol{q_c} - \boldsymbol{q_1}| = l_q$.

6. Else find distances between the two end points of capsule P with all three sections of capsule Q.

7. If each distance is greater than its minimum distance $d_m$ then no collision occurs.

8. Else collision occurs. For collisions with the cylindrical section of capsule Q, the closest point to the capsule P end points must also lie on the capsule Q line segment for collision to occur.



The minimum distances are:

$d_m = r_p + r_q$ for two circular capsules,

and

$d_m = r_p$ for a circular capsule and elliptical capsule.

At most, for any two segments, nine checks are completed. Figure 4.10 shows all possible collisions between two capsules. Collisions are between the cylindrical sections of the capsules as well as the end points of the capsules. [88]

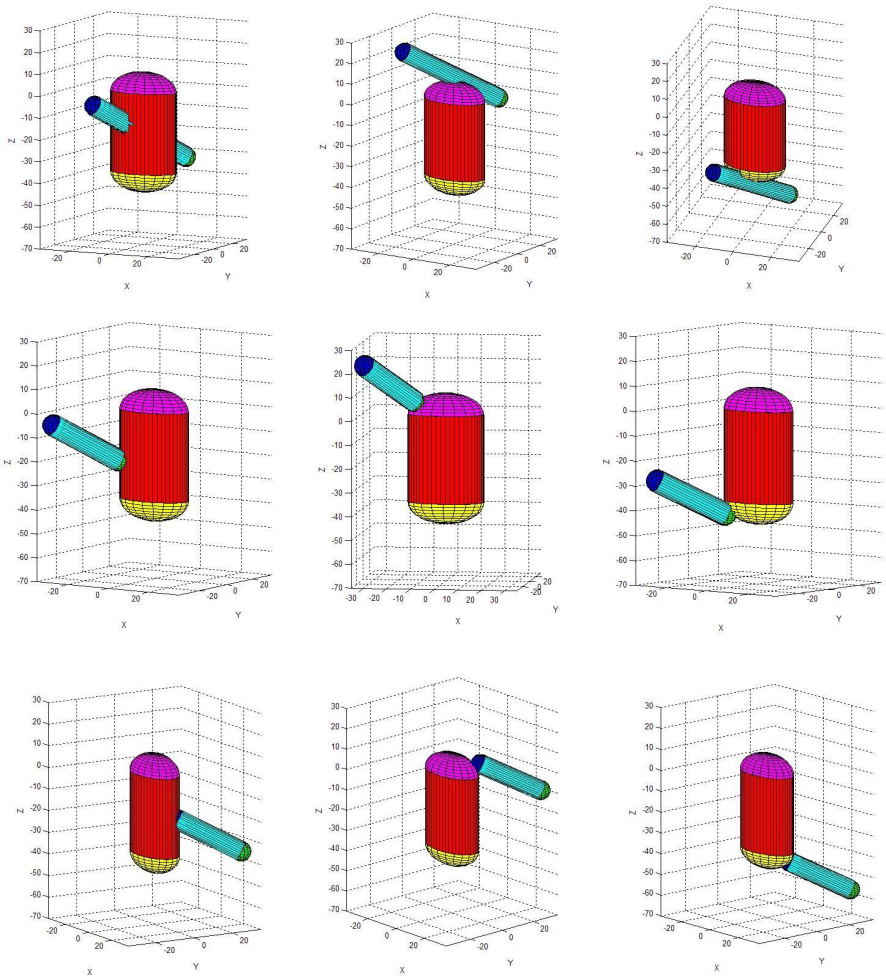

Figure 4.10: Nine possible collisions between two capsules [88].

### 4.3.3 Critical collision points

#### Critical points for circular capsule collisions

For two circular capsules, $P$ and $Q$ with axis having direction given by unit vectors $\boldsymbol{u_p}$ and $\boldsymbol{u_q}$, the critical points $\boldsymbol{p_c}$, $\boldsymbol{p_t}$ and $\boldsymbol{p_b}$ giving the shortest distance between the capsules are found as follows [88]:

The critical point $\boldsymbol{p_c}$ is (see figure 4.11):

$$\boldsymbol{p_c} = \boldsymbol{p_0} - \mu_c \boldsymbol{u_p} l_p \tag{4.36}$$

where [91] [92]:

$$\mu_c = \frac{((\boldsymbol{p_0} - \boldsymbol{q_0}) \times \boldsymbol{u_q} l_q) \cdot (\boldsymbol{n})}{\boldsymbol{n} \cdot \boldsymbol{n}} \tag{4.37}$$

and the common normal $\boldsymbol{n}$ between the two axis is [91] [92]:

$$\boldsymbol{n} = \boldsymbol{u_p} l_p \times \boldsymbol{u_q} l_q \tag{4.38}$$

If the axis are parallel then there is no unique value for $\boldsymbol{p_c}$.

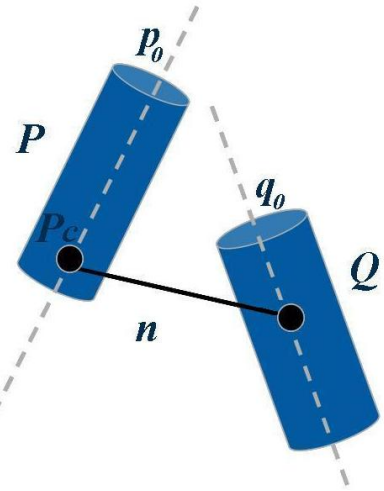


Figure 4.11: Circular capsules critical point.

The closest points $\boldsymbol{p_t}$ and $\boldsymbol{p_b}$ on the capsule P axis to the end points of capsule Q are given by:

$$\boldsymbol{p_t} = \frac{(\boldsymbol{q_0} - \boldsymbol{p_0}) \cdot (\boldsymbol{q_0} - \boldsymbol{p_1})}{l_p} \boldsymbol{u_p} + \boldsymbol{p_0} \tag{4.39}$$

$\boldsymbol{p_b}$ is found similarly. [88]

### Critical point for elliptical - circular capsule collisions

The circular cylinder is first projected onto the coordinate axis given by the elliptical capsule axis. The critical points $\boldsymbol{p_c}$ on the circular cylindrical capsule giving the shortest distance to the elliptical capsule are then found. (See figure 4.12).

To project the circular cylinder from the global coordinate frame ($\boldsymbol{X_0 Y_0 Z_0}$) onto the coordinate frame of the elliptical capsule ($\boldsymbol{X_e Y_e Z_e}$) the following rotation matrix is used:

$$\boldsymbol{R_0^e} = \begin{pmatrix} \boldsymbol{X_0 \cdot X_e} & \boldsymbol{Y_0 \cdot X_e} & \boldsymbol{Z_0 \cdot X_e} \\ \boldsymbol{X_0 \cdot Y_e} & \boldsymbol{Y_0 \cdot Y_e} & \boldsymbol{Z_0 \cdot Y_e} \\ \boldsymbol{X_0 \cdot Z_e} & \boldsymbol{Y_0 \cdot Z_e} & \boldsymbol{Z_0 \cdot Z_e} \end{pmatrix} \tag{4.40}$$

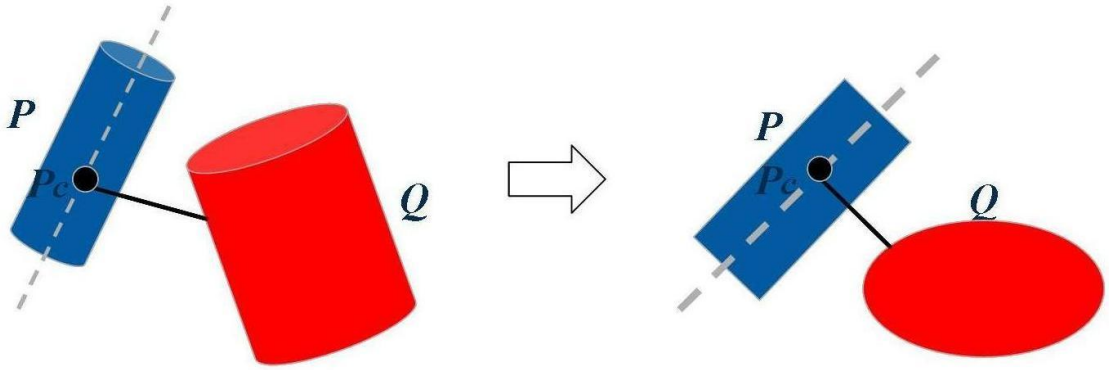


Figure 4.12: Circular and elliptical capsule critical point.

For the elliptical cylinder section; the parametric equations of the circular capsule, capsule P, axis are:

$$x_p = x_0 + \lambda u_x \tag{4.41}$$

$$y_p = y_0 + \lambda u_y \tag{4.42}$$

Substituting the parametric equations of the line into the ellipse equation, let:

$$F(\lambda) = \frac{(x_0 + \lambda u_x)^2}{a^2} + \frac{(y_0 + \lambda u_y)^2}{b^2} - 1 \tag{4.43}$$

Which is a quadratic equation in $\lambda$. The turning point $\lambda_c$ of the quadratic function is given by:

$$\lambda_c = \frac{-\beta}{2\alpha} \tag{4.44}$$

where $\beta$ is the coefficient of $\lambda$ and $\alpha$ is the coefficient of $\lambda^2$.

$\lambda_c$ gives the critical point and has the following properties (See figure 4.13):

If $F(\lambda_c) = 0$, then the point on the line given by $\lambda$ touches the ellipse.

If $F(\lambda_c) < 0$, then the point on the line given by $\lambda$ is inside the ellipse and the line therefore intersects the ellipse.

If $F(\lambda_c) > 0$, then the point on the line given by $\lambda$ is outside the ellipse and gives the closest distance to the ellipse. [88]



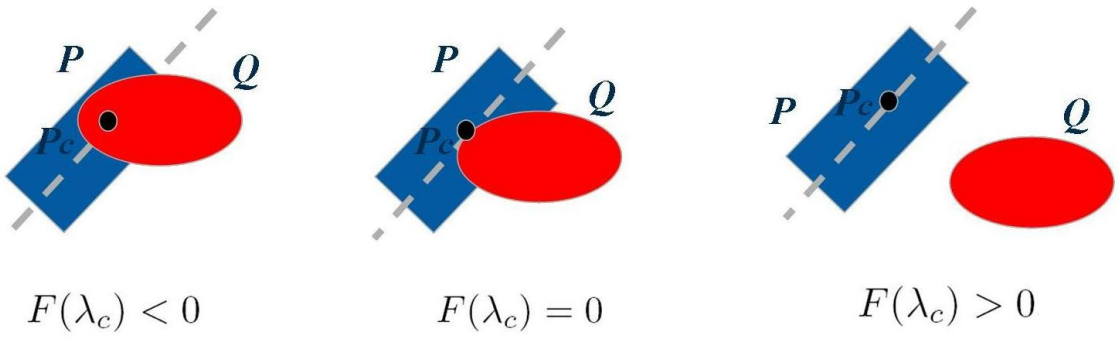


Figure 4.13: Circular and elliptical capsule critical point properties.

If the axis are parallel then use, $\boldsymbol{p_c} = [x, y, \frac{l_k}{2}]$.

For the critical point $\boldsymbol{p_t}$ between the circular cylinder with the ellipsoid end point, the formulation can be extended to an ellipsoid as follows [88]:

$$F(\lambda) = \frac{(x_0 + \lambda u_x)^2}{a^2} + \frac{(y_0 + \lambda u_y)^2}{b^2} + \frac{(z_0 + \lambda u_z)^2}{c^2} - 1 \tag{4.45}$$

and for the critical point $\boldsymbol{p_b}$:

$$F(\lambda) = \frac{(x_0 + \lambda u_x)^2}{a^2} + \frac{(y_0 + \lambda u_y)^2}{b^2} + \frac{(z_0 + \lambda u_z + l_q)^2}{c^2} - 1 \tag{4.46}$$

### 4.3.4 Computing the collision distance

For collision detection of capsules P and Q, five spheres representing capsule P critical points and end points are placed with centers $\boldsymbol{p_b}$, $\boldsymbol{p_t}$, $\boldsymbol{p_c}$, $\boldsymbol{p_0}$, $\boldsymbol{p_1}$. For the general case of a sphere with a capsule collision, let $\boldsymbol{s}$ represent the center of the sphere. [88]

#### Sphere - circular capsule collisions

The shortest distance between the center of the sphere $\boldsymbol{s}$ and the axis of capsule Q is (see figure 4.14):

$$d = \frac{|(\boldsymbol{s} - \boldsymbol{q_0}) \times (\boldsymbol{s} - \boldsymbol{q_1})|}{l_q} \tag{4.47}$$

The shortest distance between the center of the sphere $\boldsymbol{s}$ and the top end point of capsule Q is:

$$d = |(\boldsymbol{s} - \boldsymbol{q_0})| \tag{4.48}$$

The bottom end point is found similarly.

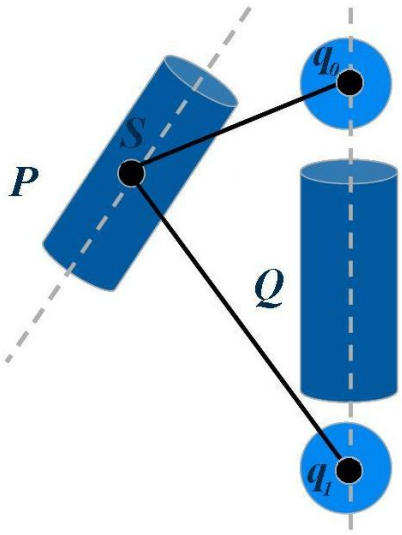


Figure 4.14: Collision testing of sphere and circular capsule



**Sphere - Elliptical capsule collisions**

To find the shortest distance between the sphere and the elliptical cylinder segment, the sphere is projected onto the plane given by the elliptical cylinder axis [88]. This then gives an ellipse and a circle. The closest point $k_s = (x_k, y_k)$ on the ellipse surface to the center of the circle $s = (x_s, y_s)$ occurs such that the line connecting the two points is normal to the ellipse [93]. (See figure 4.15).

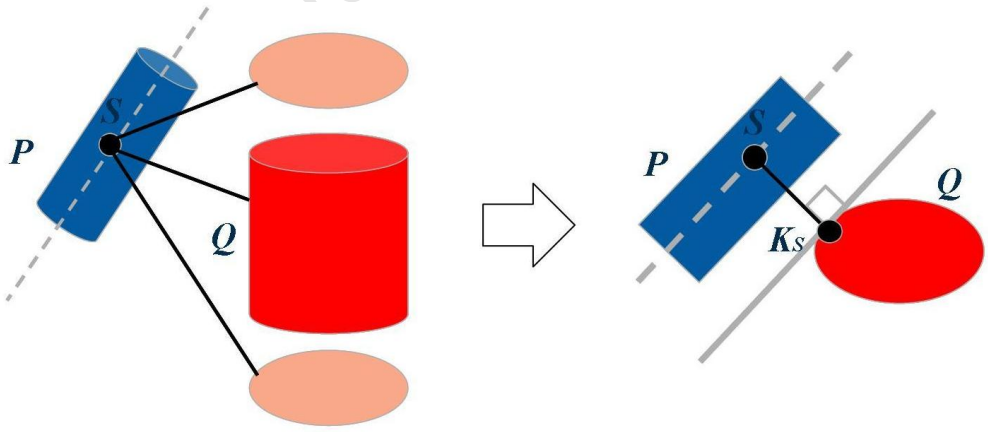


Figure 4.15: Collision testing of sphere and elliptical capsule.

The ellipse normal at any point $(x, y)$ on the ellipse is given by [93]:

$$\frac{1}{2}\nabla\left(\frac{x^2}{a^2}+\frac{y^2}{b^2}-1\right)=\left(\frac{x}{a^2},\frac{y}{b^2}\right) \tag{4.49}$$

Orthogonality condition gives [93]:

$$(x_s-x_k, y_s-y_k)=t\left(\frac{x_k}{a^2},\frac{y_k}{b^2}\right) \tag{4.50}$$

Replacing in the equation of the ellipse gives [93]:

$$\left(\frac{ax_s}{t+a^2}\right)^2+\left(\frac{by_s}{t+b^2}\right)^2-1=0 \tag{4.51}$$

Expanding the above equation gives a quartic polynomial in $t$. The largest root $t_{max}$ of the polynomial leads to the closest point [93]. The roots of a quartic polynomial can be obtained using a number of methods e.g. Newton-Raphson. However some programing languages such as MATLAB have built in functions that can be used to easily and quickly compute the roots. The closest points on the elliptical cylinder surface are then [93]:

$$x_k=\frac{a^2x_s}{t_{max}+a^2} \tag{4.52}$$

$$y_k=\frac{b^2y_s}{t_{max}+b^2} \tag{4.53}$$

To check if the point lies outside of the ellipse

$$F(k)=\frac{{x_k}^2}{a^2}+\frac{{y_k}^2}{b^2}-1 \tag{4.54}$$

If $F(k) > 0$ the point is outside the ellipse.

The distance is then:

$$d = |(\boldsymbol{s} - \boldsymbol{k_s})| \tag{4.55}$$

To calculate the distance from the sphere to the ellipsoid end caps, the above equations can be extended as follows [94]:

$$\left(\frac{ax_s}{t+a^2}\right)^2 + \left(\frac{by_s}{t+b^2}\right)^2 + \left(\frac{cz_s}{t+c^2}\right)^2 - 1 = 0 \tag{4.56}$$

For the bottom end cap:

$$\left(\frac{ax_s}{t+a^2}\right)^2 + \left(\frac{by_s}{t+b^2}\right)^2 + \left(\frac{c\,(z_s+l_p)}{t+c^2}\right)^2 - 1 = 0 \tag{4.57}$$

And the closest point $\boldsymbol{k_s} = (x_k, y_k, z_k)$ formulated as above. [88]

## 4.4 Self collision avoidance

Real time self collision avoidance algorithms can be found for humanoid robots. These algorithms, however, generally require a number of different factors to be guessed. These factors are not obvious and differ for each robot. For this thesis, self collision detection is not required in real time. For self collisions with collision distance, $d_{col}$, self collision avoidance is thus implemented by adjusting the glenohumeral abduction and / or elbow flexion joint angles, $\theta_{col}$, of the humanoids:

$$\theta_{col} = \theta_{col} \pm (10^o \times (|d_{col}| + 1)) \tag{4.58}$$

## 4.5 Motion transfer implementation

The motion transfer process was programmed and implemented using MATLAB. MATLAB functions to compute the forward kinematics, inverse kinematics, self collision detection and avoidance were developed in this study. The resultant motion plots and humanoid postures were outputted graphically. To transfer the human motion capture data to the humanoids, the process used in this study is as follows:

1. Scale the human motion capture data to the humanoid robot dimensions,
2. Estimate the initial upper body joint angles for the first motion frame,
3. Compute the weighted DLS differential inverse kinematics,
4. Compute the resultant humanoid posture using direct forwards kinematics,
5. Detect self collisions using the elliptical capsule method,
6. Compute the resultant joint angles with added self collision avoidance,
7. Compute the final humanoid posture using direct forwards kinematics.



In step 1, to scale the human motion capture data to the humanoid robot dimensions, the unit vector in the direction of each human body segment is found. This is then multiplied by the length of the appropriate body segment of the humanoid. To estimate the initial upper body joint angles of the humanoid in step 2, the desired posture of the robot is plotted graphically in MATLAB. Possible joint angles are then inputted into the forward kinematics equations of the humanoid. The resultant posture is plotted and compared to the desired posture. The joint angles are adjusted until the two figures overlap.

Differential inverse kinematics using the DLS jacobian and a joint limit weighting matrix has been used successfully to transfer human motion to the humanoid robot ASIMO in [72] and [73], showing its applicability to humanoid robots. This method is therefore also used in this study, in step 3 to transfer human motion to the five humanoids. Once the joint angles are determined in step three, they are inputted into the direct kinematics in step 4 to find the resultant postures of the humanoid upper bodies. Steps 5 and 6 then implement the self collision detection and avoidance formulated in this study. The final self collision free postures of the robots are then computed in step 7.

## 4.6 Summary

Forward kinematics modeling using the Denavit-Hartenberg parameters is used to compute the pose and velocities of the robot given the joint angles of the robot. The differential inverse kinematics is used to compute the desired joint angles of the robot while taking into account joint limits and avoiding self collisions. To detect self collisions, a new type of bounding volume and collision detection scheme is formulated. The scheme uses elliptical capsules to represent the torso of the robot. This bounding volume compares favorably to existing bounding volumes, giving a good fit to the volume of the actual object while being simple to implement.

# Chapter 5

# Humanoid Robots and Motion Capture Data



This chapter describes the humanoid robots and the human motion capture data used in the motion imitation study. Human motion capture data provides the input needed to make a humanoid robot dance. In order to obtain a valid comparison of robot capabilities, the motion capture data has to contain a large variety of motion and a sufficient number of motion capture markers. Some data sets however do not have enough motion markers. A method to estimate the location of such missing markers is thus formulated and described in this chapter.

## 5.1 The humanoid robots

The five serial structured humanoids chosen for this study have different numbers of DOFs with a differing range of motion. The humanoids are chosen based on their varying range of degrees of freedom (DOFs) and joint motion as well as availability of dimension information. Where dimension information for certain segments of the robots are not available, they are estimated based on the dimensions of the other body segments. The structure, dimensions and joint angle limits of each robot are described in this section.

### 5.1.1 Kinematics structures

**SURALP** (see figure 5.1) is a biped humanoid developed by the Sabanci University. Its upper body has a one DOF waist joint and two 6 DOF arms. SURALP has an angle offset at the glenohumeral joint and has no shoulder girdle. [47]

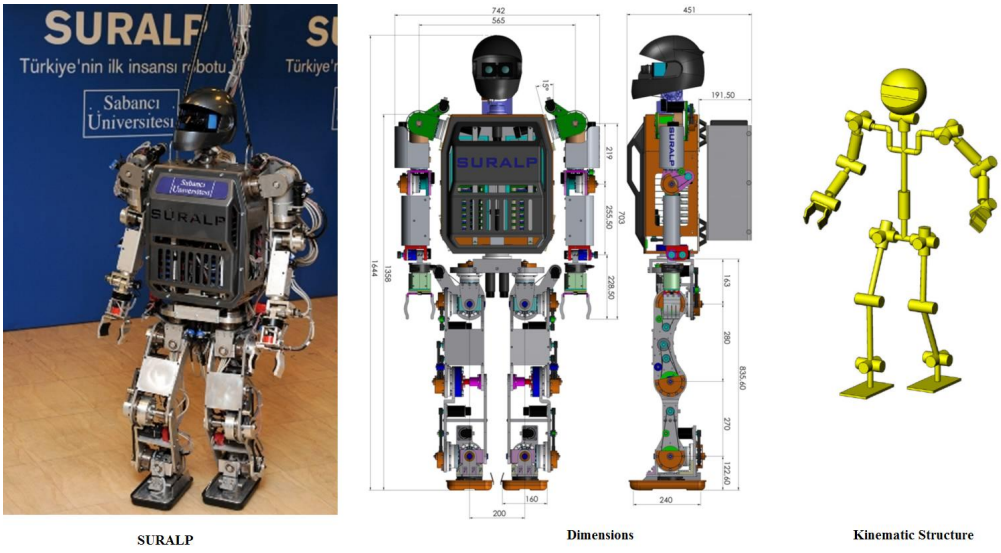


Figure 5.1: Humanoid SURALP [47].

**ARMAR**, developed by the University of Karlsruhe [29] is a humanoid upper body mounted on a wheeled base shown in figure 5.2. It has a 3 DOF waist and 7 DOF arms with no shoulder girdle. ARMAR has been used in a number of motion imitation attempts by researchers.

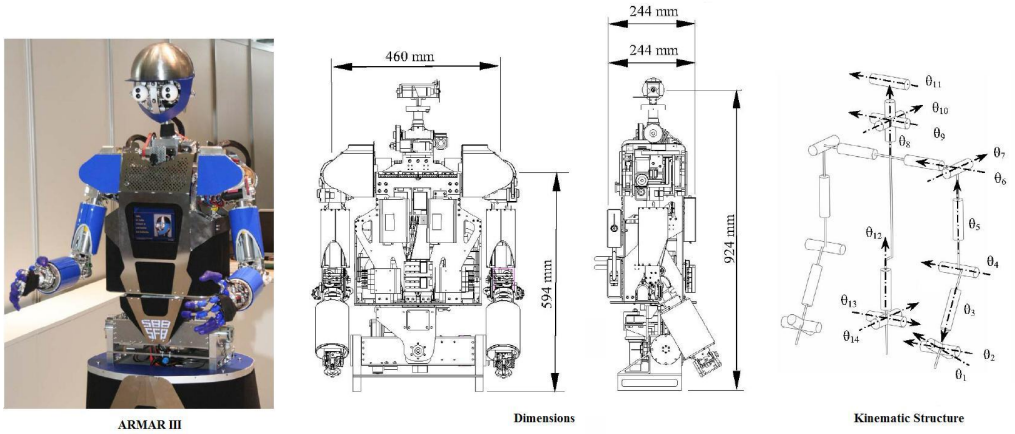


Figure 5.2: Humanoid ARMAR [29].

**WABIAN** shown in figure 5.3, developed by Waseda University [48] is a biped humanoid robot. It has a 3 DOF waist and 7 DOF arms with no shoulder girdle. WABIAN-2 has an angle offset at the glenohumeral joint.

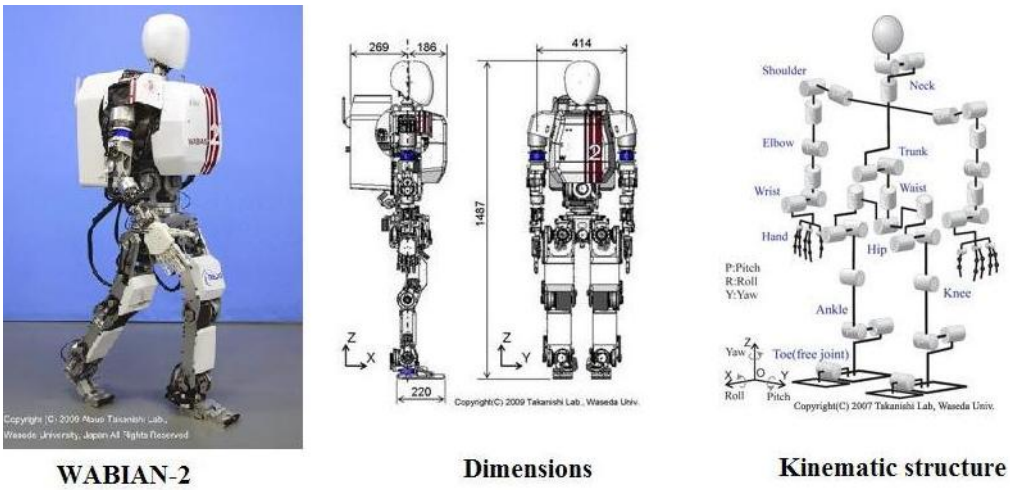


Figure 5.3: Humanoid WABIAN [95].

**HRP** is a biped humanoid, developed by the National Institute of Advanced Industrial Science and Technology and Kawada Industries. (See figure 5.4). It has a 2 DOF waist and a 6 DOF arm that has no shoulder girdle. it's waist is positioned at a large offset above the hip-line. HRP has been used in a number of motion imitation attempts by various researchers. [28] [96]

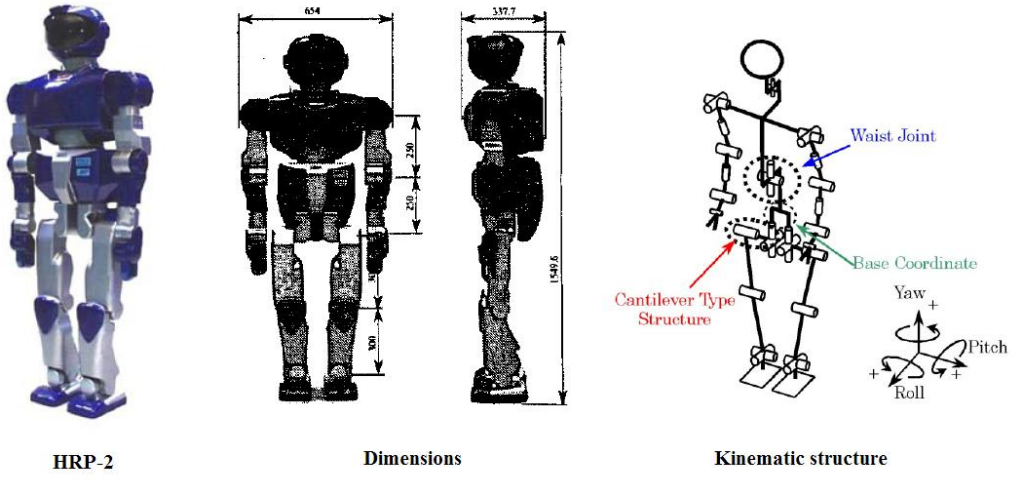


Figure 5.4: Humanoid HRP [97].

**WE-4RII** (see figure 5.5), developed by Waseda University is a humanoid upper body with 2 waist DOFs and 7 arm DOFs and 2 shoulder girdle DOFs. The shoulder girdle joints are offset a distance from the sternum position. Its glenohumeral joints have a shoulder offset angle. WE-4RII has been used in attempts to imitate human emotional expression through body language. [40] [67]

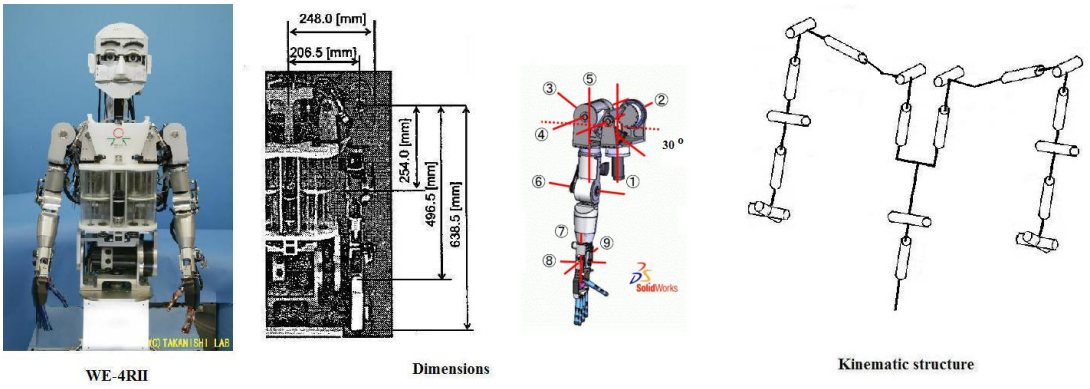


Figure 5.5: Humanoid WE-4RII [40].

### 5.1.2 Range of motion of joints

The range of motion of each humanoid, obtained from [47] [29] [48] [28] [96] [40] [67], is shown in table 5.1. As seen in the table, WE-4RII has two waist DOF's, however the range of these joints was not found. The humanoids selected exhibit a variety of differing ranges of motion for each joint. At the waist, the number of DOFs range from 1 to 3 DOFs. For the waist flexion joint, the humanoids have a range less than that of the average human. Waist lateral flexion for the humanoids falls both above and below the range of the average human. Waist rotation of the humanoids varies largely but remains above that of humans.

Only one humanoid selected has a shoulder girdle. Its protraction is less than that of a human, however elevation is significantly higher than that of humans. Each humanoid has 3 glenohumeral DOFs. The overall glenohumeral abduction range is less that that of humans, while glenohumeral rotation is equal or greater than that of humans and glenohumeral flexion has an overall range than varies from below that of humans to above the human range. Elbow flexion also varies from below to above the range of the average human. Elbow protraction is either equal or above the human range.

Table 5.1: Humanoid joint range of motion. Key for abbreviations: WT - waist, SG - shoulder girdle, GH - glenohumeral joint, EL - elbow joint, RU - radioulna joint, WR - wrist joint. [47] [29] [48] [28] [96] [40] [67]

| | Joint range (degrees) | | | | | |
|---|---|---|---|---|---|---|
| DOF | Human | SURALP | ARMAR | WABIAN | HRP | WE-4RII |
| WT Flexion | −30 to 90 | - | −10 to 60 | −30 to 45 | −5 to 60 | ? to ? |
| WT Lateral Flexion | −35 to 35 | - | −20 to 20 | −50 to 50 | - | - |
| WT Rotation | −30 to 30 | −40 to 40 | −180 to 180 | −180 to 180 | −45 to 45 | ? to ? |
| SG Protraction | −30 to 30 | - | - | - | - | −18 to 25 |
| SG Elevation | 0 to 35 | - | - | - | - | 0 to 120 |
| GH Flexion | −60 to 180 | −180 to 180 | −10 to 180 | −180 to 180 | −60 to 180 | −180 to 200 |
| GH Abduction | −75 to 180 | −23 to 135 | −45 to 180 | −17 to 196 | −30 to 90 | −25 to 180 |
| GH Rotation | −90 to 90 | −180 to 180 | −180 to 180 | −180 to 180 | −90 to 90 | −80 to 115 |
| EL flexion | 0 to 150 | −49 to 110 | −10 to 150 | −10 to 130 | 0 to 135 | 0 to 160 |
| RU Pronation | −90 to 90 | −180 to 180 | −90 to 90 | −180 to 180 | −90 to 90 | −180 to 180 |
| WR Abduction | −20 to 30 | - | −30 to 30 | −47 to 47 | - | −55 to 65 |
| WR Flexion | −70 to 80 | −16 to 90 | −60 to 60 | −115 to 41 | −90 to 90 | −100 to 115 |

### 5.1.3 Self collision models

Figure 5.6 shows the collision models for each humanoid upper body. For humanoids with some missing major dimensions, these dimensions were estimated based on the scaling the given dimensions on the dimensioned drawing. Elliptical and circular capsules are used to represent the humanoid form. Each moving segment of the humanoid is represented by a single circular capsule, while the torso is represented by elliptical capsules. The segments modeled are the: upper torso or chest, lower torso or abdomen, head, neck, shoulder girdle, upper arm, and lower arm.



## 5.2 Motion capture data sets

Two different motion capture data sets are used in this study. The first is the CSIR data set which has a large range of movements but lacks some important motion capture markers. The Ohio State University (OSU) data set has a larger number of markers but has a limited range of movements. This data set is used to validate estimates of unavailable markers of the CSIR data set.

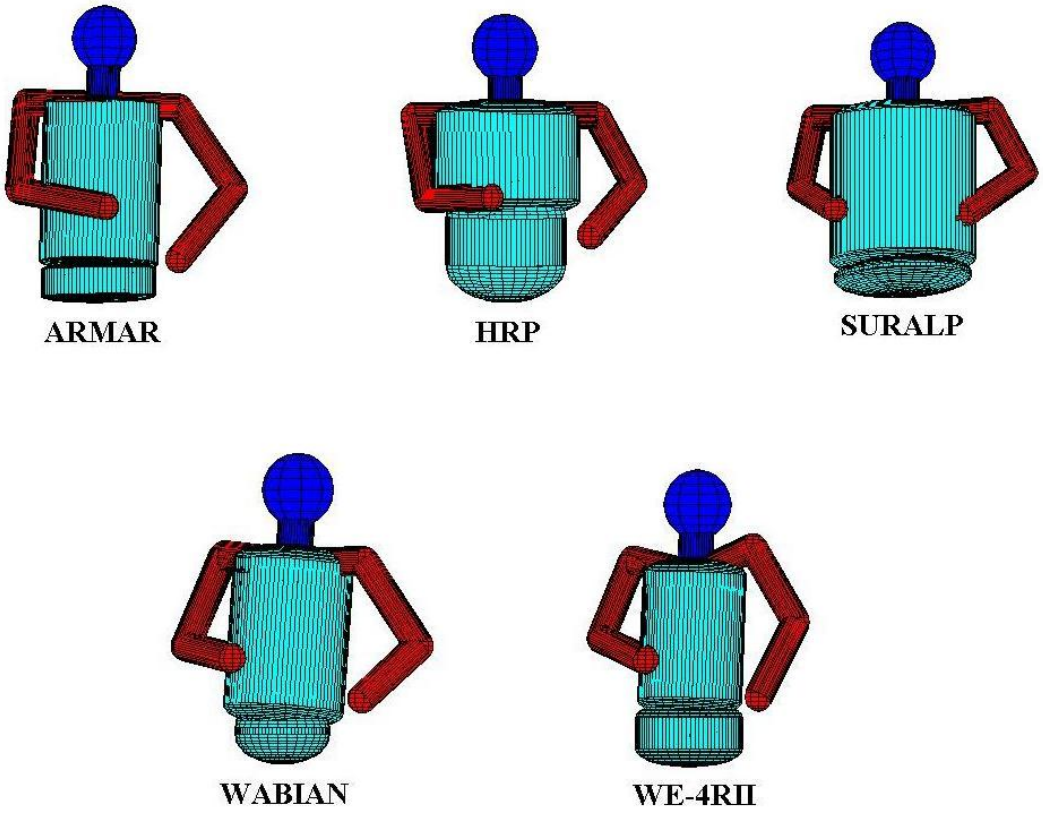


Figure 5.6: Collision models of five humanoid upper bodies.



### 5.2.1 Data set A - African dance

Data set A was captured by the CSIR and the University of Johannesburg. The visual motion capture system which was used consists of 16 passive markers and six independent digital video cameras capturing at 50Hz. The African dance routine was performed inside a pre-calibrated area. The motion capture data was then post-processed to manually identify the various markers. Each marker was plotted manually for each individual frame, for each camera. The current processing time for the motion capture data is six person hours per second of video footage. To deal with noise in the motion capture data, the data is smoothed using a fourier transform. Figure 5.7 shows the human motion capture setup and the location of the motion markers on the dancer. The available motion capture data from this setup gives the $x$, $y$, and $z$ position coordinates of the wrist, elbow and glenohumeral joint.


Figure 5.7: Human dancer with 16 motion capture markers located at: F - forehead, C - chin, GH - glenohumeral joints, E - elbow joints, W - wrist joints, H - hips, K - knees, A - ankles and Ft - feet.

The CSIR data set has very few motion capture markers, when compared to other motion data sets. The CSIR data does not have information for the position of the sternum or the hand. As the sternum location is of importance in motion transfer to humanoids, its position is estimated in section 2.3. The hand markers would yield the orientation of the lower arm. However the lower arm position information alone is sufficient for motion transfer. Despite the lack of some motion capture markers, this data set does have a large range of different movements which other data sets tend to lack. A wide range of waist movements are found in the data, including bending and twisting of body at the waist. Arms are raised and lowered at different speeds and follow many different paths of motion. Shoulder girdle movements are also observed in the dance including shrugging and forwards and backwards motions. Throughout the dance no contact between various body segments is made however segments do come in close proximity at certain times.

### 5.2.2 Data set B - OSU Performance 1

Data set B is a performance from the OSU Advanced Computing Center for the Arts and Design (ACCAD) motion capture library. The ACCAD lab uses a Vicon 8 optical motion capture system with 14 cameras. The sizes of the reflective markers vary from 28mm, 14mm, 12mm, and the smallest, 6mm. They mainly use the 14mm size markers. The smallest markers are used when clusters of markers have to be positioned closely together, as done with hand and facial markers. Markers are located as shown in figure 5.8. The ACCAD Performance 1 data set used in this study does not have a large variety of movements. It however does makes use of a large number of markers which can be used to validate the estimation of missing markers in data set A. [98].

Figure 5.8: OSU ACCAD Motion capture markers.

## 5.3 Missing motion markers

The sternum forms an important reference for arm movements. Since a marker for the sternum is not available from the motion capture data set A, the position of the sternum for this data set is estimated. The estimation technique developed in this thesis and presented in [99] is detailed here.

### 5.3.1 Geometric sternum calculation

A way to find the position of the sternum is to use the geometry of the body and the hip markers and the glenohumeral joint markers. The sternum is found at the intersection of the spine and the left and right clavicles. To find the intersection point, the spine can be taken as a link with a three-DOF joint centered at the mid-hip position. the mid-hip position is then taken as the origin. The clavicles can be taken as links with two-DOF joints centered at the glenohumeral joints $\begin{pmatrix} a_L & b_L & c_L \end{pmatrix}$ and $\begin{pmatrix} a_R & b_R & c_R \end{pmatrix}$. See figure 5.9. The workspace of each link is a sphere centered at the joint. The intersection of the three workspaces gives the two possible sternum positions. See figure 5.10. [99]

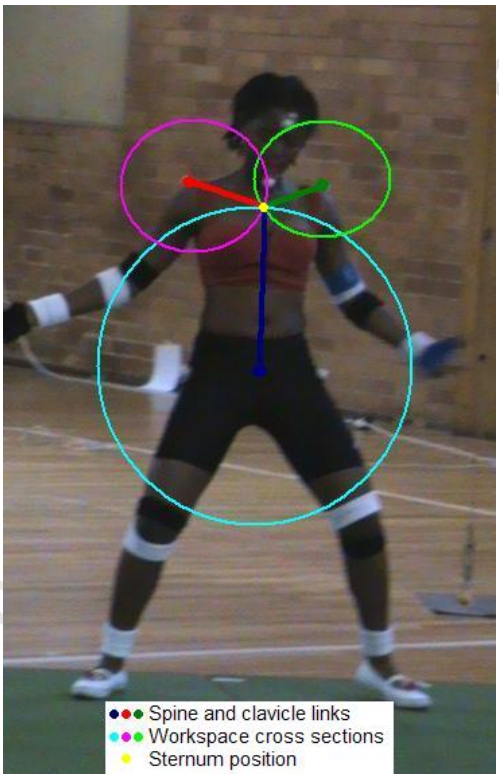


Figure 5.9: Dancer showing the spine and clavicle links, and their workspace cross-sections, centered at the glenohumeral markers and mid-hip point, to find the position of sternum [99].

The two points are calculated as follows [99]. The equation of the spine sphere is given by:

$$R_w^2 = x^2 + y^2 + z^2 \tag{5.1}$$

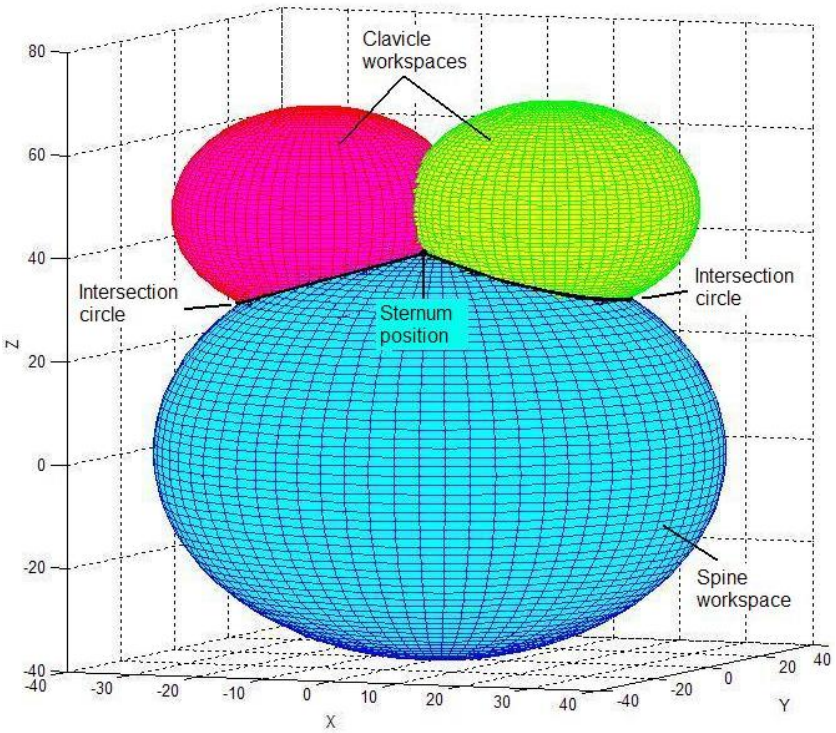


Figure 5.10: Spine and clavicles' spherical workspaces and intersection circles to find the sternum position [99]

The equation of either shoulder girdle sphere is:

$$R^2 = (x-a)^2 + (y-b)^2 + (z-c)^2 \tag{5.2}$$

The intersection of the spine sphere and the clavicle sphere is a circle. Expanding and combining the equations above gives the equation of the plane on which the circle of intersection of the spine and clavicle spheres lies. The plane is:

$$d_p = a_p x + b_p y + c_p z \tag{5.3}$$

where:

$$d_p = \frac{a^2 + b^2 + c^2 + R_w^2 - R^2}{2 \times \sqrt{a^2 + b^2 + c^2}} \tag{5.4}$$

$$a_p x + b_p y + c_p z = \frac{ax + by + cz}{\sqrt{a^2 + b^2 + c^2}} \tag{5.5}$$

The normal of the plane $\boldsymbol{n}_p$ is:

$$\boldsymbol{n}_p = \begin{pmatrix} a_p & b_p & c_p \end{pmatrix} \tag{5.6}$$

The radius of the circle of intersection $r_I$ is:

$$r_I = \sqrt{R_w^2 - d_p^2} \tag{5.7}$$

and the position vector of the center of the circle of intersection $\boldsymbol{C}$ is:

$$\boldsymbol{C} = d_p \times \boldsymbol{n}_p \tag{5.8}$$

The plane and circle of intersection is found for each clavicle link. Finding the intersection of the right and left clavicle circles of intersection then gives the two possible sternum positions as shown in figure 5.11. To find the points, first find the line of intersection of the left and right intersection planes. The intersection of one of the circles with the line then gives the two possible sternum points. The line is given by the vector:

$$\boldsymbol{V}_I = \boldsymbol{n}_{pL} \times \boldsymbol{n}_{pR} \tag{5.9}$$

and the position vector $\boldsymbol{P2}$ of a point on the line. A point on the line is given by setting $z = 0$ in the equations of the two intersection planes and solving the equations simultaneously for $x$ and $y$:

$$y_2 = \frac{a_{pR} d_{pL} - a_{pL} d_{pR}}{a_{pR} b_{pL} - a_{pL} b_{pR}} \tag{5.10}$$

$$x_2 = \frac{d_{pL} - b_{pL} y_2}{a_{pL}} \tag{5.11}$$

The line is:

$$\boldsymbol{P}_{line} = \boldsymbol{P2} + t\boldsymbol{V}_I \tag{5.12}$$

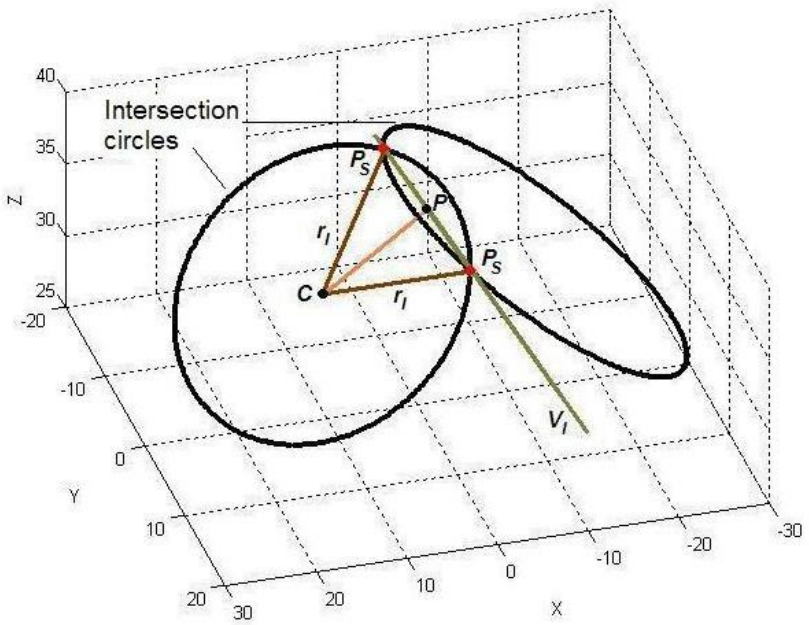


Figure 5.11: Intersection circles of the spine workspace with the two clavicle workspaces showing the two possible sternum points $\boldsymbol{P_s}$, the intersection circle center $\boldsymbol{C}$, the intersection circle radius $r_I$, the line of intersection $\boldsymbol{V_I}$ and the mid point $P$ between the two possible sternum points [99].

The minimum distance $D$ between the center of an intersection circle and the line by using the position vectors of two points on the intersection line $\boldsymbol{P2}$ and $\boldsymbol{P3}$ and the position vector of the center of the intersection circle $\boldsymbol{C}$:

$$D_{min} = \frac{|(\boldsymbol{P2} - \boldsymbol{P3}) \times (\boldsymbol{P2} - \boldsymbol{C})|}{|\boldsymbol{P2} - \boldsymbol{P3}|} \tag{5.13}$$

The minimum distance lies on the vector given by:

$$\boldsymbol{V}_{min} = \boldsymbol{V}_I \times \boldsymbol{n}_p \tag{5.14}$$

The midpoint between the two possible sternum points is:

$$\boldsymbol{P} = \boldsymbol{C} + D_{min}\boldsymbol{V}_{min} \tag{5.15}$$

The distance between this midpoint and the sternum positions is:

$$D = \sqrt{r_I^2 - D_{min}^2} \tag{5.16}$$

The position vectors of the two possible sternum points are then given by:

$$\boldsymbol{P}_s = \boldsymbol{P} \pm D\boldsymbol{V}_I \tag{5.17}$$

To choose between the two sternum positions, the resultant DOFs for each position are calculated and the one that keeps the sternum to the front of the body is selected (ie the point with more positive y values). [99]



### 5.3.2 Link length estimates

For the sternum position formulations, the length of the spine and the two clavicles is required as input into the kinematic or geometric equations. The link lengths of the spine and clavicles are estimated using the geometry of the body. The positioning and size of markers (i.e. not at joint center of rotation and large size markers mean measured distance between markers has error) gives justification for a variable link length estimate. (See figure 5.12). [99]


Figure 5.12: Link length estimates.

The clavicle link lengths are equivalent to the distances between each glenohumeral marker and the sternum. From the body geometry, the distance between the two glenohumeral markers $L_g$ is less than the combined clavicle link lengths. The link lengths $L_{cl}$ of the clavicles are therefore taken as [99]:

$$L_c = \frac{L_g + k_c\,(A_g - M_g)}{2} \tag{5.18}$$

where:

$A_g$ is the average female shoulder breath obtained from [23] and is equal to 395mm

$M_g$ is the average distance between the glenohumeral joints for all the motion capture frames.

The spine link length is the distance between the mid-hip point and the sternum. From the body geometry, the spine link length is less than the distance $L_{gs}$ between the mid-hip and mid-glenohumeral joint points. The spine link length $L_s$ is thus taken as [99]:

$$L_s = L_{gs} - k_s(A_{gs} - M_{gs}) \tag{5.19}$$

where:

$A_{gs}$ is the average female shoulder height obtained from [23] and is equal to 555mm

$M_{gs}$ is the average distance between the mid-hip and mid-glenohumeral points for all the motion capture frames.

If $L_s < L_{s_{min}}$, then:

$$L_s = L_{s_{min}} \tag{5.20}$$

where

$$L_{s_{min}} = L_{gs} - \sqrt{L_c^2 - \left(\frac{L_g}{2}\right)^2} \tag{5.21}$$

The link lengths above serve as the inputs into the sternum formulation and their accuracy determines the accuracy of sternum position results.

### 5.3.3 Testing of sternum formulation

To test the formulation the calculated sternum positions are compared using the actual sternum positions of data set B. The formulation rests on the performance of the link length estimates. Given the correct link lengths, the formulation results in the correct sternum position. The error in the link lengths and the resulting sternum position errors are thus examined.

### Link length error

The spine and clavicle links length errors are calculated as the difference between the estimated and the actual link lengths. For the spine, the mean error is $-0.1cm$ with a standard deviation of 0.9, the right clavicle has a mean error of $-0.4cm$ and standard deviation of 1.3 and the left clavicle has a mean error of $0.5cm$ with standard deviation of 1.1. Figure 5.13 shows the error distribution for each link. The three plots have similar profiles. As both mean and standard deviation of the plots are low, the estimates obtained from the sternum formulation are considered as acceptable.

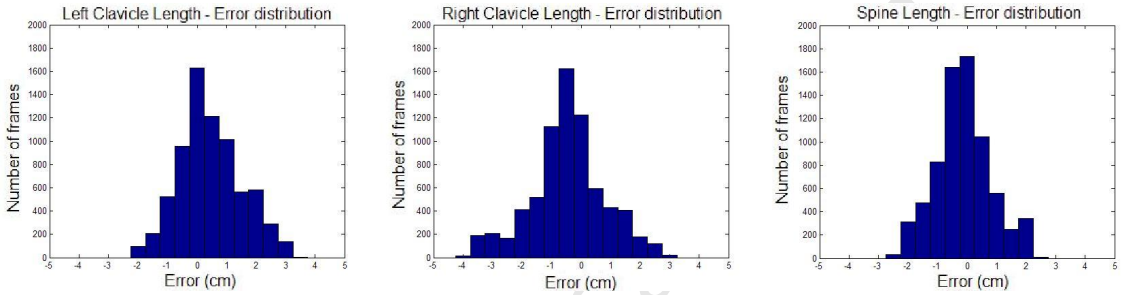


Figure 5.13: Error distribution for link length estimates.

### Sternum position error

Figure 5.14 shows the $xyz$ positions of the sternum marker and the calculated positions of the sternum. The plots for the calculated and actual sternum positions are similar, with slight offset between measured and actual positions. [99]

Figures 5.15 shows the error distribution for the $xyz$ coordinates of the sternum estimate. For the $x$ coordinate, the mean error is $0.9cm$ with a standard deviation of 0.7, the $y$ has a mean error of $0.9cm$ with a standard deviation of 0.7 and the $z$ has a mean error of $0.7cm$ with a standard deviation of 0.6. The combined error in distance between the actual and sternum estimate has a mean of $1.7cm$ and standard deviation of 0.8. Taking into account that the motion capture process itself does not result in highly accurate marker positions, the sternum formulation estimates the positions well enough that they can be used in the absence of the actual data. [99]

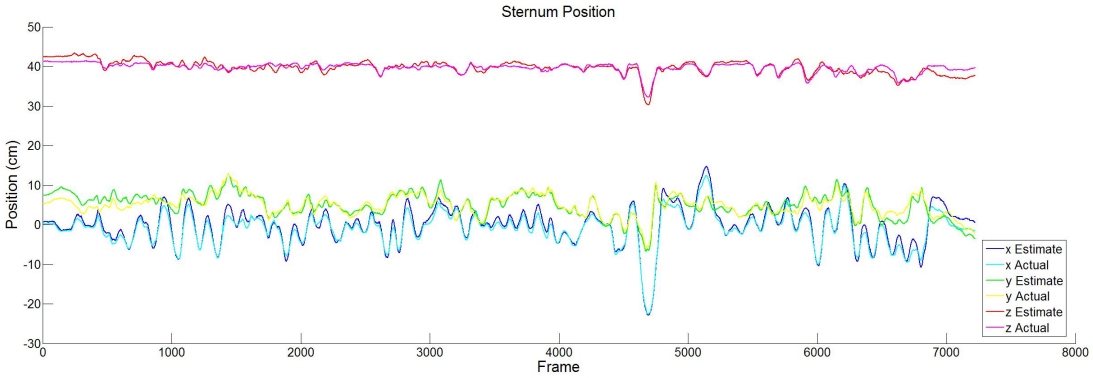


Figure 5.14: Actual and calculated sternum positions of a test motion capture data set [99].

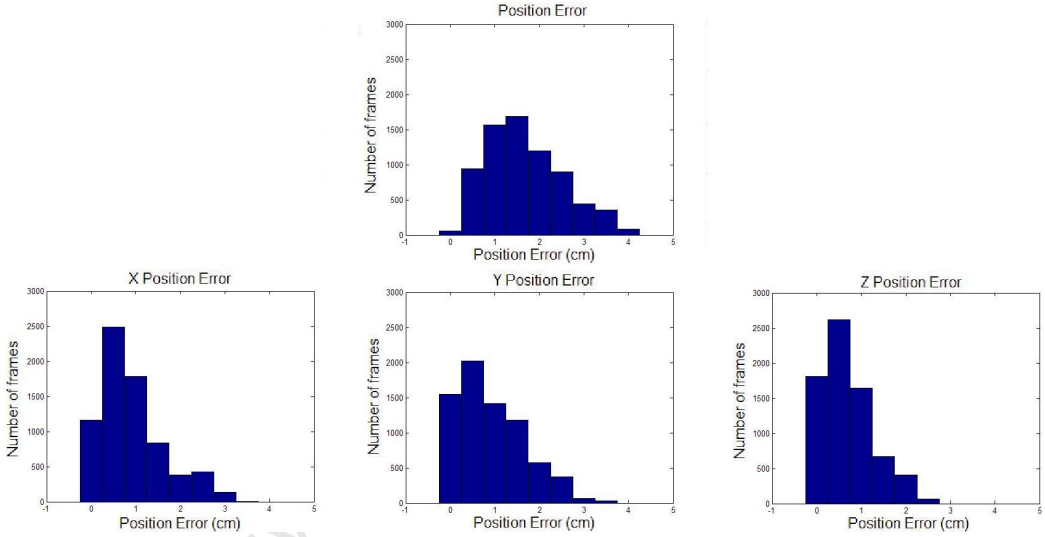


Figure 5.15: Errors in the sternum position estimate.

## 5.4 Summary

Five humanoid robots are used in this study. Two motion capture data sets are used in this study. One contains a wide variety of movements but has missing sternum position markers, while the other has a large number of markers but contains a limited range of movements. The missing sternum position is calculated using the spine workspace and the clavicle workspaces. Testing of the method shows that the calculated sternum position corresponds well to the actual sternum position of the human. The formulation can therefore be used to produce a sternum position in place of an actual sternum motion capture marker.

# Chapter 6

# Dancing Humanoids



Humanoid robots are designed such that they mimic the functionality of the human body. To test how well they do this, the motion imitation abilities of five humanoid upper bodies are compared using a dance as a case study. The dance is obtained from human motion capture and transfered to the humanoid models as described in the previous chapters. The resulting error between the actual robot position and the desired position is examined in this chapter. The joint angles, joint limits, number of joints and self collisions are examined to determine how they affect the motion imitation results.

## 6.1 Motion imitation analysis of humanoid robots

The humanoids used in the motion imitation study are ARMAR, HRP, SURALP, WABIAN and WE-4RII. The motion transfer procedure outlined in chapter 4, section 4.5 was programmed in MATLAB and applied to the humanoid robots. Motion imitation is conducted using the weighted damped least squares (DLS) differential inverse kinematics as described in section 4.2.2. Joint limit constraints are added as a weighting matrix to keep the motion with the movable range of the robot joints.

Self collision detection, as formulated in section 4.3, is applied and self collision avoidance achieved by adjusting the glenohumeral and elbow joint angles as formulated in section 4.4. Plots of the resultant robot postures are generated using MATLAB. The motion without self collision avoidance is first discussed, followed by the motion imitation results incorporating self collision avoidance. Factors that

possibly influence or limit the positioning results of joints include; joint limits, location of joints, the number of degrees of freedom (DOFs), and self collisions.

The motion imitation position error distribution for each link of each robot is discussed in detail. The links are; the spine whose position is measured at the sternum location; the clavicles, measured at the glenohumeral joint locations; the upper arms, measured at the elbow joint locations; and the lower arms, measured at the wrist joint locations. The implications of each distributions' shape, spread, height and mode are also discussed. The shape can be right skewed, symmetrical or left skewed. Slight and distinct are used to distinguish between low and high levels of skewness. The spread is graded as; very low, low, moderate, high, very high, extremely high; measured in increments of 10. The height, i.e. the frequency of the modal value, is graded as; extremely low, very low, low, medium, high, very high; measured in increments of 200.

Peaks and troughs in the position error data are then investigated to determine the factors that influence high and low error results. Peaks, $P$, and troughs, $T$, are defined according to the scaled standard deviation, distance from the mean error, and from the upper error and lower error limits.

Peaks are defined as:

$$P > M_e + S_e \times 2 \tag{6.1}$$

and

$$P > E_{max} - S_e \times 0.2 \tag{6.2}$$

where:

$S_e$ is the standard deviation

$M_e$ is the mean error

$E_{max}$ is the upper error limit.

While troughs are:

$$T < M_e - S_e \times 2 \tag{6.3}$$

and

$$T < E_{min} + S_e \times 0.2 \tag{6.4}$$

where:

$E_{min}$ is the lower error limit.

The overall motion of the humanoids is then compared by investigating the mean and standard deviation of the position error of each joint for each robot. The range of motion used by each humanoid is compared to determine the comparative significance of each joint and its range to motion imitation. Differences in the upper bodies that influence the number of collisions that occur are investigated. The mean and standard deviation of the self collision free motion is compared to determine the effects of self collisions.



### 6.1.1 ARMAR

ARMAR, has good motion following abilities due to the high motion range of its waist joints and glenohumeral joints. It has limitations due to the lack of a shoulder girdle. The human motion imitation performance is discussed in detail below.

#### Error distribution

The position error distributions for ARMAR are shown in figure 6.1, and the description is shown in table 6.1. ARMAR has a mean error distribution with a distinct right skewed shape that has distinct limit to the left at about 6cm and a mode of 8cm. The position of the left limit indicates that ARMAR has at least one significant limiting factor in its overall positioning abilities. The low spread

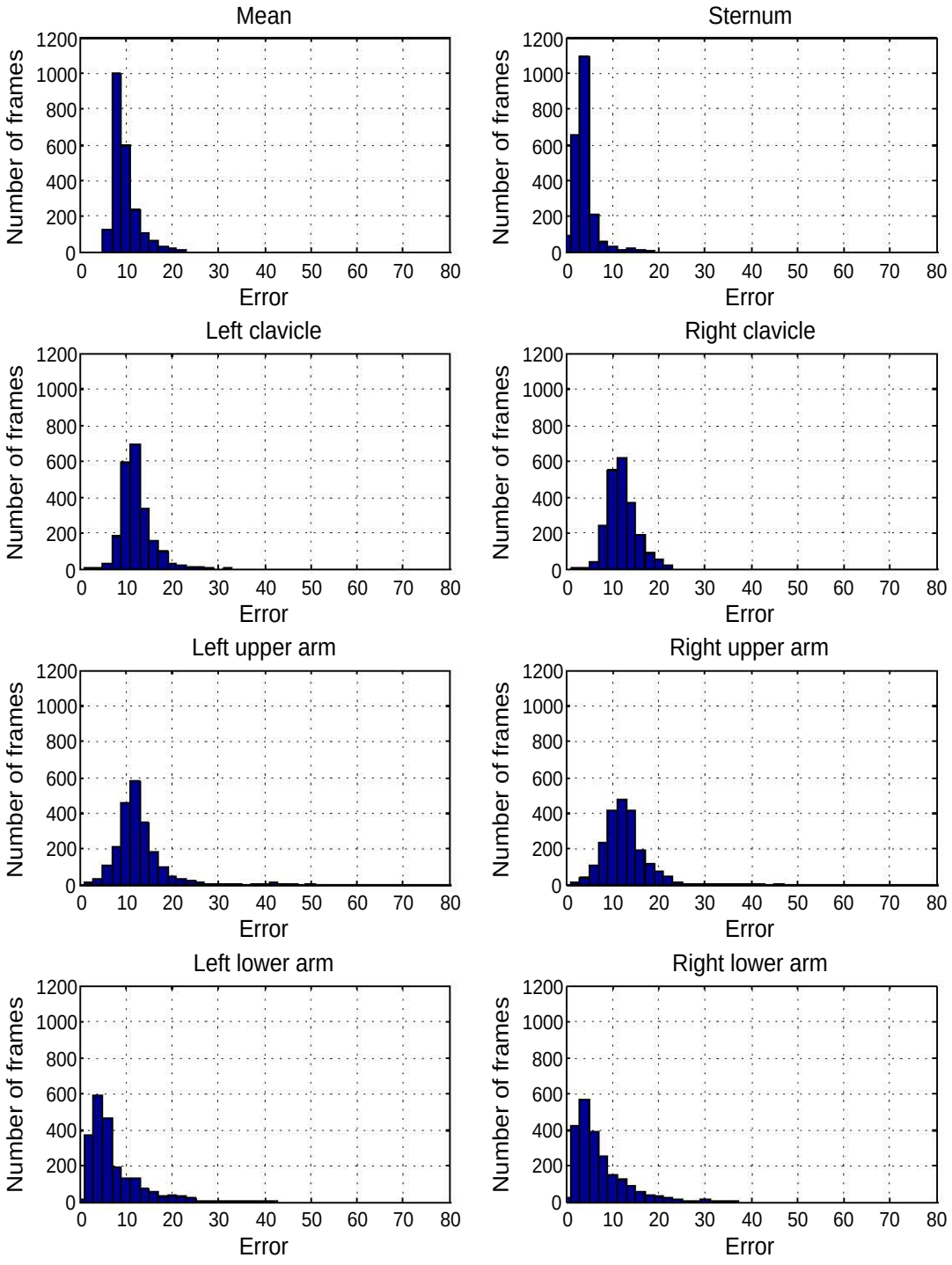


Figure 6.1: ARMAR Position error distribution.

Table 6.1: ARMAR Position error distribution description.

| DOF | Shape | Spread | Height | Mode |
|---|---|---|---|---|
| Mean | distinct right skew | low | very high | 8cm |
| Sternum | right skew | low | very high | 4cm |
| Glenohumerals | slight right skew | moderate | medium | 12cm |
| Elbows | almost symmetrical | moderate | low | 12cm |
| Wrists | distinct right skew | high | low | 4cm |

and high height of the mean distribution suggest that AMAR has few, or minor, additional limiting factors.

The waist joints of AMAR are able to position the sternum with good accuracy as shown by the high height, low spread and low modal value of the sternum position error distribution. The clavicles position error distributions have a lower height and higher spread than that of the sternum. This, combined with the large increase in the mode, from 4cm at the sternum to 12cm at the clavicles, shows that the waist joints, alone, are unable to position the clavicles with good accuracy.

The upper arm position error distributions have slightly lower height than the clavicle distributions, showing that the glenohumeral joints have some limitations in positioning the upper arms. There is a slight shift to the left in the shape of the upper arm distributions, making them more symmetrical than the clavicle distributions. This shows that the glenohumeral joints are able to compensate somewhat for some of the errors brought forward from the waist joints. There is a large decrease in the mode, from 12cm at the upper arms to 4cm at the lower arms. This shows that the glenohumeral joints and elbow joints are able to largely compensate for some of the errors brought forward from the waist joints, in order to position the lower arm with better accuracy.



### Peaks and troughs

***Torso.*** For ARMAR, the troughs in the sternum position error distribution occur when the waist flexion and lateral flexion joints are close to their neutral positions. (See figure 6.2.) The waist rotation joint remains near to its neutral position for all the peaks and troughs. The troughs in the clavicle position error distributions occur throughout the range of the waist lateral flexion joint and in the mid-range of the waist flexion joint. Peaks in the clavicle position error distributions occur

throughout the range of the waist flexion and lateral flexion joints. The two combined peaks in the sternum and left clavicle error distributions occur when the waist lateral flexion joint is at the limit of its motion range. For all remaining peaks that involve a peak in the sternum position error distribution, the waist flexion joint is at the limit of its extension motion range.

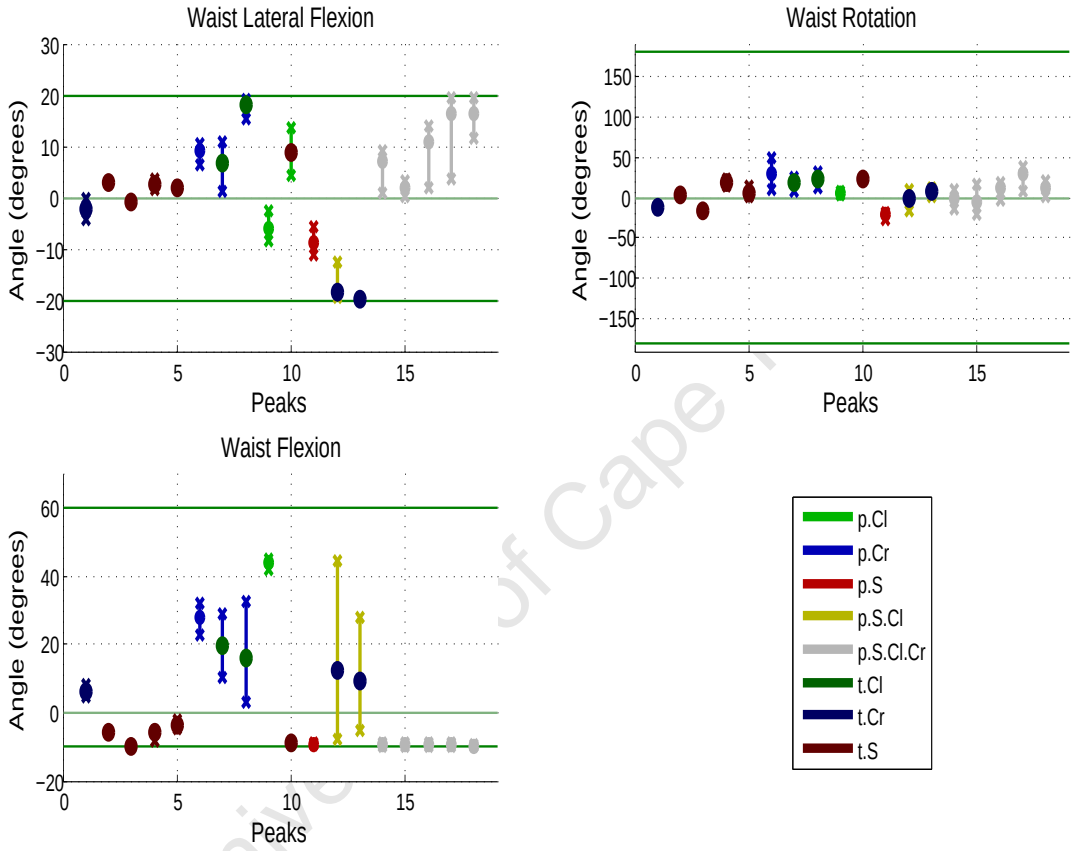


Figure 6.2: Range of torso joint motion for position error peaks and troughs, ARMAR. Key: • - mean joint angle, x - joint angle range, p - peak, t - trough, S - sternum, C - clavicle, l - left, r - right

Troughs in the sternum position error distribution occur when the desired torso posture is very close to upright as illustrated in figure 6.3b. The increase in error when the torso is bent, is mainly due to the influence of the position of the waist joints. The waist joints are located slightly above the hip line, thus as the torso is bent, the distance between the desired and the actual position of the sternum increases. Peaks in the sternum position error distributions are mainly due to the limited extension range of the waist flexion joint, as illustrated in figure 6.3c. The lateral flexion joint limit also influences the peaks in the sternum error.

The troughs in the clavicle position error distributions occur when no shoulder girdle motion is required to reach the desired position. I.e., when the desired clavicle position is close to $90^o$ to the spine as shown by the left clavicle in figure 6.3a. Peaks in the clavicle position error distribution occur when the desired clavicle position is at a large angle, above $90^o$, from spine as shown by the right clavicle in figure 6.3a. The lack of shoulder girdle joints thus prevents the clavicle from reaching the desired positions. The peaks in the sternum position error distribution also increase the peaks in the clavicle position error distributions as shown in figure 6.3c.

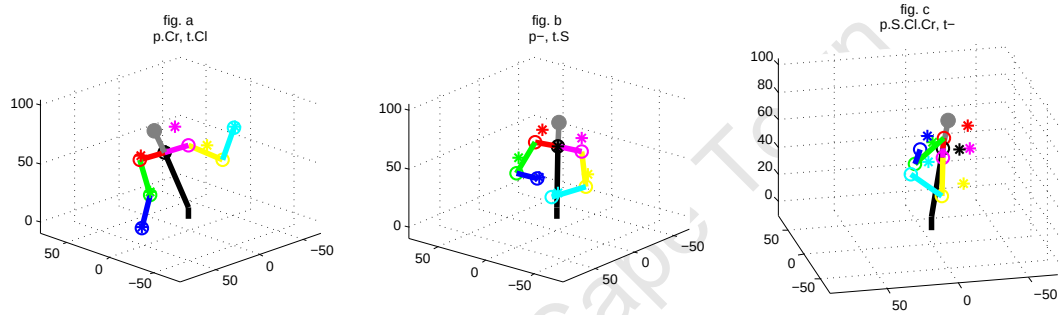


Figure 6.3: Dance configurations for torso, ARMAR. Key: $*$ - desired position, o - actual position, p - peak, t - trough, S - sternum, C - clavicle, l - left, r - right

***Arms.*** For AMAR's arms, combined troughs in the upper arm and lower arm position error distributions occur at about $100^o$ glenohumeral flexion, while the rest of the troughs in the lower arm position error distribution occur below this. (See figure 6.4.) Most troughs in the distributions occur close to the neutral positions of glenohumeral rotation and glenohumeral abduction joints. Most of the peaks in the distributions occur at the extension limit of the glenohumeral flexion joint. Some of the troughs in the lower arm position error distributions occur when the elbow joint is at its extension limit.

The errors in the clavicle positions largely influence the arm position errors. Troughs in the arm position error distributions occur when the glenohumeral and elbow joints are able to compensate for these errors as shown in figure 6.5a. Some peaks in the upper arm position error distribution occur when the glenohumeral and elbow joints are unable to compensate due to limited glenohumeral extension as shown in figure 6.5b. Where peaks in all three distributions, i.e. clavicle, upper arm and lower arm occur, this is due to the sternum position being far from its desired position as can be seen in figure 6.5b. In some cases, the glenohumeral

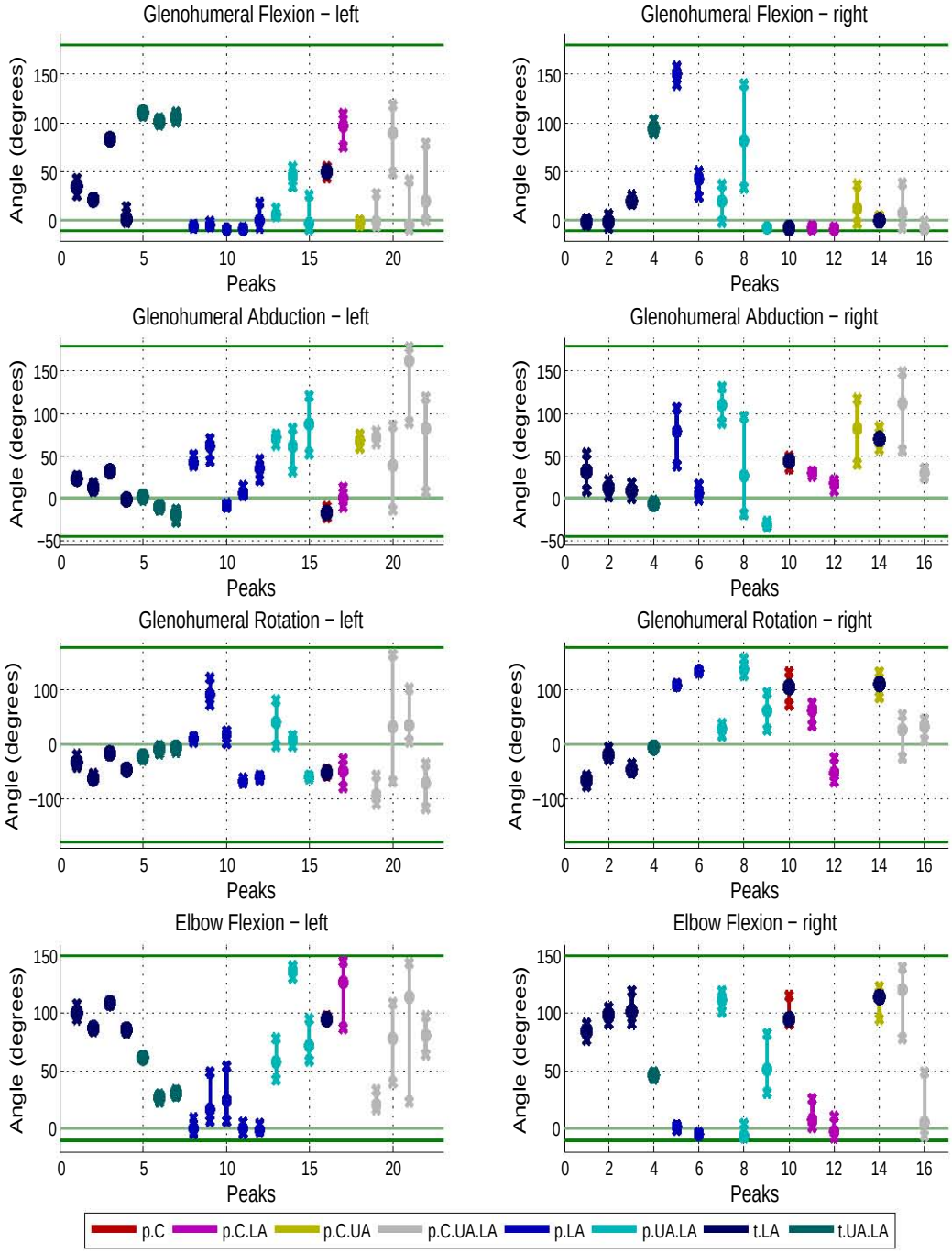


Figure 6.4: Range of arm joint motion for position error peaks and troughs, ARMAR. Key: • - mean joint angle, x - joint angle range, p - peak, t - trough, C - clavicle, UA - upper arm, LA - lower arm

joint singularity influences the error in the arms. While a better posture might be possible, it cannot be attained as the arm is stuck at the singular point as shown by the left arm of figure 6.5c. Correcting the singularity also takes a number of frames, thus the influence of the error is seen for a number of frames after the singularity has been passed.

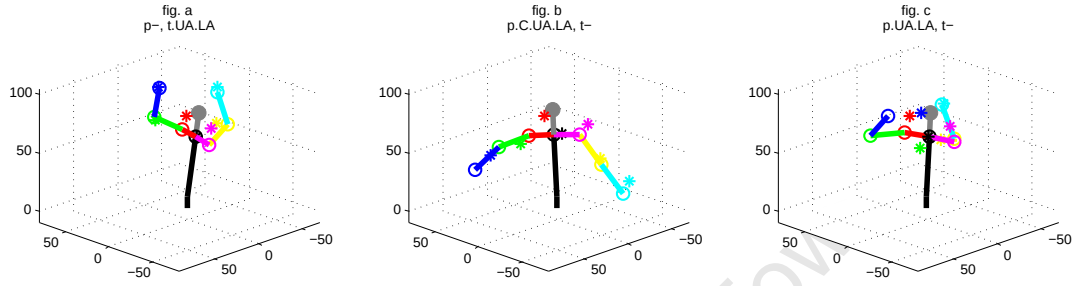


Figure 6.5: Dance configurations for arms, ARMAR. Key: $*$ - desired position, o - actual position, p - peak, t - trough, C - clavicle, UA - upper arm, LA - lower arm

### 6.1.2 HRP

HRP has moderate motion following abilities. It has limitations due to the lack of a shoulder girdle and the lack of a waist lateral flexion joint. The human motion imitation performance is discussed in detail below.

#### Error distribution

The position error distributions for HRP are shown in figure 6.6, and the description is shown in table 6.2. HRP has a mean error distribution with a distinct right skewed shape that has distinct limit to the left at about 6cm and a mode of 10cm. The position of the left limit indicates that HRP has at least one significant limiting factor in its overall positioning abilities. The low spread and high height of the mean distribution suggest that HRP has additional significant limiting factors.

The waist joints of HRP are able to position the sternum with moderate accuracy as shown by the moderate spread and moderate modal value of the sternum position error distribution. The waist joints do have some limitations, however as shown

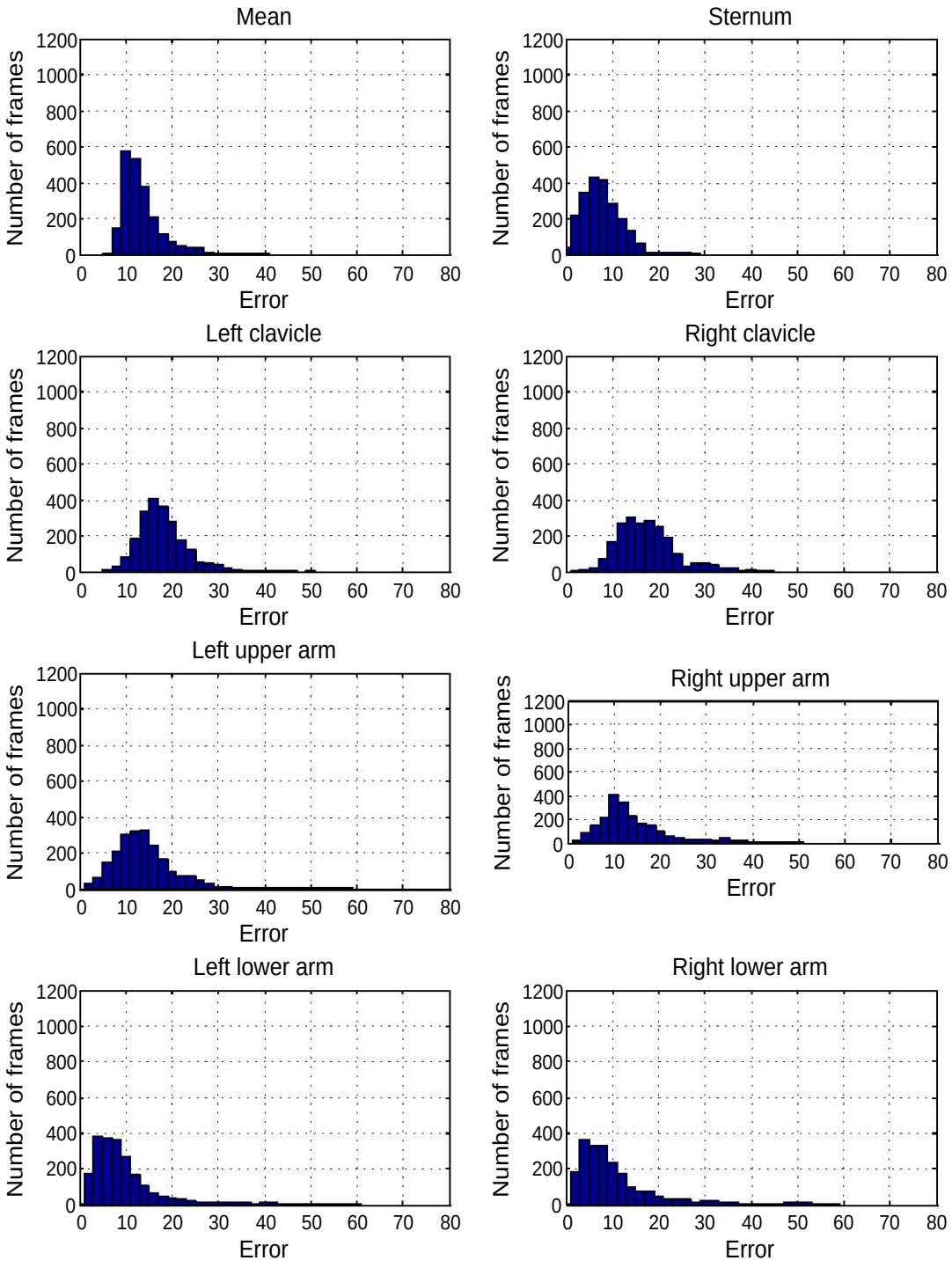


Figure 6.6: HRP Position error distribution.

Table 6.2: HRP Position error distribution description.

| DOF | Shape | Spread | Height | Mode |
|---|---|---|---|---|
| Mean | distinct right skew | low | medium | 10cm |
| Sternum | slight right skew | moderate | low | 6cm |
| Glenohumerals | almost symmetrical | very high | very low | 16cm |
| Elbows | slight right skew | very high | very low | 10cm and 12cm |
| Wrists | distinct right skew | very high | very low | 4cm to 8cm |

by the low peak of the sternum position error distribution. The clavicles position error distributions have a lower height and higher spread than that of the sternum. This, combined with the large increase in the mode, from 6cm at the sternum to 16cm at the clavicles, shows that the waist joints, alone, are unable to position the clavicles with a similar moderate accuracy of the sternum.

There is a shift to the left in the mode of the upper arm distributions, to 10cm and 12cm. This shows that the glenohumeral joints are able to compensate somewhat for some of the errors brought forward from the waist joints. There is a moderate decrease in the mode, from 8cm at the upper arms to 4cm at the lower arms. This shows that the glenohumeral joints and elbow joints are able to compensate further for some of the errors brought forward from the waist joints, in order to position the lower arm with better accuracy.



### Peaks and troughs

**Torso.** For HRP, the troughs in the sternum position error distribution occur when the waist flexion joint is close to its neutral position. (See figure 6.7.) The waist rotation joint limit is not reached for all the peaks and troughs. The clavicle position error distribution troughs occur in the mid-range of waist flexion joint. Peaks in the clavicle position error distributions occur throughout the range of the waist flexion joint. One sternum position error peak occurs at the waist flexion limit. For all remaining peaks that involve a sternum position error peak, the waist flexion joint is at its extension limit.

As with ARMAR, for HRP; troughs in the sternum position error distribution occur when the torso is at an upright posture; troughs in the clavicle position error distribution occur at angles close $90^o$ to the spine; peaks in the sternum position error distribution occur due to the limited extension range of the waist

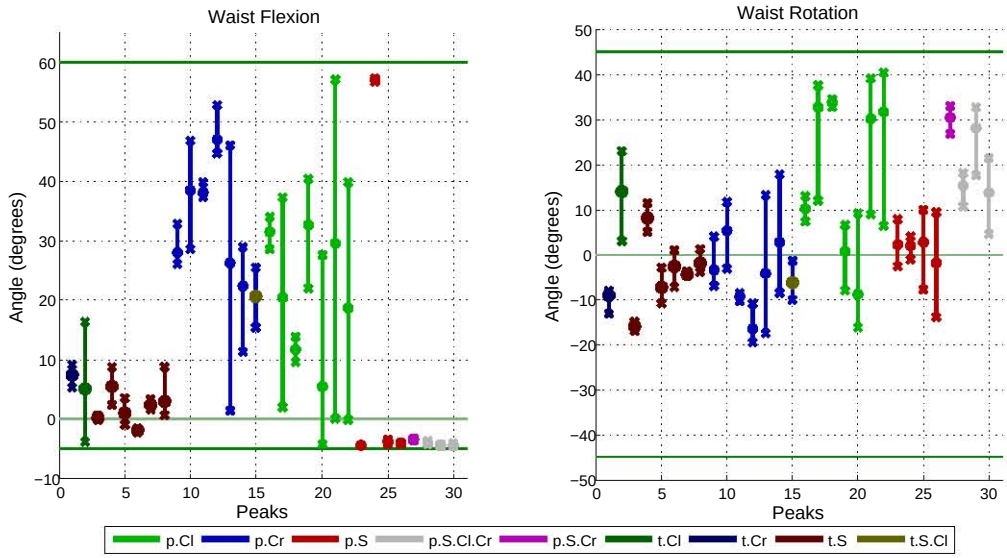


Figure 6.7: Range of torso joint motion for position error peaks and troughs, HRP. Key: • - mean joint angle, x - joint angle range, p - peak, t - trough, S - sternum, C - clavicle, l - left, r - right

flexion joint; peaks in the clavicle position error distributions occur due to a lack of a shoulder girdle (see figure 6.8b); peaks in the clavicle position error distributions are increased by the sternum error. Unlike ARMAR, HRP's sternum position error peaks also occur due to the lack of a waist lateral flexion joint as illustrated in figure 6.8b. In addition, the location of the waist joint, which is high above the hip-line, increases the sternum error. This is shown as the torso bends forwards in figure 6.8c.

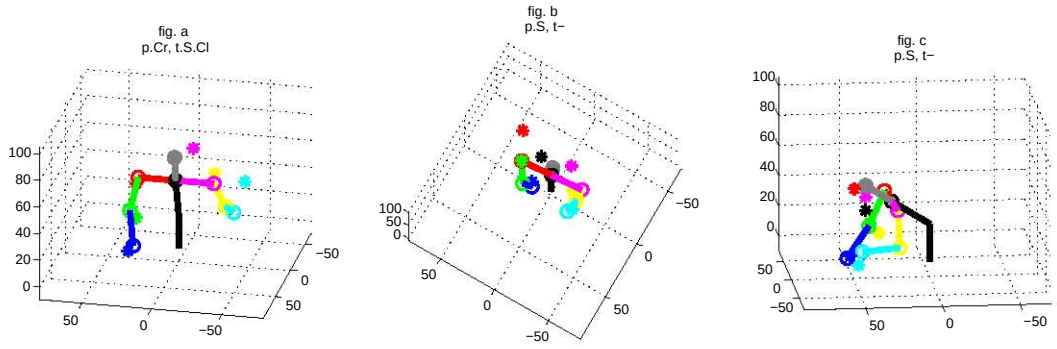


Figure 6.8: Dance configurations for torso, HRP. Key: ∗ - desired position, o - actual position, p - peak, t - trough, S - sternum, C - clavicle, l - left, r - right

**Arms.** For HRP's arms, troughs in the upper and lower arm position error distributions occur throughout the range of glenohumeral flexion, and up to about $50^o$ glenohumeral abduction. Some of the lower arm position error peaks occur at, or close to, the elbow flexion limit. (See figure 6.10).

As with ARMAR, for HRP as shown in figure 6.9; errors in the clavicles largely influence the arm errors; arm troughs occur due to compensation by the glenohumeral and elbow joints (see figure 6.9a); peaks in the arms occur when the limited glenohumeral extension is unable to provide compensation (see figure 6.9c); peaks in all three occur due to large sternum errors; the glenohumeral singularity causes some peaks (see figure 6.9b). In addition, HRP's limited abduction range also increases arm errors.

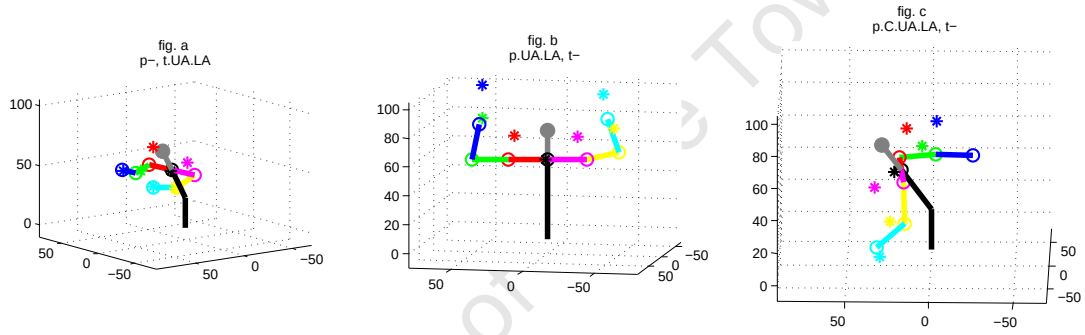


Figure 6.9: Dance configurations for arms, HRP. Key: $*$ - desired position, o - actual position, p - peak, t - trough, C - clavicle, UA - upper arm, LA - lower arm



### 6.1.3 SURALP

SURALP has poor motion following abilities due due to the lack of a shoulder girdle and lack of waist flexion and lateral flexion joints. The human motion imitation performance is discussed in detail below.

#### Error distribution

The position error distributions for SURALP are shown in figure 6.11, and the description is shown in table 6.3. SURALP has a mean position error distribution with a distinct right skewed shape that has a distinct limit to the left at about

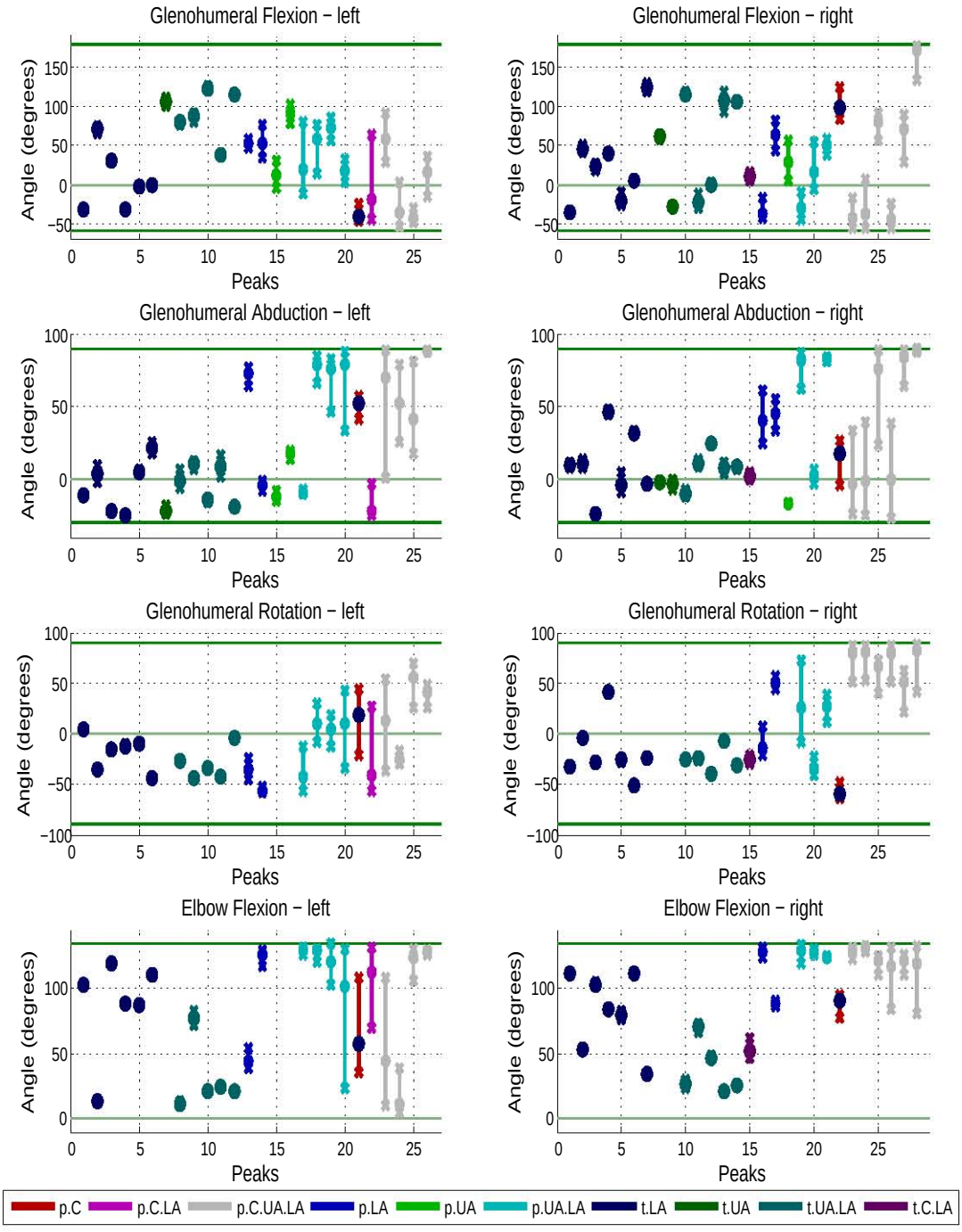


Figure 6.10: Range of arm joint motion for position error peaks and troughs, HRP. Key: • - mean joint angle, x - joint angle range, p - peak, t - trough, C - clavicle, UA - upper arm, LA - lower arm

8cm, and a mode of 12cm. The position of the left limit indicates that SURALP has at least one significant limiting factor in its overall positioning abilities. The very low height and high spread of the distribution suggest that SURALP has a large number of additional significant limiting factors.

Table 6.3: SURALP Position error distribution description.

| DOF | Shape | Spread | Height | Mode |
|---|---|---|---|---|
| Mean | distinct right skew | high | very low | 12cm |
| Sternum | slight right skew | very high | extremely low | 6cm |
| Glenohumerals | slight right skew | very high | very to extremely low | 12cm and 14cm to 16cm |
| Elbows | slight right skew | very high | very low | 12cm and 14cm |
| Wrists | right skew | very high | very low | 10cm and 12cm |

The waist joints of SURALP are able to position the sternum with low accuracy as shown by the very high spread, flat shape and very low height of the sternum position error distribution. There is a shift to the right in the clavicle position error distributions, compared to the sternum distributions. This, as well as the very low height and very high spread of the clavicle position error distributions, shows that the waist joints alone are only able to position the glenohumerals with very low accuracy.

There is a shift to the right in the shape of the upper arm distributions and the slight increase in the height. This show that the glenohumeral joints are able to compensate somewhat for some of the errors brought forward from the waist joints. There is a decrease in the mode of the lower arms to 10cm and 12cm. This show that the glenohumeral joints and elbow joints are able to compensate further for the errors brought forward from the waist joints.



### Peaks and troughs

**Torso.** For SURALP, peaks and troughs in the position error distributions occur throughout the waist rotation motion range. The waist rotation joint limit is not reached for all the peaks and troughs. (See figure 6.12).

As with ARMAR and HRP, for SURALP; sternum position error troughs occur at an upright posture as shown in figure 6.13a; clavicle troughs occur at angles close $90^o$ to the spine as seen by the right clavicle in figure 6.13a; peaks in the clavicle position errors occur due to a lack of shoulder girdle; peaks in the clavicles

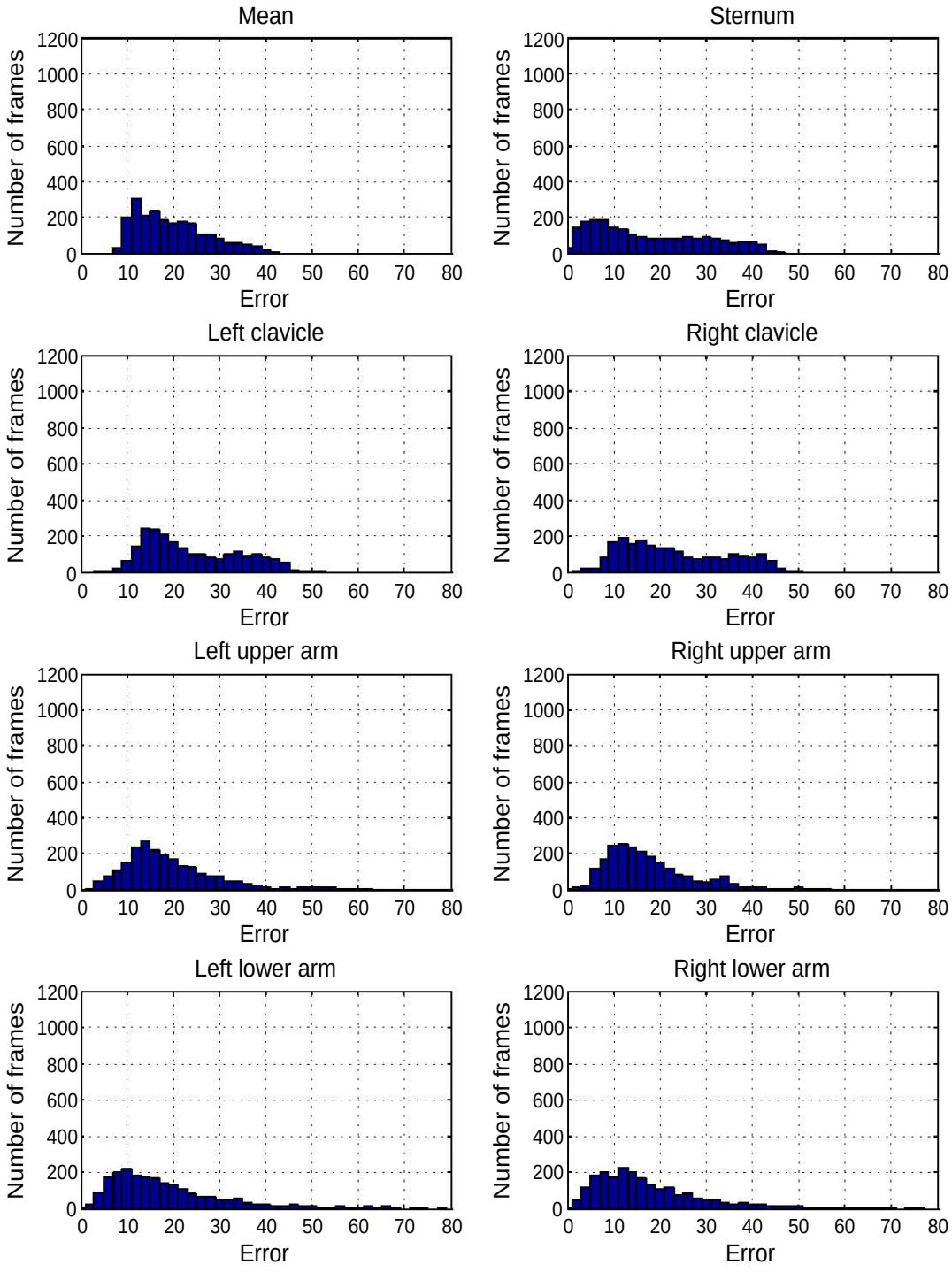


Figure 6.11: SURALP Position error distribution.

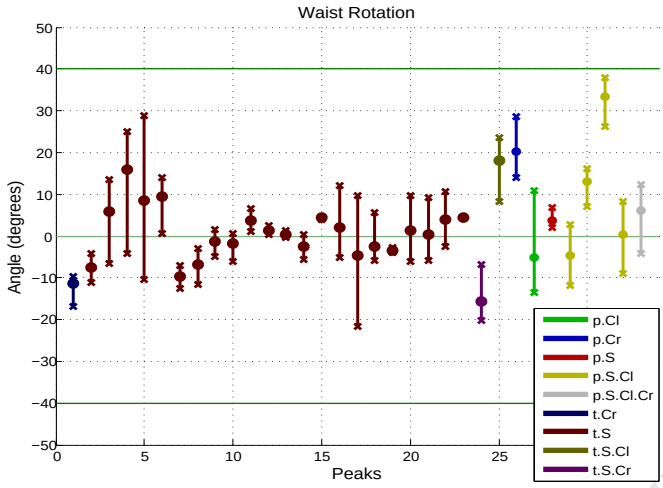


Figure 6.12: Range of torso joint motion for position error peaks and troughs, SURALP. Key: • - mean joint angle, x - joint angle range, p - peak, t - trough, S - sternum, C - clavicle, l - left, r - right

are increased by the sternum error. Like HRP, SURALP's sternum peaks also occur due to the lack of a waist lateral flexion joint as illustrated in figure 6.13b. In addition, the lack of a waist flexion joint greatly increases the errors in the sternum position as seen in in figure 6.13b and c.

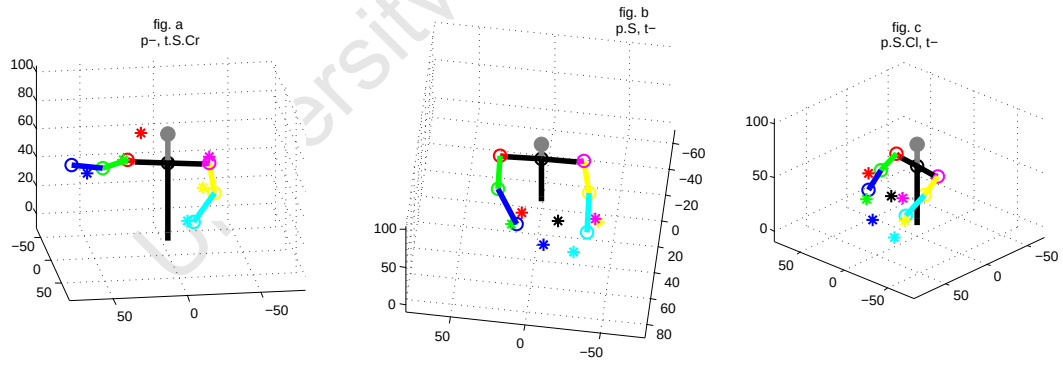


Figure 6.13: Dance configurations for torso, SURALP. Key: ∗ - desired position, o - actual position, p - peak, t - trough, S - sternum, C - clavicle, l - left, r - right

**Arms.** Troughs in the position error distributions occur when the glenohumeral joints are close to the neutral and mid-range of their motion. Some of the peaks in the position errors occur at the glenohumeral flexion, abduction and elbow flexion motion limits. No peaks and troughs in the lower arm position error distributions occur in the hyperextension range of the elbow joints. (See figure 6.14).

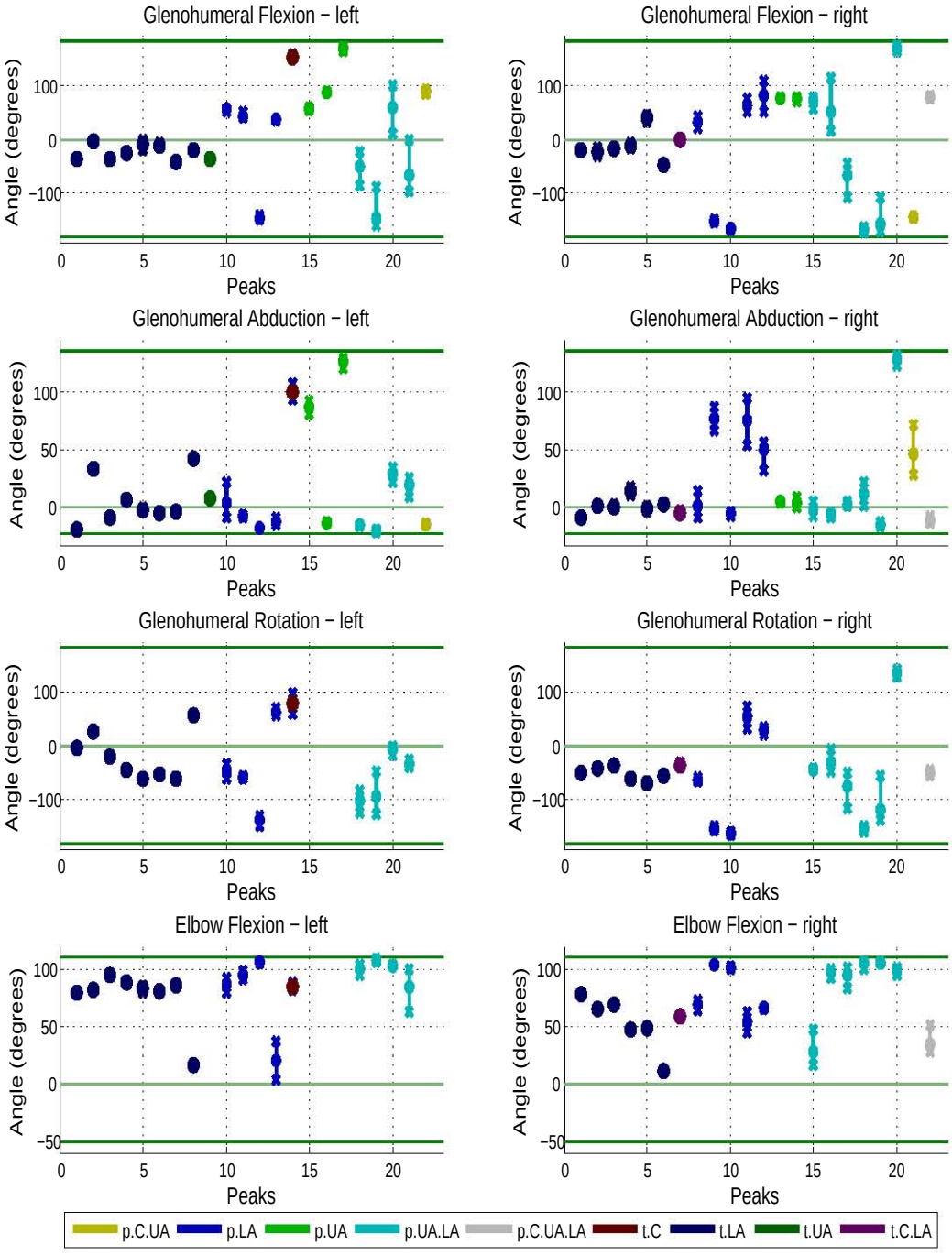


Figure 6.14: Range of arm joint motion for position error peaks and troughs, SURALP. Key: • - mean joint angle, x - joint angle range, p - peak, t - trough, C - clavicle, UA - upper arm, LA - lower arm

As with ARMAR and HRP, for SURALP, as shown in figure 6.15; errors in the clavicles largely influence the arm errors; arm position error troughs occur due to compensation by the glenohumeral and elbow joints as seen in figure 6.15a; peaks in the arm position errors occur when the limited glenohumeral extension and adduction are unable to provide compensation; peaks in all three error distribution, i.e clavicle, upper and lower arm, occur due to large sternum errors as seen in figure 6.15c; the glenohumeral joint singularity causes some peaks as shown in figure 6.15b. The elbow flexion limit also affects the arm errors.

As SURALP has some very large errors, despite the small time step, the distance between the posture attained at one time instant from the posture required at the next time instant, is very large. The numerical integration used for motion transfer is valid for small time steps and small distances. Thus even while better postures are possible at the next time step, they are not reached and the resulting posture is sometimes very different from the required posture as shown in figure 6.15b. This takes a number of frames to correct.

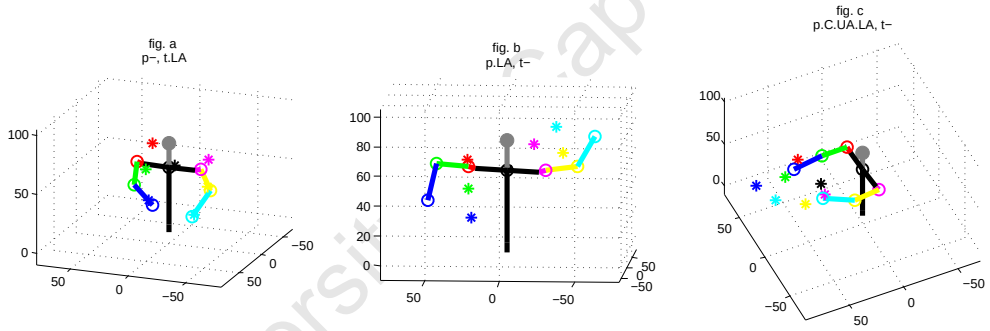


Figure 6.15: Dance configurations for arms, SURALP. Key: $*$ - desired position, o - actual position, p - peak, t - trough, C - clavicle, UA - upper arm, LA - lower arm

### 6.1.4 WABIAN

WABIAN has very good motion following abilities due to its high waist motion and high arm motion. It has limitations due to the lack of a shoulder girdle. The human motion imitation performance is discussed in detail below.

### Error distribution

The position error distributions for WABIAN are shown in figure 6.16, and the description is shown in table 6.4. WABIAN has a mean position error distribution with a distinct right skewed shape, a distinct limit to the left at about 6cm, a mode of 6cm. The position of the left limit indicates that WABIAN has at least one significant limiting factors in its overall positioning abilities. The very high height and very low spread of the distribution suggest that WABIAN has very few, or very minor, additional limiting factors.

Table 6.4: WABIAN Position error distribution description.

| DOF | Shape | Spread | Height | Mode |
|---|---|---|---|---|
| Mean | distinct right skew | very low | very high | 6cm |
| Sternum | slight right skew | very low | very high | 4cm |
| Glenohumerals | almost symmetrical | low | medium | 8cm |
| Elbows | slight right skew | moderate | medium | 8cm |
| Wrists | distinct right skew | moderate | medium to high | 2cm |

The waist joints of WABIAN are able to position the sternum with very good accuracy as shown by the very low spread, very high height and low modal value of the sternum position error distribution. There is an increase in the mode of the distributions from 4cm at the sternum to 8cm at the clavicles, as well as a lower height and higher spread of the clavicle position error distributions. This show that the waist joints alone are only able to position the clavicles with moderate accuracy.

The slight shift to the right of the upper arm distributions and the slightly higher height, show that the glenohumeral joints are able to compensate a little for some of the errors brought forward from the waist joints. The decrease in the mode to 2cm at the lower arms shows that the glenohumeral joints and elbow joints are able to largely compensate for the errors brought forward from the waist joints.

### Peaks and troughs

**Torso.** For WABIAN, the troughs in the sternum position error distributions occur when the waist flexion and lateral flexion joints are at neutral to mid-range of their joint motion. (See figure 6.17.) The waist rotation joint remains near to its

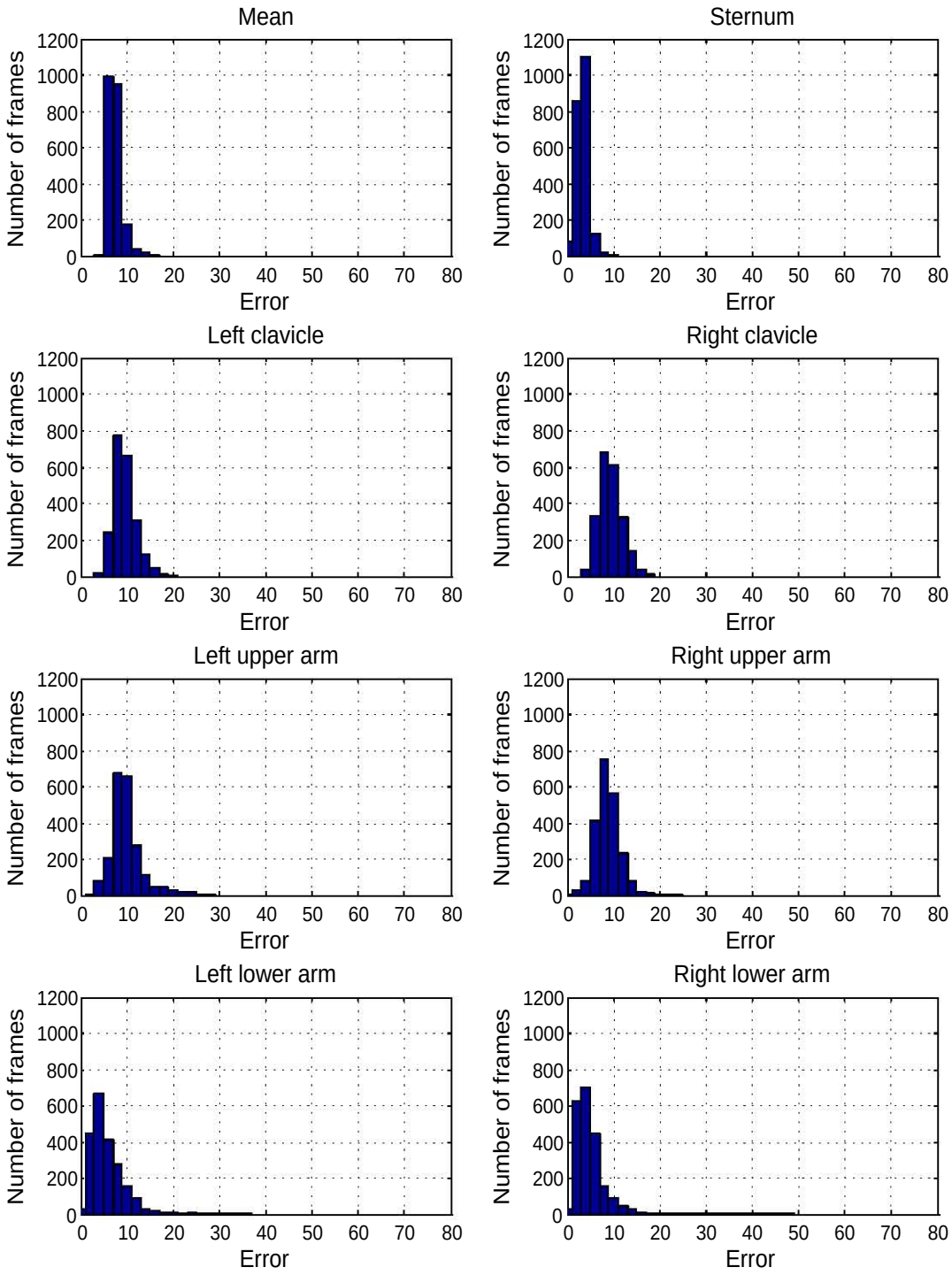


Figure 6.16: WABIAN Position error distribution.

neutral position for all the peaks and troughs. The clavicle position error troughs occur throughout the range of the waist lateral flexion and waist flexion joints. Peaks in the clavicle position errors occur throughout the range of the two joints. The two combined sternum and left clavicle position error peaks occur at the extension limit of the waist flexion joint. The two combined sternum and clavicle position error peaks do not occur at the limits of any joint. For all remaining position error peaks that involve a peak in the sternum position error distribution, the waist flexion joint is at its flexion limit.

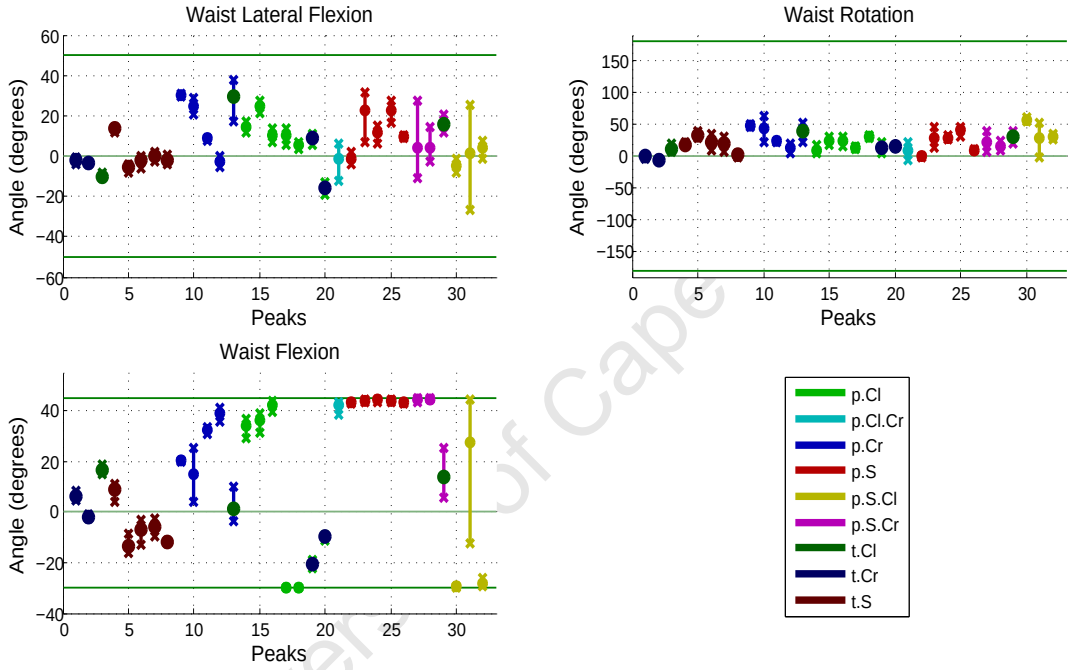


Figure 6.17: Range of torso joint motion for position error peaks and troughs, WABIAN. Key: • - mean joint angle, x - joint angle range, p - peak, t - trough, S - sternum, C - clavicle, l - left, r - right

As with ARMAR, HRP and SURALP, for WABIAN; sternum troughs occur at when the torso close to an upright posture as shown in figure 6.18c; clavicle troughs occur at angles close $90^o$ to the spine as seen by the right clavicle in figure 6.18b; peaks in the clavicles occur due to a lack of shoulder girdle; peaks in the clavicles are increased by the sternum error. Like HRP, WABIAN's sternum peaks also occur due to the position of the waist joints above the hip-line as seen when the torso bends forwards in figure 6.18a. WABIAN's sternum peaks are however, affected more by its limited waist flexion range than waist extension as WABIAN has a high waist extension range. Some sternum peaks occur due to compensating for the lack of a shoulder girdle. As seen in figure 6.18b, the desired sternum

position is within the lateral flexion limit of the waist, however the actual sternum position is offset to try reach the clavicles.

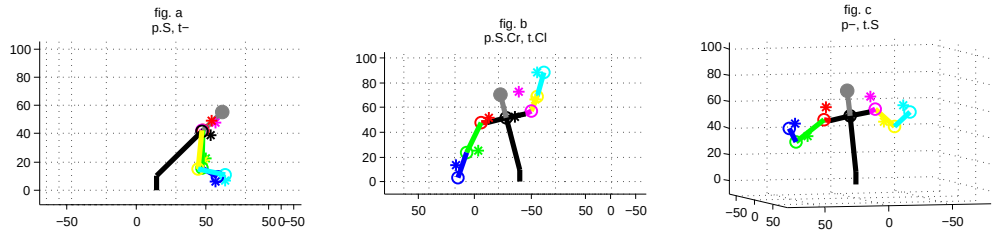


Figure 6.18: Dance configurations for torso, WABIAN. Key: $*$ - desired position, o - actual position, p - peak, t - trough, S - sternum, C - clavicle, l - left, r - right

**Arms.** Troughs in the position error distributions occur throughout the motion range of each joint. No troughs occur close to $90^o$ abduction. Most of the individual upper arm position error peaks occur at the glenohumeral flexion limit. (See figure 6.20).

As with ARMAR, HRP and SURALP, for WABIAN, as shown in figure 6.19; errors in the clavicles largely influence the arm errors; arm position error troughs occur due to compensation by the glenohumeral and elbow joints as shown in figure 6.19a; peaks in all three distributions occur due to large sternum errors; the glenohumeral singularity causes some position error peaks.

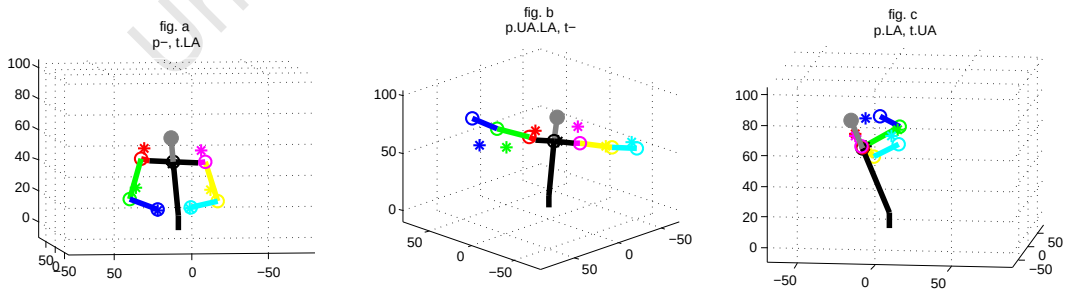


Figure 6.19: Dance configurations for arms, WABIAN. Key: $*$ - desired position, o - actual position, p - peak, t - trough, C - clavicle, UA - upper arm, LA - lower arm

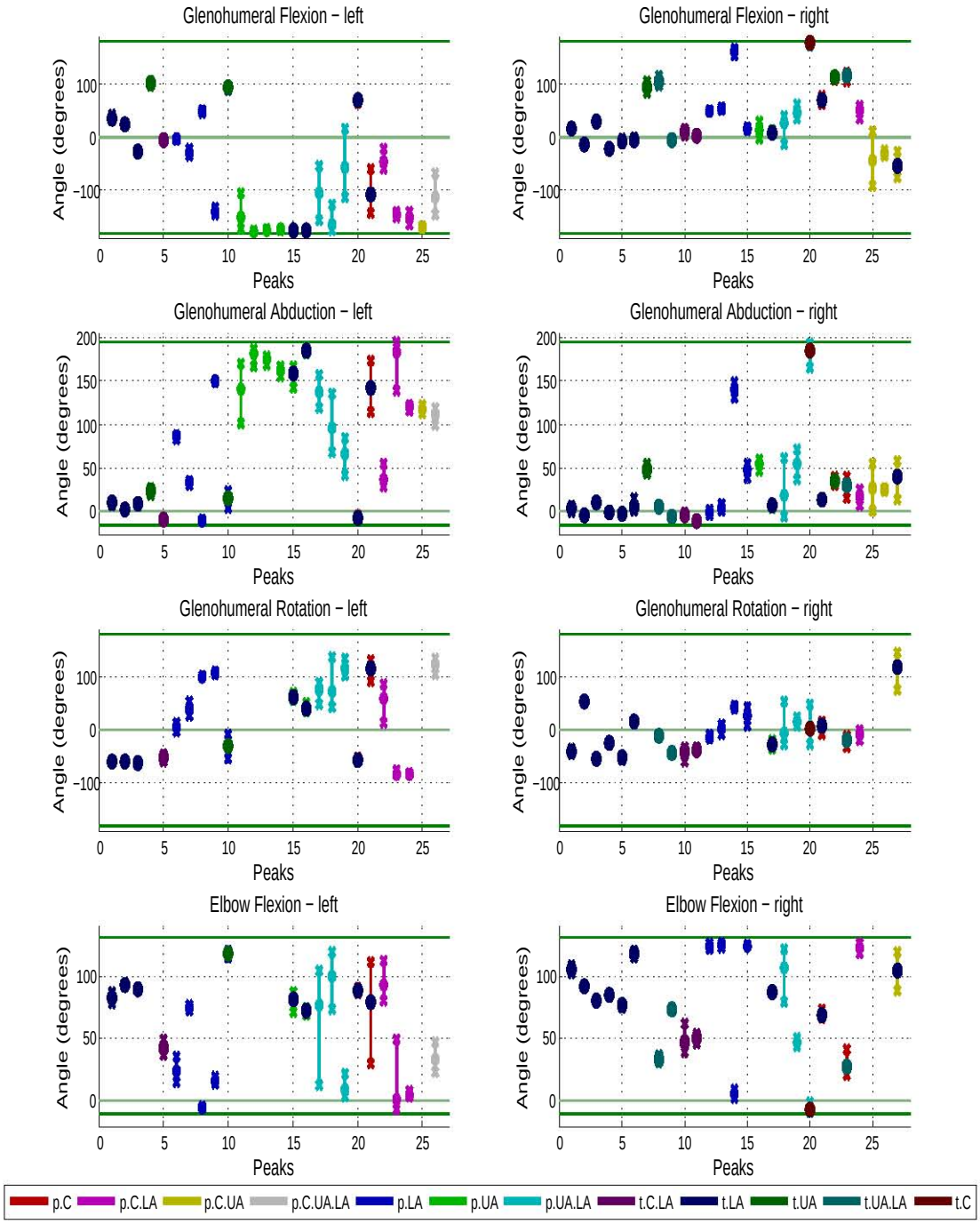


Figure 6.20: Range of arm joint motion for position error peaks and troughs, WABIAN. Key: • - mean joint angle, x - joint angle range, p - peak, t - trough, C - clavicle, UA - upper arm, LA - lower arm

In addition, WABIAN's limited glenohumeral adduction range also increases arm errors. WABIAN's arm motion gets stuck at the very high glenohumeral extension limit even though posture can be attained within a lower range as shown by the left arm in figure 6.19b. The elbow flexion limit also affects the arm errors as seen in figure 6.19c.

### 6.1.5 WE-4RII

WE4RII has very good motion following abilities due to its shoulder girdle motion, waist motion and high arm motion. It has limitations due to the lack of a waist lateral flexion joint. The human motion imitation performance is discussed in detail below.



#### Error distribution

The position error distributions for WE4RII are shown in figure 6.21, and the description is shown in table 6.5. WE4RII mean position error distribution has a very high height, very low spread and low mode of 4cm, showing that it has few or minor limiting factors in its overall positioning abilities.

Table 6.5: WE4RII Position error distribution description.

| DOF | Shape | Spread | Height | Mode |
|---|---|---|---|---|
| Mean | distinct right skew | very low | very high | 4cm |
| Sternum | right skew | low | medium | 4cm |
| Glenohumerals | right skew | low | medium | 4cm |
| Elbows | right skew | low | medium | 4cm |
| Wrists | distinct right skew | very low | high | 2cm |

The waist joints of WE4RII are able to position the sternum with moderate to good accuracy as shown by the low spread, medium height and low modal value of 4cm of the sternum position error distribution. The similar clavicle position error distributions show that the waist joints and the shoulder girdle joints combine to position the clavicles with moderate to good accuracy. There are however, some slight limitations in both the waist and shoulder girdle joints as shown by the medium heights.

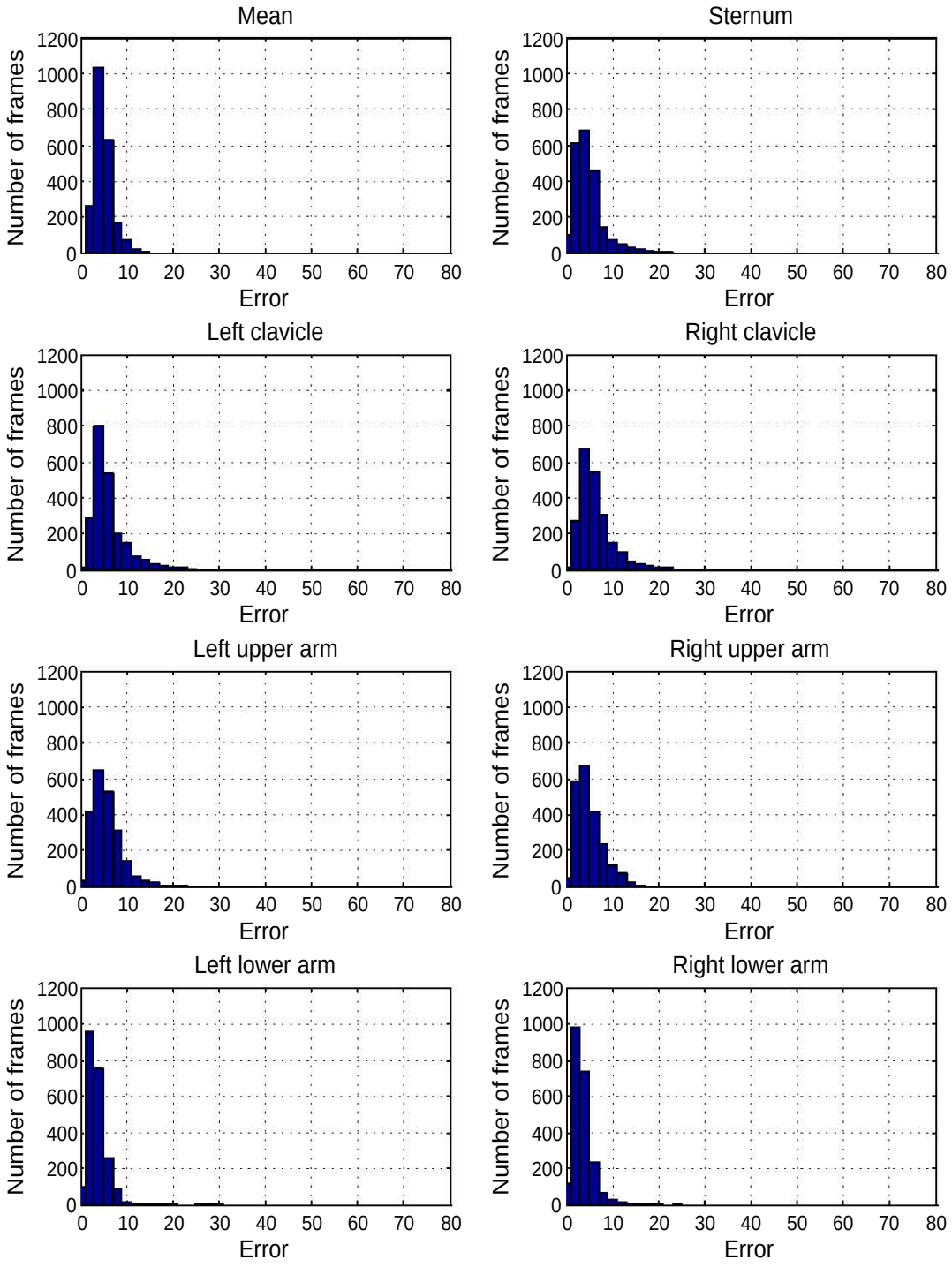


Figure 6.21: WE4RII Position error distribution.

The glenohumeral joints, likewise, are able to position the upper arms well. The decrease in the mode to 2cm at the lower arms and the increase in the height shows that the glenohumeral joints and elbow joints are able to compensate for the errors brought forward from the waist and shoulder girdle joints.

### Peaks and troughs

**Torso.** For WE4RII, the sternum position error troughs occur close to the neutral and mid-range of the waist flexion joint motion. All peaks and troughs in the distributions occur throughout the range of the waist rotation joint. However, the rotation limit is only approached a couple of times. The clavicle position error peaks and troughs occur throughout the range of shoulder girdle protraction and elevation. Some of the sternum position error peaks occur at the extension limit of the waist flexion joint. (See figure 6.23 and 6.22.)

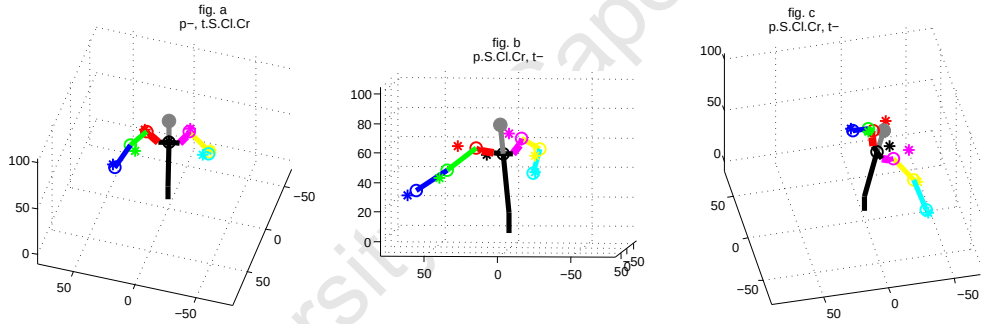


Figure 6.22: Dance configurations for torso, WE4RII. Key: ∗ - desired position, o - actual position, p - peak, t - trough, S - sternum, C - clavicle, l - left, r - right

As with ARMAR, HRP, SURALP, and WABIAN, for WE4RII; sternum position error troughs occur when the torso is close to an upright posture as shown in figure 6.22a; peaks in the clavicle position error distributions are increased by the sternum error. As with HRP, sternum position error peaks occur due to the lack of a waist lateral flexion joint as seen in figure 6.22b, and similar to AMAR and SURALP, due to limited waist extension as shown by figure 6.22c.

Like HRP and WABIAN, WE4RII's sternum peaks also occur due to the position of the waist joints above the hip-line. Unlike the other humanoids, WE4RII's clavicle troughs occur due to the presence of a shoulder girdle as seen in figure 6.22a. Peaks in the clavicle position errors occur due to the position of the shoulder girdle joints,

which are offset from the sternum. High shoulder girdle motions thus have a larger position error. The clavicle errors are also increased by the sternum errors.

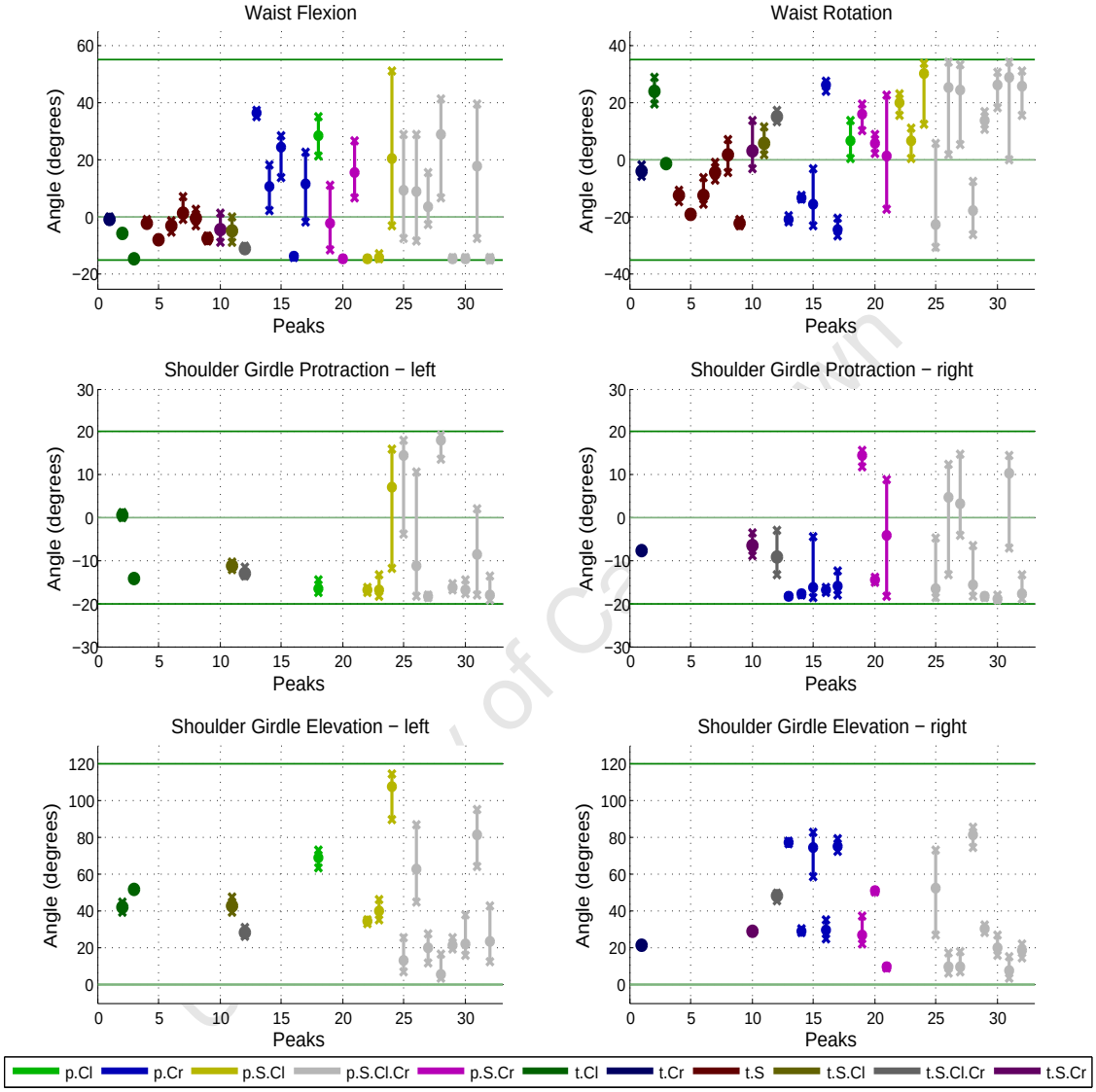


Figure 6.23: Range of torso joint motion for position error peaks and troughs, WE4RII. Key: • - mean joint angle, x - joint angle range, p - peak, t - trough, S - sternum, C - clavicle, l - left, r - right

**Arms.** Peaks and troughs for WE4RII arm position error distributions occur near the neutral and mid-range of the glenohumeral flexion joint. Most of the peaks and troughs in the distributions occur at the glenohumeral abduction limit. (See figure 6.24.)

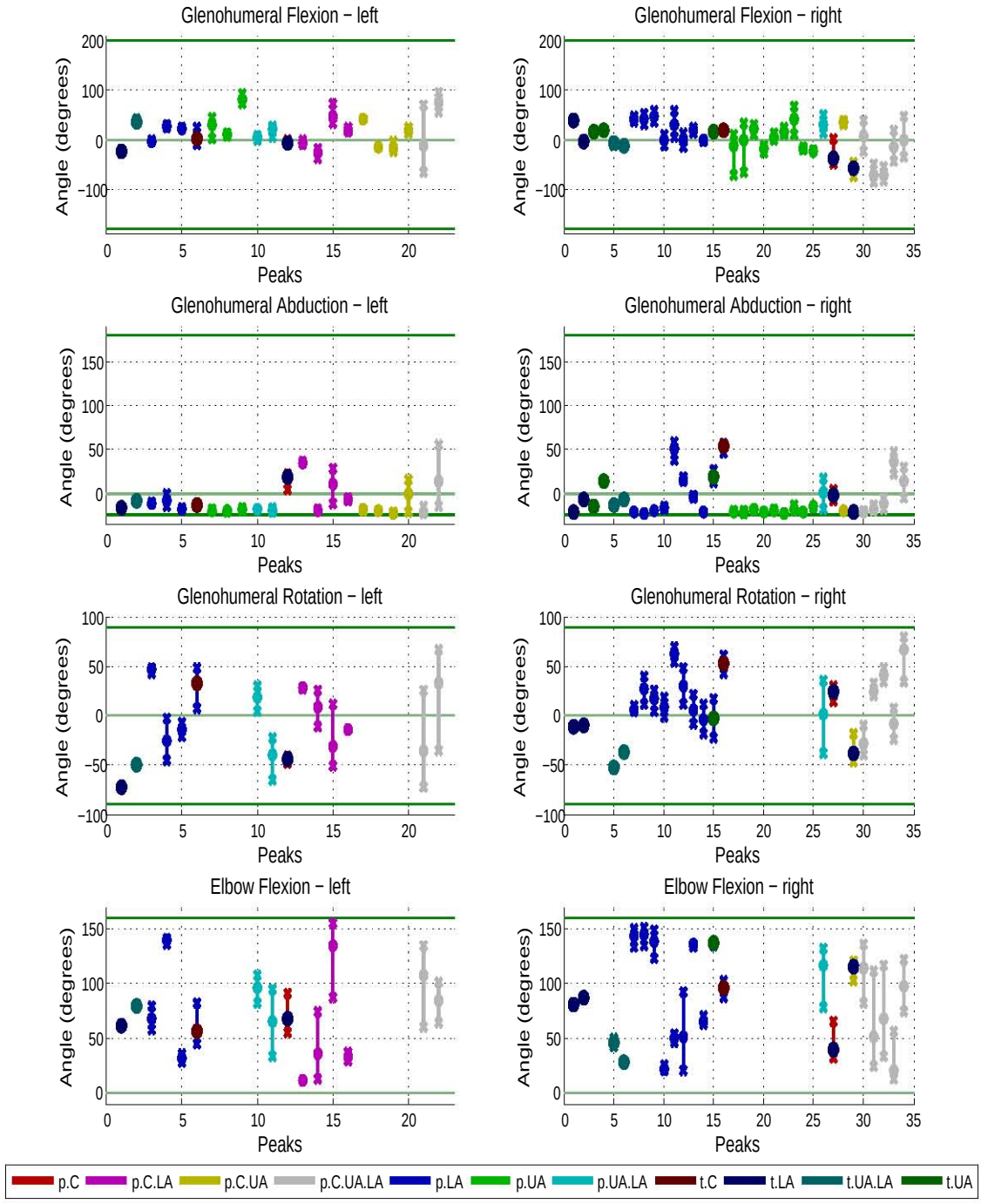


Figure 6.24: Range of arm joint motion for position error peaks and troughs, WE4RII. Key: • - mean joint angle, x - joint angle range, p - peak, t - trough, C - clavicle, UA - upper arm, LA - lower arm

As with the other humanoids, as shown in figure 6.25, for WE4RII; errors in the clavicles and sternum influence the arm errors. For WE4RII most arm position error peaks are due to the limited glenohumeral adduction.

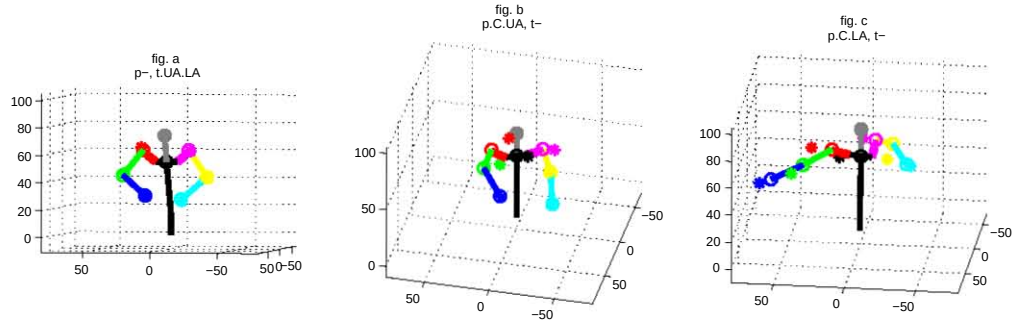


Figure 6.25: Dance configurations for arms, WE4RII. Key: $*$ - desired position, o - actual position, p - peak, t - trough, C - clavicle, UA - upper arm, LA - lower arm

## 6.2 Comparison of humanoids motion

The motion of the humanoid robot human motion imitation compared, first without added self collision avoidance, and secondly with self collision avoidance added. The mean and standard deviation of the position errors are compared as well as the range of joint motion used throughout the dance.

### 6.2.1 Without self collision avoidance

Figure 6.26 shows the position error bar plots of the position of the glenohumeral joints and sternum for each humanoid. The bars show the mean and standard deviations of the position errors.

While both WE4RII and HRP have two DOF waists with similar ranges of motion, WE4RII has a lower sternum position error due to the different locations of the sternum joints. WE4RII has waist joints that are located closer to the hip line while HRP has waist joints that are at the middle of the spine. Both ARMAR and WABIAN have three DOF waists. WABIAN has a lower error and standard deviation due to its higher waist extension range. WE4RII has a similar mean to

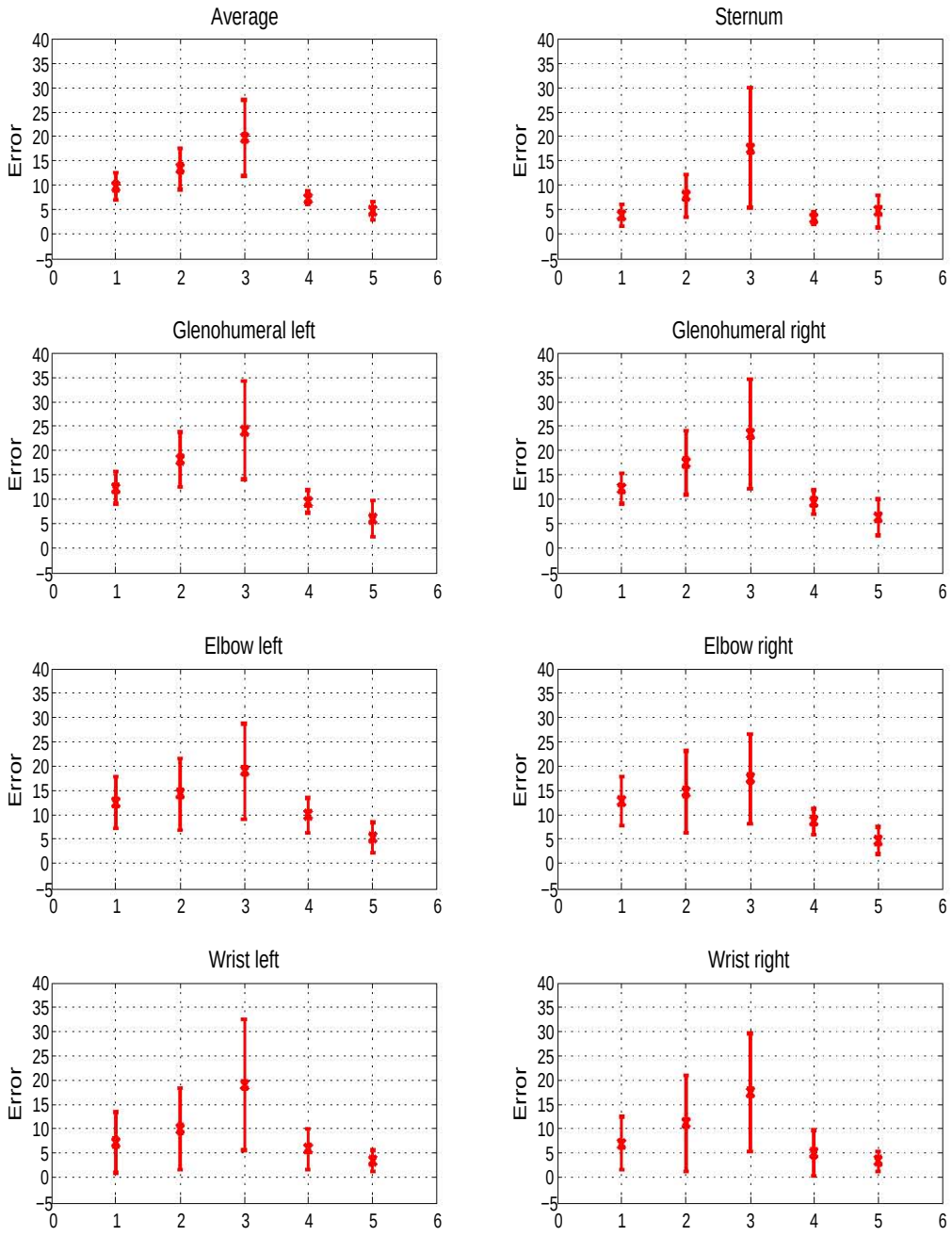


Figure 6.26: Position error mean and standard deviation bars. Key: x - mean, - - standard deviation. 1 - ARMAR, 2 - HRP, 3 - SURALP, 4 - WABIAN, 5 - WE4RII.

ARMAR but has a higher standard deviation. While WE4RII has no waist lateral flexion joint, WE4RII has slightly higher waist extension range than AMAR, which lowers its error. However the lack of the waist lateral flexion joint increases the standard deviation relative to that of ARMAR. Both ARMAR and WABIAN have low errors and standard deviations due to the presence of waist lateral flexion. SURALP has the largest error and standard deviation due to having only a single waist rotation range. The difference in error due to a second waist joint is much larger than the difference in error due to a third waist joint.

For the robot's with no shoulder girdle, the sternum error highly influences the clavicle error. The clavicles for these robots all have a higher mean and standard deviation than the sternum. WE4RII with its two DOF shoulder girdle joints has a decrease in the clavicle error as compared to the sternum error. The clavicle error for WE4RII has a lower mean than WABIAN due to the presence of the shoulder girdle, in contrast to the sternum which had a higher mean than WABIAN's. The location of the shoulder girdle joints of WE4RII are not at the sternum and the error caused, along with the sternum error carried over, is reflected in the standard deviation of the clavicles.

The upper arm error for WABIAN, ARMAR and SURALP is lower than that of the clavicles due to the compensating effect of the glenohumeral joints. ARMAR has a higher error than WABIAN, mainly due to the influence of the sternum error and in part due to the limited glenohumeral extension range of ARMAR. HRP has a slightly higher error and higher standard deviation, again due mainly to the influence of the sternum error. The differences in the mean upper arm errors of the humanoids is smaller than that of the clavicles, due to the glenohumeral joint action. WE4RII once again has the lowest error due to the influence of the shoulder girdle. The upper arm error of WE4RII however does not show a similar decrease as the other robot's from the clavicle error due the the limited glenohumeral adduction of WE4RII. HRP's upper arm mean error does not lower due to its limited abduction range.

Expect for SURALP, the lower arm errors are lower than the upper arm errors, due to the compensating effect of the glenohumeral and elbow joints. The standard deviations increase due to to an accumulation of errors of the preceding torso and arm segments, with the exception of WE4RII. The presence of a shoulder girdle lessens the error accumulation for WE4RII.

WE4RII has the lowest average error mean due to the presence of a shoulder girdle. The standard deviation of WE4RII is higher than WABIAN, due to the lack of a

waist lateral flexion joint and to limited glenohumeral adduction. WABIAN has the second smallest average error mean due to its three DOF waist and high waist joint range. ARMAR is third, again due to the waist joints. HRP is second, and SURALP with only one waist DOF has the highest error.

### Joint motion range used

The range of motion for each humanoid along with the actual range used through the dance are shown in figure 6.27 and 6.28.

For the dance, each robot uses most of, or all of, its waist flexion range. Waist extension is likewise fully used. Waist extension of all the humanoids except WABIAN is much less than that of an average human. From the previous analysis, the waist extension limit largely increases the errors in the sternum position. Limited waist flexion also increases errors as shown by WABIN. ARMAR has a lower waist lateral flexion range than WABIAN and uses its full range. WABIAN though having a large waist lateral flexion range, uses a range close to that of an average human. Both ARMAR and WABIAN have very high waist rotation ranges. They both use a range slightly larger than that of a human. The larger range is used to compensate for the lack of a shoulder girdle in positioning the clavicles.

The shoulder girdle protraction for WE4RII is equal to human protraction and the full range is used. Shoulder girdle elevation is much larger than that of an average human, and a very large range is used. The large range is used mainly due to the location of the shoulder girdle joints. The joints are not centered at the sternum and so a larger joint range is needed to reach the same position.

While WABIAN uses most of its very large glenohumeral flexion and extension range, this is not strictly necessary as the same postures can be attained using a combination of lower joint angles. The large range of extension is actually detrimental as the arm gets stuck at the extension limit even when the posture is feasible at lower angles. SURALP also uses most of its very large range and also gets stuck at the extension limit. WE4RII while also having a very large range of glenohumeral flexion and extension, uses only a fraction of the range. High arm positions are reached with the aid of the shoulder girdle motion thus high flexions and extensions are not used. WE4RII thus avoids approaching and getting stuck at the glenohumeral joint limits. WE4RII's arm and shoulder girdle action is in line with the working of the human upper limb's scapulohumeral rhythm. That is,

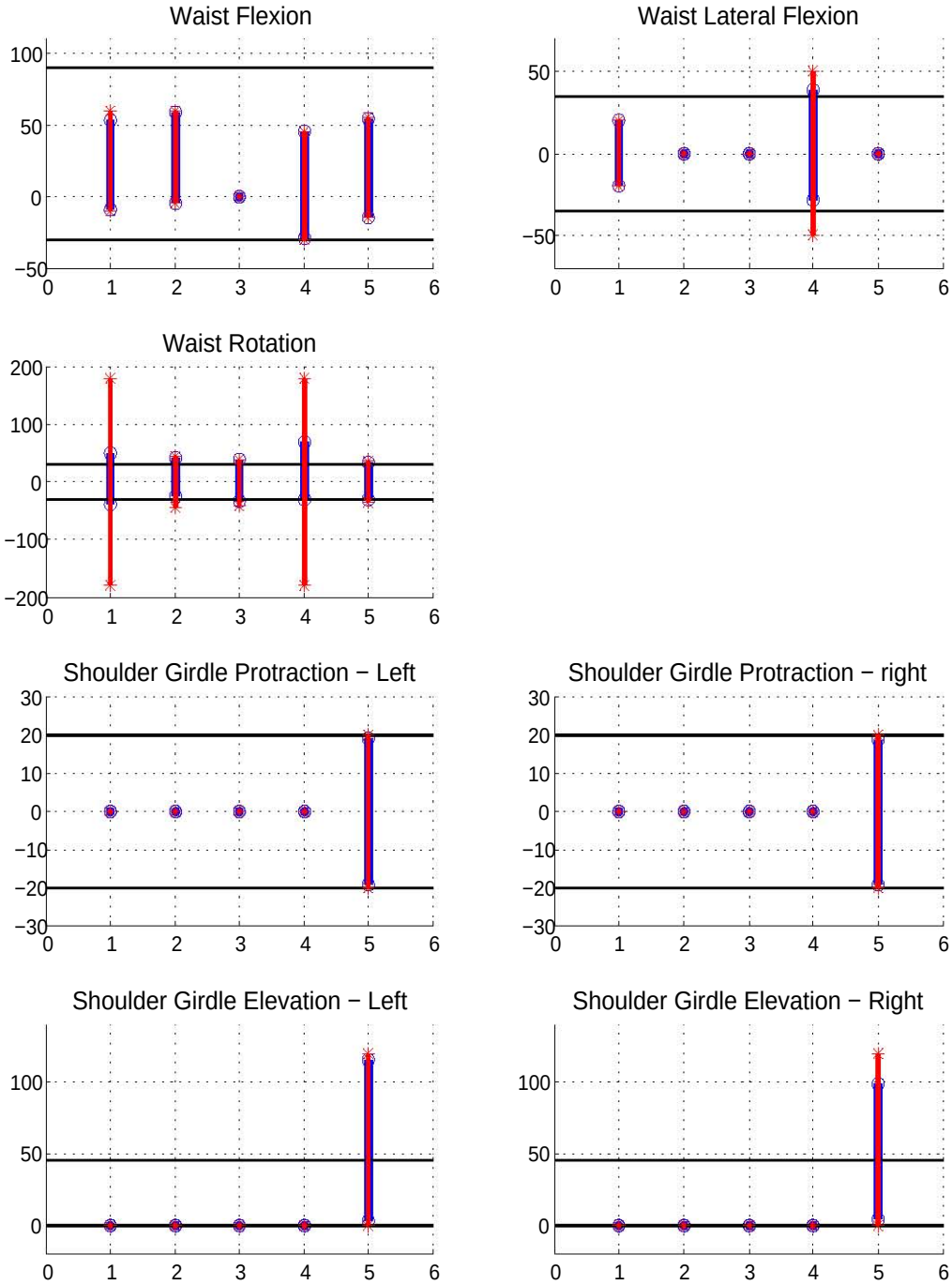


Figure 6.27: Torso joint ranges used. Key: $*$ - joint limit, o - joint range used. 1 - ARMAR, 2 - HRP, 3 - SURALP, 4 - WABIAN, 5 - WE4RII.

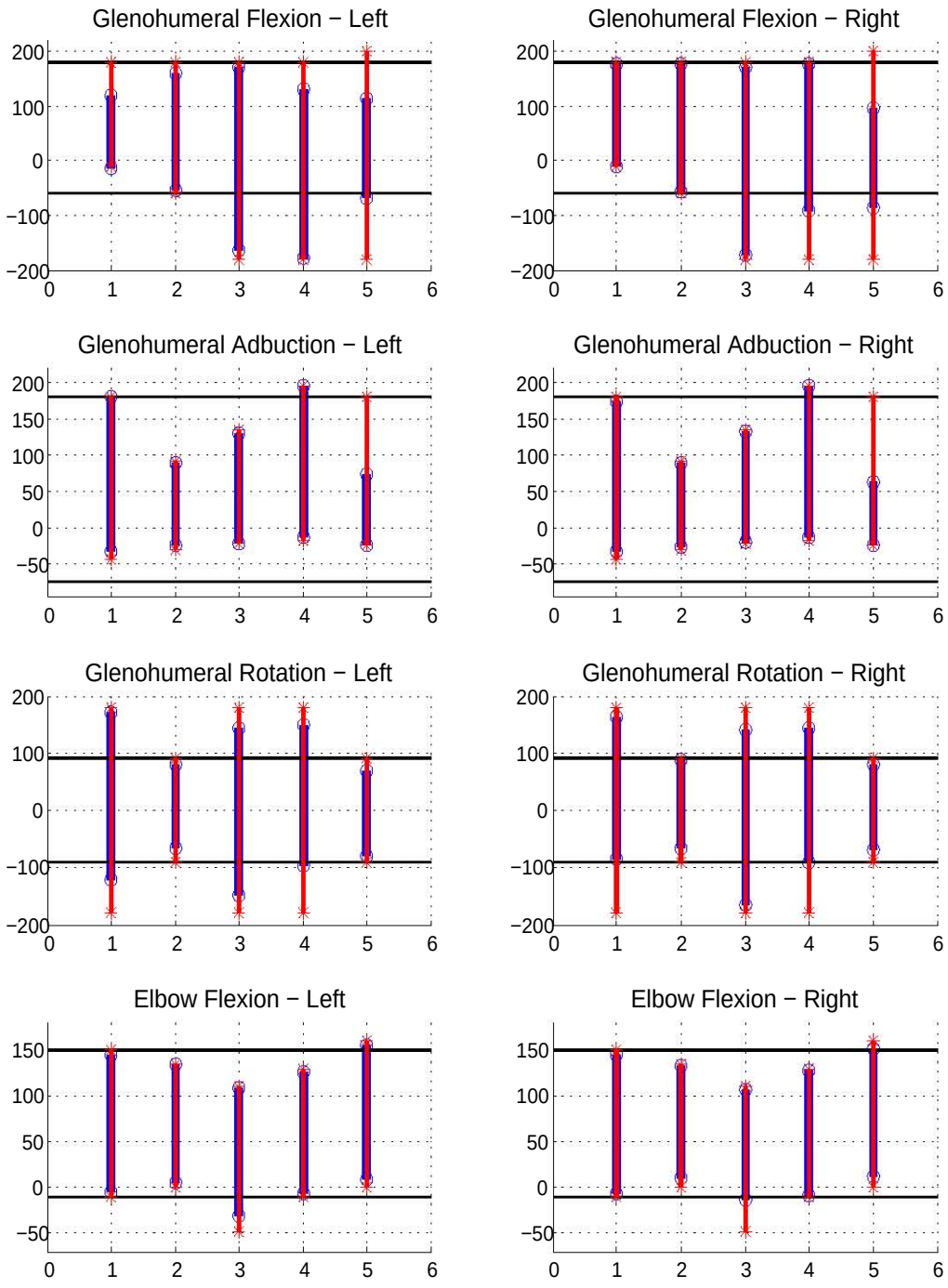


Figure 6.28: Arm joint ranges used. Key: $*$ - joint limit, o - joint range used. 1 - ARMAR, 2 - HRP, 3 - SURALP, 4 - WABIAN, 5 - WE4RII.

in order to reach high arm positions, part of the human arm's glenohumeral motion is actually aided by the motion of the shoulder girdle. AMAR and HRP both with limited glenohumeral extension, use most or all of their glenohumeral flexion and extension range. All the robot's except WE4RII use their full glenohumeral abduction joint range. All the robots have limited glenohumeral adduction, and use the full range. For WE4RII, the limited adduction has a large influence on the arm errors. WE4RII however, uses only about half its abduction range due to having a shoulder girdle which aids in positioning the arm.

Most of the humanoids have large glenohumeral rotation ranges which are mostly used in trying to compensate for errors in the arm position causes by sternum or clavicle position errors. WE4RII and HRP have a range similar to that of a human and, while using most of the range, the joint limits are not reached. Elbow hyperextension is mostly unused. Where elbow hyperextension is used, it is to try and compensate for the arm errors caused by waist and shoulder girdle joints, however its influence is negligible. Errors due to limited elbow flexion are noted.

### 6.2.2 With self collision avoidance

Figure 6.29 illustrates the results of self collision avoidance. As shown in figure 6.30, avoiding collisions results in an increase in the position error mean and standard deviation. Each humanoid robot successfully avoids collisions of the arms with the torso. As sufficient information to locate the head is not available, collisions with the head are not taken into account. As the self collision avoidance method used does not take into account the desired arm posture, it sometimes results in the arm moving far from the desired configuration. The effect is most noticeable with ARMAR, who's wrist standard deviation increases significantly.

Table 6.6 shows the number of collisions for the arms with the torso of each humanoid. There are a number of different reasons why collisions occur. The first is due to the scaling of lengths from the human motion to the robot dimensions. The next is determined by how well the robot reaches the desired postures. If the robot does not reach the required posture, the posture attained could result in collisions or could manage to avoid collisions that would otherwise have occurred.

In general collisions of the upper arm are less than collisions of the lower arm. This is due to the larger range of positions the lower arm can reach. Collisions with the lower torso are generally less than collisions with the upper torso. This is because while the upper torso is within the workspace of both upper and lower

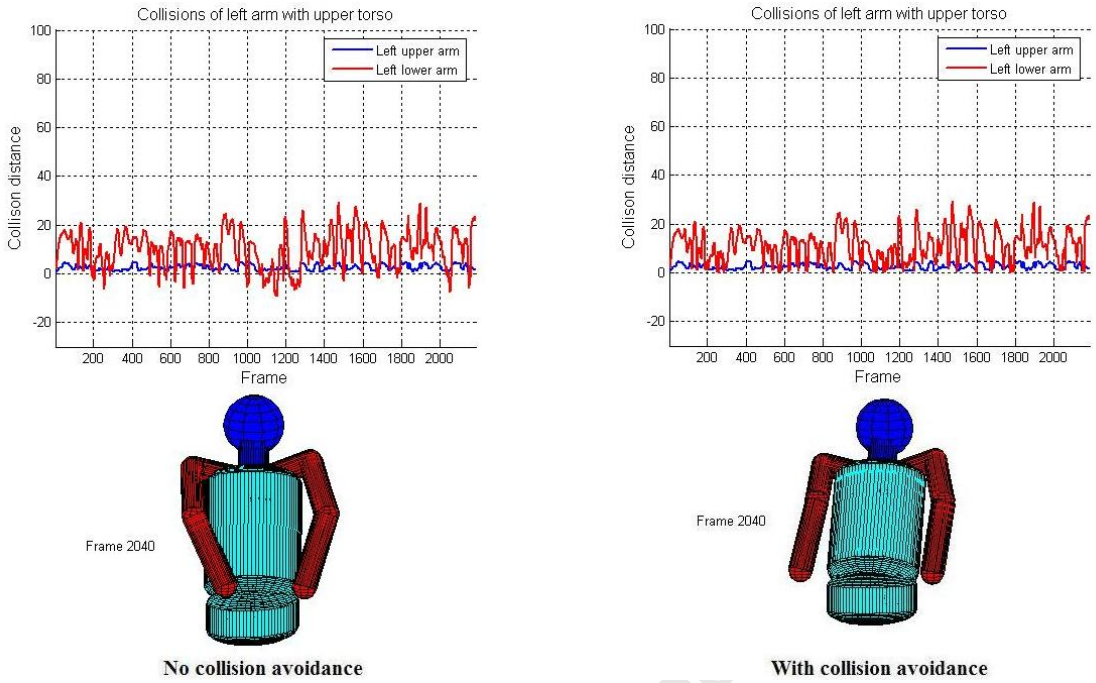


Figure 6.29: Self collision avoidance results (WE4RII).

| | Lower Arm | | Upper Arm | |
|---|---|---|---|---|
| Humanoid | Upper Torso | Lower Torso | Upper Torso | Lower Torso |
| ARMAR | 665 | 167 | 447 | 0 |
| HRP | 798 | 397 | 641 | 22 |
| SURALP | 767 | 31 | 29 | 0 |
| WABIAN | 497 | 45 | 0 | 0 |
| WE4RII | 388 | 43 | 0 | 0 |

Table 6.6: Humanoid self collisions for dance.

arms, the lower torso is largely outside the workspace of the upper arm. HRP has the highest number of collisions overall. It has very high collisions with the lower torso in comparison to the other humanoids as its lower torso is much longer due to the waist joint being positioned in the middle of the spine. WE4RII and WABIAN have the lowest collisions. They are the two robots with the best motion following and have similar upper body dimensions. WABIAN, however has the larger torso depth, which may account for the larger number of collisions. WE-4RII's shoulder girdle might also influence its lower number of collisions, as one of the functions of a shoulder girdle is to prevent collisions of the arm with the torso.

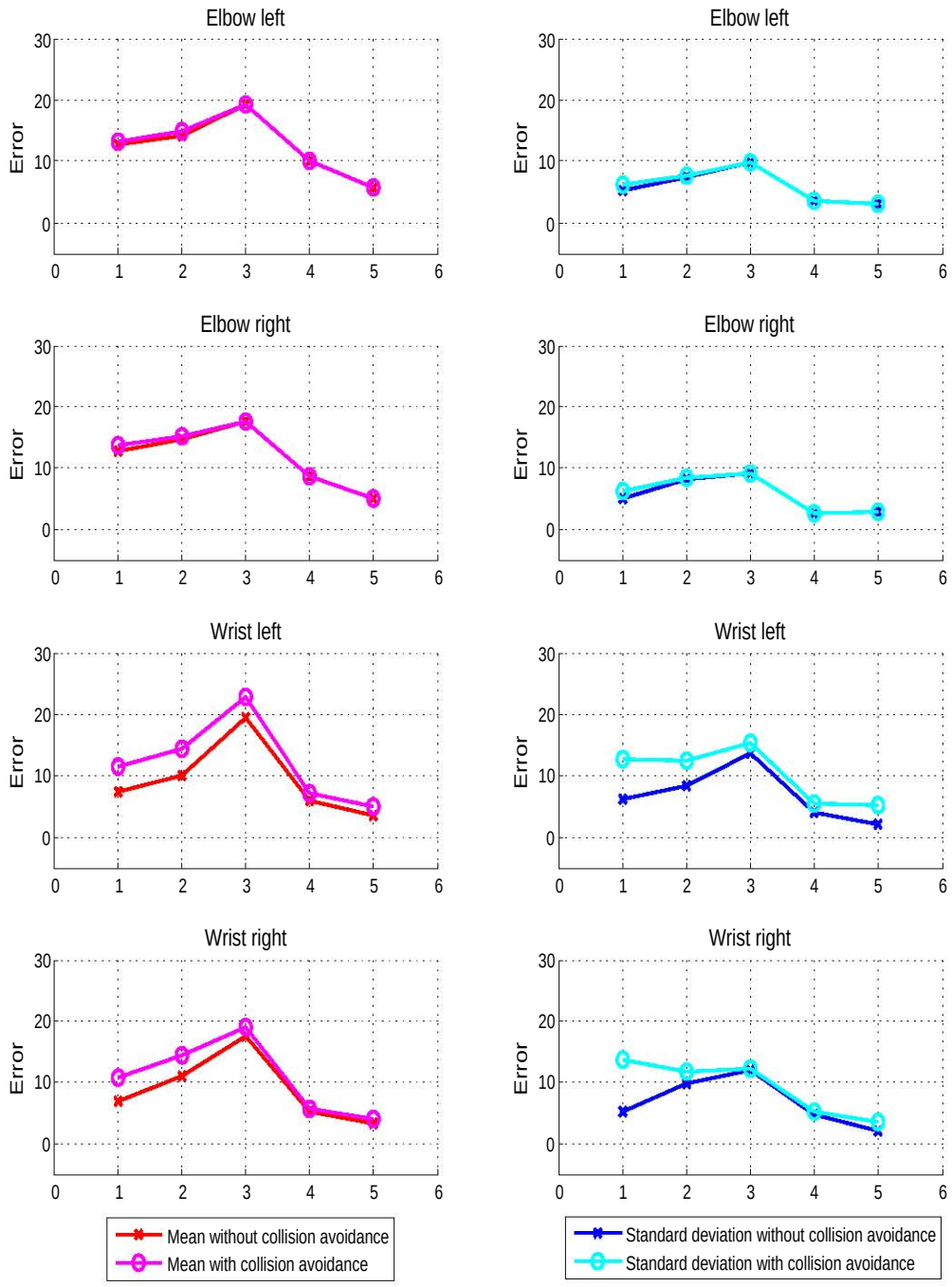


Figure 6.30: Position error mean and standard deviation with collision avoidance. Key: 1 - ARMAR, 2 - HRP, 3 - SURALP, 4 - WABIAN, 5 - WE4RII.

## 6.3 Summary

Five humanoids are studied to determine the factors that influence human motion imitation. Factors that affect the motion following capabilities of the humanoids include; the lack of a shoulder girdle; the lack of some waist DOFs; limited range of joints; glenohumeral joint singularities. WE4RII has the best motion performance due to having two waist DOFs and due to the presence of a shoulder girdle. SURALP has the worst motion performance due to having only a single waist DOF and no shoulder girdle. Self collisions decrease the motion performance of the humanoids.

# Chapter 7

# Conclusions and Future Work



This thesis set out to determine how well humanoid robots can imitate human motion obtained from motion capture data. The aim was to model humanoid upper bodies and to determine the characteristics of the humanoid structure that affect its motion performance. Five humanoid robots were therefore modeled and compared. The resulting conclusions and future work stemming from this study are discussed in this chapter.

## 7.1 Conclusions

The objectives of this thesis were to; 1) Model five different humanoid robot upper body structures; 2) Use the humanoid upper body models to imitate a captured human dance; 3) Compare the motion imitation abilities of the humanoid upper body models. The humanoid robots used in this study were therefore modeled to determine the resulting pose of each robot given human motion capture data as an input. Methods to estimate missing motion capture data and to determine self collisions of the humanoid body were also developed. Differences in performance of each robot were observed. Differences were due to a number of factors, including; the number of joints, the range of joint motion and self collisions of the humanoids.

### 7.1.1 Modeling of humanoid upper body structures

Five different serial structured humanoid robots were used in this study. The humanoids used had different numbers of degrees of freedom (DOF's) and different

ranges of joint motion. This enabled comparison of the effects of the waist, shoulder girdle and arm on the overall upper body motion of the humanoids. Each robot was modeled as a chain of links connected by individual joints, using the Denavit-Hartenburg convention. The pose of each link was then computed using the transformation matrix obtained for each link. This then combined to give the pose for the whole upper body.

To model self collisions of the humanoid limbs with the body, a self collision detection scheme based on elliptical capsules was formulated. The torso of each robot was modeled using an elliptical capsule as a collision detection bounding volume. The limbs were modeled using circular capsules as collision detection bounding volumes. The distance between each capsule was used to determine whether possible collisions occurred. Where collisions were detected, the motion of the arm was adjusted to move the arms away from the collision point. The self collision avoidance used, however, did not take into account the desired pose of the humanoid. The self collision detection scheme formulated was simple while it provided a good fit to the humanoid form for each robot used. Using elliptical capsules as bounding volumes for self collision detection compared favorably, in terms of number of faces required and volume estimation, to existing bounding volume representations found in literature. The formulation was successfully applied to the five different humanoids. Self collision free motion was attained for each humanoid.



### 7.1.2 Transferring human motion to humanoids

Human motion capture data of a dance routine, which had a wide range of upper body movements, was used for motion imitation in this study. To account for missing information from the motion capture data set used, a sternum position estimation method was formulated. The formulation was tested using a second motion capture data set that contained sternum position information, though this data set had limited upper body movements. The low error in the estimate of the sternum position when compared to the actual sternum position shows that the sternum position formulation developed in this thesis is suitable for use on humanoid robots when actual sternum marker information is missing.

Human motion was transfered to the humanoids using differential inverse kinematics. The Damped Least Squares (DLS) Jacobian was used for the inverse kinematics. A weighting factor was added to the inverse kinematics to account for joint limit constraints. The method works well for high DOF robots such as those used in this study. The limitations of the method were due to it's incremental

nature which computes the robot's pose at a particular time instant based on the previous pose. This limitation led to some of the humanoids becoming stuck at certain incorrect postures even though other feasible postures could be attained.

### 7.1.3 Comparison of human motion imitation of humanoids

Humanoid robots were compared to determine how the waist, shoulder girdle and arm DOFs and their range of motion affect human motion imitation. Of the five humanoids studied, WE-4RII had the best motion performance largely due to the presence of a shoulder girdle. This was despite WE-4RII only having two waist DOFs. The rest of the humanoids had no shoulder girdle which limited their performance. WABIAN had the second best performance due mainly to its three waist DOFs and high range of waist motion. This was followed by ARMAR again with three waist DOFs. ARMAR's waist motion range was however limited in comparison with WABIAN. HRP was next in motion performance, having only two waist DOF's and limited arm motion range. SURALP had the worst performance, having only one waist DOF. Self collisions were shown to decrease the accuracy of motion imitation for each of the robots.

The waist DOFs were highlighted as important to human motion imitation. Having three waist DOFs greatly improves the motion imitation of humanoids, as illustrated by the results of WABIAN and ARMAR. Two waist DOFs can also give acceptable motion imitation results as shown by HRP's motion results. As shown by SURALP, a single waist rotation joint results in very poor motion imitation. As SURALP was the only humanoid with only one waist DOF (waist rotation), the difference resulting from a single waist flexion or waist lateral flexion joint could not be determined. The position of the waist joint is important as shown by HRP whose results are affected by having the waist at the center of the spine. Having the waist joints close to the hip line also decreases self collisions of the arms with the lower body.

The shoulder girdle was shown to be a highly significant factor in motion imitation of humanoids. Having a shoulder girdle greatly improves the motion performance of the humanoid. The shoulder girdle is also capable of compensating significantly for the lack of a waist lateral flexion joint. As seen by the results of the humanoids with no shoulder girdles, while the glenohumeral and elbow joints can to some extent compensate for the lack of a shoulder girdle, the compensation effect is not very large.

The glenohumeral abduction joint singularity also worsens the motion imitation results. As all the humanoids had similar glenohumeral joints, the effects of a different type of glenohumeral joint cannot be determined. As none of the humanoids had different arm DOFs, the potential influences of more arm DOF's was not determined. However based on the how the range of each arm joint influences the arm motion, it can be concluded that removing any of the arm joints would have a detrimental effect.

Based on the results, for a humanoid to successfully imitate human motion with high accuracy the following are therefore desirable:

1. A three DOF waist joint,
2. A two DOF shoulder girdle for each arm,
3. At least three DOF for the glenohumeral joints,
4. Singularity free glenohumeral joints,
5. One DOF elbow joints,
6. A waist joint situated close to the hip-line.

The range of motion of each humanoid joint also affected the motion performance of each humanoid. Having a very large range of motion of some joints, as shown by SURALP and WABIAN's very high glenohumeral extension range, was not necessarily a benefit for motion imitation. The very high glenohumeral extension lead to the robot becoming stuck while trying to attain certain postures. However, a range of motion that is much lower than that of a human decreases the motion imitation capabilities as shown by the limited waist extension and limited glenohumeral extension of some of the humanoids. For humanoids with shoulder girdles, the influence of the adduction range on the upper arm errors shows that increased adduction would be beneficial for human motion imitation. If the shoulder girdle is not situated at the sternum location, higher elevation and protraction are needed as shown by WE4RII. For WE4RII the presence of a shoulder girdle meant that a lower range of glenohumeral flexion was sufficient for human motion imitation. Based on the motion imitation results, for a humanoid with a shoulder girdle, the acceptable range of motion for joints are summarised in table 7.1.

Table 7.1: Humanoid recommended joint range of motion.

| | Joint range (degrees) | |
|---|---|---|
| DOF | Minimum | Maximum |
| WT Flexion | −30 | 60 |
| WT Lateral Flexion | −35 | 35 |
| WT Rotation | −30 | 30 |
| SG Protraction | −30 | 30 |
| SG Elevation | 0 | 90 |
| GH Flexion | −90 | 120 |
| GH Abduction | −90 | 120 |
| GH Rotation | −90 | 90 |
| EL flexion | 0 | 150 |

Key for abbreviations: WT - waist, SG - shoulder girdle, GH - glenohumeral joint, EL - elbow joint.



## 7.2 Future work

Future work stemming from this study includes development of an effective self collision avoidance method based on elliptical capsule self collision detection. The self collision avoidance method used thus far does not attempt to keep the humanoid close to the desired posture while avoiding self collisions. A constraint keeping the self collision free posture as close as possible to the desired posture would improve performance. Further tests incorporating self collision avoidance can then be carried out and the effects of the shoulder girdle on self collisions can be fully determined.

The influence of velocities and accelerations of the humanoid body segments on human motion imitation are also to be further investigated. Motion imitation including not only the position, but the orientation of the lower arm as an input is also to be examined. Another area of future work is to investigate the influence of different DOF glenohumeral joints on the humanoid motion imitation. Finally, a real life comparison of the motion imitation of the humanoids, instead of their simulated models, is another area of further study.

# Appendix A

# Presented and published papers

The following papers were presented and published based on the work carried out in this thesis.

## A.1 Paper 1

### Title

A model of the humanoid body for self collision detection based on elliptical capsules.



### Authors

Chioniso Dube, Mohohlo Tsoeu and Jonathan Tapson.

### Proceedings

This paper appears in the proceedings of the 2011 IEEE International Conference on Robotics and Biomimetics (ROBIO).

### Abstract

This paper presents a self collision detection scheme for humanoid robots using elliptical and circular capsules as bounding volumes. A capsule is defined as an elliptical or circular cylinder capped with ellipsoids or spheres respectively. The humanoid body is modeled using elliptical capsules, while the moving segments, i.e. arms and legs, of the humanoid are modeled using circular capsules. This collision detection model provides a good fit to the humanoid body shape while being simple to implement. A case study of the self collision free workspace of the humanoid arm is then presented to illustrate the effectiveness of the collision detection scheme.

## A.2 Paper 2

### Title

Kinematics design and human motion transfer for a humanoid service robot arm.

### Authors

Chioniso Dube and Jonathan Tapson.

### Proceedings

This paper appears in the proceedings of the 2009 Robotics and Mechatronics Conference of South Africa.

### Abstract

This paper focuses firstly, on the kinematics structure required for a humanoid service robot arm and secondly, on transferring human motion obtained from visual motion capture to the humanoid arm. The kinematics structure of a ten Degree of Freedom (DOF) humanoid arm which has a two DOF shoulder girdle and has a four DOF glenohumeral joint is presented. A method of obtaining the sternum position, which forms the movement reference frame for the ten DOF arm, is formulated from human motion capture data. The method is based on clavicle and spine workspaces. Results show that the sternum formulation corresponds well to the actual sternum position.

# Appendix B

# Ethics Form

## EBE Faculty: Assessment of Ethics in Research Projects

Any person planning to undertake research in the Faculty of Engineering and the Built Environment at the University of Cape Town is required to complete this form before collecting or analysing data. When completed it should be submitted to the supervisor (where applicable) and from there to the Head of Department. If any of the questions below have been answered YES, and the applicant is NOT a fourth year student, the Head should forward this form for approval by the Faculty EIR committee: submit to Ms Zulpha Geyer (Zulpha.Geyer@uct.ac.za; Chem Eng Building. Ph 021 650 4791). Students must include a copy of the completed form with the thesis when it is submitted for examination.

---

Name of Principal Researcher/Student: Chioniso Dube  Department: Electrical Engineering

If a Student:  Degree: MSc Elec Eng  Supervisor: M. S. Tsoeu

If a Research Contract indicate source of funding/sponsorship:

Research Project Title: Modelling of the humanoid upper body for human motion imitation

**Overview of ethics issues in your research project:**

| | | |
|---|---|---|
| **Question 1: Is there a possibility that your research could cause harm to a third party (i.e. a person not involved in your project)?** | YES | NO X |
| **Question 2: Is your research making use of human subjects as sources of data?** If your answer is YES, please complete Addendum 2. | YES | NO X |
| **Question 3: Does your research involve the participation of or provision of services to communities?** If your answer is YES, please complete Addendum 3. | YES | NO X |
| **Question 4: If your research is sponsored, is there any potential for conflicts of interest?** If your answer is YES, please complete Addendum 4. | YES | NO X |

If you have answered YES to any of the above questions, please append a copy of your research proposal, as well as any interview schedules or questionnaires (Addendum 1) and please complete further addenda as appropriate.

**I hereby undertake to carry out my research in such a way that**

- there is no apparent legal objection to the nature or the method of research; and
- the research will not compromise staff or students or the other responsibilities of the University;
- the stated objective will be achieved, and the findings will have a high degree of validity;
- limitations and alternative interpretations will be considered;
- the findings could be subject to peer review and publicly available; and
- I will comply with the conventions of copyright and avoid any practice that would constitute plagiarism.

Signed by:

| | Full name and signature | Date |
|---|---|---|
| Principal Researcher/Student: | Chioniso Dube | 17/02/2012 |

This application is approved by:

| | | |
|---|---|---|
| Supervisor (if applicable): | | 20/02/2012 |
| HOD (or delegated nominee): Final authority for all assessments with NO to all questions and for all undergraduate research. | | |
| Chair : Faculty EIR Committee For applicants other than undergraduate students who have answered YES to any of the above questions. | | |

# References


[1] Y. Kuroki, M. Fujita, T. Ishida, K. Nagasaka, and J. Yamaguchi, "A small biped entertainment robot exploring attractive applications," in *Robotics and Automation, 2003. Proceedings. ICRA '03. IEEE International Conference on*, vol. 1, pp. 471 – 476 vol.1, Sept. 2003.

[2] "SDR-4X QRIO product design." Available: `http://www.sony.net/Fun/design/history/product/2000/sdr-4x.html`. [Online; last visited January 2010].

[3] E. Guizzo, "How to make a robot dance." Available: `http://spectrum.ieee.org/automaton/robotics/humanoids/how-to-make-a-robot-dance`, Nov. 2010. [Online; last visited May 2011].

[4] C. Burgar, P. Lum, A. Scremin, S. Garber, H. Van der Loos, D. Kenney, and P. Shor, "Robot-assisted upper-limb therapy in acute rehabilitation setting following stroke: Department of veterans affairs multisite clinical trial," *Journal of Rehabilitation Research & Development*, vol. 48, pp. 445–458, 2011.

[5] H. Krebs, B. Volpe, M. Aisen, and N. Hogan, "Increasing productivity and quality of care : Robot-aided neuro-rehabilitation," *Journal of Rehabilitation Research and Development*, vol. 24, pp. 639–652, Nov. / Dec. 2000.

[6] R. Colombo, F. Pisano, S. Micera, A. Mazzone, C. Delconte, M. Chiara Carrozza, P. Dario, and G. Minuco, "Robotic techniques for upper limb evaluation and rehabilitation of stroke patients," *IEEE Transactions on Neural Systems and Rehabilitation Engineering*, vol. 13, pp. 311–324, 2005.

[7] T. Sugar, J. He, E. Koeneman, J. Koeneman, R. Herman, H. Huang, R. Schultz, D. Herring, J. Wanberg, S. Balasubramanian, P. Swenson, and J. Ward, "Design and control of RUPERT: a device for robotic upper extremity repetitive therapy," *Neural Systems and Rehabilitation Engineering, IEEE Transactions on*, vol. 15, pp. 336–346, Sept. 2007.

[8] V. J. Traver, A. P. del Pobil, and M. Perez-Francisco, "Making service robots human-safe," in *Intelligent Robots and Systems, 2000. (IROS 2000). Proceedings. 2000 IEEE/RSJ International Conference on*, vol. 1, pp. 696–701, 2000.

[9] S.-S. Yoon, S. Kang, S.-J. Kim, Y.-H. Kim, M. Kim, and C.-W. Lee, "Safe arm with mr-based passive compliant joints and visco-elastic covering for service robot applications," in *Intelligent Robots and Systems, 2003. (IROS 2003). Proceedings. 2003 IEEE/RSJ International Conference on*, vol. 3, pp. 2191–2196, Oct. 2003.

[10] P. Dario, E. Guglielmelli, V. Genovese, and M. Toro, "Robot assistants: Applications and evolution," *Robotics and Autonomous Systems*, vol. 18, no. 12, pp. 225 – 234, 1996.

[11] O. Khatib, "Mobile manipulation: The robotic assistant," *Robotics and Autonomous Systems*, vol. 26, no. 2, pp. 175–183, 1999.

[12] B. Graf, M. Hans, and R. D. Schraft, "Care-O-bot II-Development of a next generation robotic home assistant," *Autonomous Robots*, vol. 16, pp. 193–205, Mar. 2004.

[13] P. Dario, E. Guglielmelli, and C. Laschi, "Humanoids and personal robots: Design and experiments," *Journal of Robotic Systems*, vol. 18, no. 12, pp. 673–690, 2001.

[14] K. Tsui, H. Yanco, D. Kontak, and L. Beliveau, "Development and evaluation of a flexible interface for a wheelchair mounted robotic arm," in *Proceedings of the 3rd ACM/IEEE international conference on Human robot interaction*, HRI '08, (New York, NY, USA), pp. 105–112, ACM, 2008.

[15] K. M. Tsui, D. Kim, A. Behal, D. Kontak, and H. A. Yanco, "I want that: Human-in-the-loop control of a wheelchair-mounted robotic arm," *Journal of Applied Bionics and Biomechanics*, vol. 8, p. 127147, 2011.

[16] W.-K. Song, H. Lee, and Z. Bien, "Kares: Intelligent wheelchair-mounted robotic arm system using vision and force sensor," *Robotics and Autonomous Systems*, vol. 28, no. 1, pp. 83 – 94, 1999.

[17] N. Pollard, J. Hodgins, M. Riley, and C. Atkeson, "Adapting human motion for the control of a humanoid robot," in *Robotics and Automation, 2002. Proceedings. ICRA '02. IEEE International Conference on*, vol. 2, pp. 1390–1397, 2002.

[18] M. Riley and C. G. Atkeson, "Methods for motion generation and interaction with a humanoid robot: Case studies of dancing and catching," in *Proc. 2000 Workshop on Interactive Robotics and Entertainment, Robotics Inst., Carnegie Mellon Univ*, pp. 35–42, 2000.

[19] S. Nakaoka, A. Nakazawa, K. Yokoi, H. Hirukawa, and K. Ikeuchi, "Generating whole body motions for a biped humanoid robot from captured human dances," in *Robotics and Automation, 2003. Proceedings. ICRA '03. IEEE International Conference on*, vol. 3, pp. 3905–3910, Sept. 2003.

[20] A. Nakazawa, S. Nakaoka, K. Ikeuchi, and K. Yokoi, "Imitating human dance motions through motion structure analysis," in *Intelligent Robots and Systems, 2002. IEEE/RSJ International Conference on*, vol. 3, pp. 2539–2544, 2002.

[21] J. Hamill and K. M. Knutzen, *Biomechanical Basis of Human Motion*. Baltimore: Williams and Wilkins, 1995.

[22] K. Luttgens and K. F. Wells, *Kinesiology : Scientific Basis of Human Motion*. Philadelphia: Saunders College Publishing, 6th ed., 1982.

[23] S. Pheasant, *Bodyspace: Anthropometry, Ergonomics and Design*. London and Philadelphia: Taylor and Francis Ltd, 1986.

[24] "Antagonistic muscles." Available: `http://www.arrowvale.worcs.sch.uk/sportscollege/muscles.htm`. [Online; last visited January 2010].

[25] R. Van Ham, *Compliant actuation for biologically inspired bipedal walking robots*. PhD thesis, Vrijie University Brussel, 2006.

[26] M. Okada, Y. Nakamura, and S. Hoshino, "Development of the cybernetic shoulder-a three DOF mechanism that imitates biological shoulder-motion," in *Intelligent Robots and Systems, 1999. IROS '99. Proceedings. 1999 IEEE/RSJ International Conference on*, vol. 1, pp. 543–548, 1999.

[27] "ASIMO the Honda humanoid robot." American Honda Motor Co. Inc. Corporate Affairs & Communication, 2003. [Technical Information].

[28] K. Kaneko, F. Kanehiro, S. Kajita, H. Hirukawa, T. Kawasaki, M. Hirata, K. Akachi, and T. Isozumi, "Humanoid robot HRP-2," in *Robotics and Automation, 2004. Proceedings. ICRA '04. 2004 IEEE International Conference on*, vol. 2, pp. 1083–1090, Apr. 2004.

[29] A. Albers, S. Brudniok, J. Ottnad, C. Sauter, and K. Sedchaicharn, "Upper body of a new humanoid robot - the design of ARMAR III," in *Humanoid Robots, 2006 6th IEEE-RAS International Conference on*, pp. 308–313, Dec. 2006.

[30] T. Asfour, P. Azad, N. Vahrenkamp, K. Regenstein, A. Bierbaum, K. Welke, J. Schrder, and R. Dillmann, "Toward humanoid manipulation in human-centred environments," *Robotics and Autonomous Systems*, vol. 56, no. 1, pp. 54–65, 2008.

[31] S. Shirata, A. Konno, and M. Uchiyama, "Design and development of a light-weight biped humanoid robot Saika-4," in *Intelligent Robots and Systems, 2004. (IROS 2004). Proceedings. 2004 IEEE/RSJ International Conference on*, vol. 1, pp. 148–153, Sep / Oct. 2004.

[32] I.-W. Park, J.-Y. Kim, J. Lee, and J.-H. Oh, "Mechanical design of humanoid robot platform khr-3 (kaist humanoid robot 3: Hubo)," in *Humanoid Robots, 2005 5th IEEE-RAS International Conference on*, pp. 321–326, Dec. 2005.

[33] T. Morita and S. Sugano, "Development and evaluation of seven DOF MIA ARM," in *Robotics and Automation, 1997. Proceedings., 1997 IEEE International Conference on*, vol. 1, pp. 462–467, Apr. 1997.

[34] R. Tadakuma, Y. Asahara, H. Kajimoto, N. Kawakami, and S. Tachi, "Development of anthropomorphic multi-d.o.f master-slave arm for mutual telexistence," *Visualization and Computer Graphics, IEEE Transactions on*, vol. 11, pp. 626–636, Nov / Dec 2005.

[35] W. Bluethmann, R. Ambrose, M. Diftler, S. Askew, E. Huber, M. Goza, F. Rehnmark, C. Lovchik, and D. Magruder, "Robonaut: A robot designed to work with humans in space," *Autonomous Robots*, vol. 14, pp. 179–197, 2003.

[36] B. Rooks, "The harmonious robot," *Industrial Robot: An International Journal*, vol. 33, pp. 125–130, 2006.

[37] W. Townsend and A. Guertin, "Teleoperator slave - WAM design methodology," *Industrial robot: An international Journal*, vol. 26, pp. 167–177, 1999.

[38] D. Tsetserukou, R. Tadakuma, H. Kajimoto, N. Kawakami, and S. Tachi, "Intelligent variable joint impedance control and development of a new whole-sensitive anthropomorphic robot arm," in *Computational Intelligence*

*in Robotics and Automation, 2007. CIRA 2007. International Symposium on*, pp. 338–343, June 2007.

[39] S. Chiaverini, G. Oriolo, and I. Walker, "Kinematically redundant manipulators," in *Springer Handbook of Robotics*, pp. 245–268, Springer-Verlag, 2008.

[40] H. Miwa, K. Itoh, D. Ito, H. Takanobu, and A. Takanishi, "Design and control of 9-DOFs emotion expression humanoid arm," in *Robotics and Automation, 2004. Proceedings. ICRA '04. 2004 IEEE International Conference on*, vol. 1, pp. 128–133, Apr. / May 2004.

[41] M. Zinn, B. Roth, O. Khatib, and J. Salisbury, "A new actuation approach for human friendly robot design," *The International Journal of Robotics Research*, vol. 23, pp. 379–398, 2004.

[42] A. Edsinger-Gonzales and J. Weber, "Domo: a force sensing humanoid robot for manipulation research," in *Humanoid Robots, 2004 4th IEEE/RAS International Conference on*, vol. 1, pp. 273–291, Nov. 2004.

[43] H. Maeda, H. Nagai, and T. Nakamura, "Development of a 6-DOF manipulator actuated with a straight-fiber-type artificial muscle," in *Intelligent Robots and Systems, 2009. IROS 2009. IEEE/RSJ International Conference on*, pp. 607–612, Oct. 2009.

[44] B. Tondu, S. Ippolito, and J. Guiochet, "A seven-degrees-of-freedom robot arm driven by pneumatic artificial muscles for humanoid robots," *The International Journal of Robotics Research*, vol. 24, pp. 257–274, 2005.

[45] K. Hoshino and W. Krishantha, "Calligraphic motion by humanoid robot arm using air cylinder actuators as endoskeletons," in *Mechatronics, ICM2007 4th IEEE International Conference on*, pp. 1–6, May 2007.

[46] K. Kaneko, S. Kajita, K. Yokoi, V. Hugel, P. Blazevic, and P. Coiffet, "Design of LRP humanoid robot and its control method," in *Robot and Human Interactive Communication, 2001. Proceedings. 10th IEEE International Workshop on*, pp. 556 –561, 2001.

[47] "Humanoid robot project - SURALP." Available: `http://people.sabanciuniv.edu/erbatur/humanoid%20robot%20project.html`. [Online; last visited January 2012].

[48] Y. Ogura, H. Aikawa, K. Shimomura, A. Morishima, H. Lim, and A. Takanishi, "Development of a new humanoid robot WABIAN-2," in *Robotics and*

*Automation, 2006. ICRA 2006. Proceedings 2006 IEEE International Conference on*, pp. 76–81, May 2006.

[49] N. Tsakarakis, G. Metta, G. Sandini, D. Vernon, R. Beira, F. Becchi, L. Righetti, J. Santos-Victor, A. Ijspeert, M. Carrozza, and D. Caldwell, "iCub - The Design and Realization of an Open Humanoid Platform for Cognitive and Neuroscience Research," *Journal of Advanced Robotics, Special Issue on Robotic platforms for Research in Neuroscience*, vol. 21, no. 10, pp. 1151–1175, 2007.

[50] A. Nagakubo, Y. Kuniyoshi, and G. Cheng, "ETL-Humanoid - a high-performance full body humanoid system for versatile actions," in *Intelligent Robots and Systems, 2001. Proceedings. 2001 IEEE/RSJ International Conference on*, vol. 2, pp. 1087–1092, 2001.

[51] G. Yang, W. Lin, M. Kurbanhusen, C. B. Pham, and S. H. Yeo, "Kinematic design of a 7-DOF cable-driven humanoid arm: a solution-in-nature approach," in *Advanced Intelligent Mechatronics. Proceedings, 2005 IEEE/ASME International Conference on*, pp. 444–449, 2005.

[52] K. Kawashima, N. Nakamura, T. Miyata, and T. Kagawa, "Application of robots using pneumatic artificial rubber muscles for operating construction machines," in *Intelligent Robots and Systems, 2003. (IROS 2003). Proceedings. 2003 IEEE/RSJ International Conference on*, vol. 3, pp. 3384–3389, Oct. 2003.

[53] M. Suzuki, T. Mayahara, and A. Ishizaka, "Redundant muscle coordination of a multi-DOF robot joint by online optimization," in *Advanced intelligent mechatronics, 2007 IEEE/ASME international conference on*, pp. 1–6, Sept. 2007.

[54] W. Chen, Q. Chen, J. Zhang, and S. Yu, "Kinematics control for a 7-DOF cable-driven anthropomorphic arm," in *Intelligent Robots and Systems, 2006 IEEE/RSJ International Conference on*, pp. 1650–1655, Oct. 2006.

[55] S. Mustafa, G. Yang, S. H. Yeo, and W. Lin, "Kinematic calibration of a 7-DOF self-calibrated modular cable-driven robotic arm," in *Robotics and Automation, 2008. ICRA 2008. IEEE International Conference on*, pp. 1288–1293, May 2008.

[56] I. Mizuuchi, T. Yoshikai, Y. Sodeyama, Y. Nakanishi, A. Miyadera, T. Yamamoto, T. Niemela, M. Hayashi, J. Urata, Y. Namiki, T. Nishino, and

M. Inaba, "Development of musculoskeletal humanoid kotaro," in *Robotics and Automation, 2006. ICRA 2006. Proceedings 2006 IEEE International Conference on*, pp. 82–87, May 2006.

[57] K. Kawashima, T. Sasaki, N. Nakamura, T. Miyata, N. Nakamura, M. Sekiguchi, and T. Kagawa, "Development of robot using pneumatic artificial rubber muscles to operate construction machinery," *Journal of Robotics and Mechatronics*, vol. 16, pp. 8–16, 2004.

[58] H. Ishiguro, "Scientific issues concerning androids," *The International Journal of Robotics Research*, vol. 26, pp. 105–117, 2007.

[59] M. Okada and Y. Nakamura, "Development of a cybernetic shoulder - a 3-DOF mechanism that imitates biological shoulder motion," *Robotics, IEEE Transactions on*, vol. 21, pp. 438–444, June 2005.

[60] J. Lenarcic, M. Stanisic, and V. Parenti-Castelli, "Kinematic design of a humanoid robotic shoulder complex," in *Robotics and Automation, 2000. Proceedings. ICRA '00. IEEE International Conference on*, vol. 1, pp. 27–32, 2000.

[61] Y. Sodeyama, T. Yoshikai, T. Nishino, I. Mizuuchi, and M. Inaba, "The designs and motions of a shoulder structure with a wide range of movement using bladebone-collarbone structures," in *Intelligent Robots and Systems, 2007. IROS 2007. IEEE/RSJ International Conference on*, pp. 3629–3634, Nov. 2007.

[62] M. M. Staniic and C. M. Goehler, "Reproducing human arm motion using a kinematically coupled humanoid shoulder-elbow complex," *Applied Bionics and Biomechanics*, vol. 5, no. 4, pp. 175–185, 2009.

[63] J. Lenarcic and N. Klopcar, "Positional kinematics of humanoid arms," *Robotica*, vol. 24, no. 01, pp. 105–112, 2006.

[64] I. Mizuuchi, Y. Nakanishi, Y. Sodeyama, Y. Namiki, T. Nishino, N. Muramatsu, J. Urata, K. Hongo, T. Yoshikai, and M. Inaba, "An advanced musculoskeletal humanoid kojiro," in *Humanoid Robots, 2007 7th IEEE-RAS International Conference on*, pp. 294–299, Dec. 2007.

[65] H. G. Marques, M. Jantsch, S. Wittmeier, O. Holland, C. Alessandro, A. Diamond, M. Lungarella, and R. Knight, "ECCE1: the first of a series of anthropomimetic musculoskeletal upper torsos," in *Humanoid Robots (Humanoids), 2010 10th IEEE-RAS International Conference on*, pp. 391–396, Dec. 2010.

[66] K. Erbatur, U. Seven, E. Taskran, O. Koca, M. Ylmaz, M. Unel, G. Kzltas, A. Sabanovic, and A. Onat, "SURALP: a new full-body humanoid robot platform," in *Intelligent Robots and Systems, 2009. IROS 2009. IEEE/RSJ International Conference on*, pp. 4949–4954, Oct. 2009.

[67] H. Miwa, K. Itoh, M. Matsumoto, M. Zecca, H. Takanobu, S. Rocella, M. Carrozza, P. Dario, and A. Takanishi, "Effective emotional expressions with expression humanoid robot WE-4RII: integration of humanoid robot hand RCH-1," in *Intelligent Robots and Systems, 2004. (IROS 2004). Proceedings. 2004 IEEE/RSJ International Conference on*, vol. 3, pp. 2203–2208, Sep / Oct 2004.

[68] A. Safonova, N. Pollard, and J. K. Hodgins, "Optimizing human motion for the control of a humanoid robot," in *2nd International Symposium on Adaptive Motion of Animals and Machines (AMAM2003)*, Mar. 2003.

[69] D. Matsui, T. Minato, K. F. MacDorman, and H. Ishiguro, "Generating natural motion in an android by mapping human motion," in *Humanoid Robots, Human-like Machines* (M. Hackel, ed.), InTech, 2007.

[70] M. Ruchanurucks and S. Nakaoka, "Offline and online trajectory generation with sequential physical constraints," in *Robotics and Biomimetics, 2008. ROBIO 2008. IEEE International Conference on*, pp. 578–583, Feb. 2009.

[71] B. Dariush, Y. Zhu, A. Arumbakkam, and K. Fujimura, "Constrained closed loop inverse kinematics," in *Robotics and Automation (ICRA), 2010 IEEE International Conference on*, pp. 2499 –2506, May 2010.

[72] B. Dariush, M. Gienger, A. Arumbakkam, Y. Zhu, B. Jian, K. Fujimura, and C. Goerick, "Online transfer of human motion to humanoids," *International Journal of Humanoid Robotics*, vol. 6, pp. 265–289, 2009.

[73] B. Dariush, M. Gienger, A. Arumbakkam, C. Goerick, Y. Zhu, and K. Fujimura, "Online and markerless motion retargeting with kinematic constraints," in *Intelligent Robots and Systems, 2008. IROS 2008. IEEE/RSJ International Conference on*, pp. 191 –198, Sept. 2008.

[74] J. Corrales, F. Candelas, and F. Torres, "Safe human-robot interaction based on dynamic sphere-swept line bounding volumes," *Robotics and Computer-Integrated Manufacturing*, vol. 27, pp. 177–185, 2011.

[75] F. Seto, K. Kosuge, and Y. Hirata, "Self-collision avoidance motion control for human robot cooperation system using RoBE," in *Intelligent Robots and*

*Systems, 2005. (IROS 2005). 2005 IEEE/RSJ International Conference on*, pp. 3143–3148, Aug. 2005.

[76] O. Stasse, A. Escande, N. Mansard, S. Miossec, P. Evrard, and A. Kheddar, "Real-time (self)-collision avoidance task on a HRP-2 humanoid robot," in *Robotics and Automation, 2008. ICRA 2008. IEEE International Conference on*, pp. 3200–3205, May 2008.

[77] K. Okada and M. Inaba, "A hybrid approach to practical self collision detection system of humanoid robot," in *Intelligent Robots and Systems, 2006 IEEE/RSJ International Conference on*, pp. 3952–3957, Oct. 2006.

[78] K. Okada, M. Inaba, and H. Inoue, "Real-time and precise self collision detection system for humanoid robots," in *Robotics and Automation, 2005. ICRA 2005. Proceedings of the 2005 IEEE International Conference on*, pp. 1060–1065, Apr. 2005.

[79] J. Kuffner, K. Nishiwaki, S. Kagami, Y. Kuniyoshi, M. Inaba, and H. Inoue, "Self-collision detection and prevention for humanoid robots," in *Robotics and Automation, 2002. Proceedings. ICRA '02. IEEE International Conference on*, vol. 3, pp. 2265 –2270, May 2002.

[80] H. Sugiura, M. Gienger, H. Janssen, and C. Goerick, "Real-time collision avoidance with whole body motion control for humanoid robots," in *Intelligent Robots and Systems, 2007. IROS 2007. IEEE/RSJ International Conference on*, pp. 2053–2058, Nov. 2007.

[81] H. Sugiura, M. Gienger, H. Janssen, and C. Goerick, "Real-time self collision avoidance for humanoids by means of nullspace criteria and task intervals," in *Humanoid Robots, 2006 6th IEEE-RAS International Conference on*, pp. 575–580, Dec. 2006.

[82] E. Larsen, S. Gottschalk, M. C. Lin, and D. Manocha, "Fast proximity queries with swept sphere volumes," Tech. Rep. TR99-018, Department of Computer Science, University of North Carolina.

[83] V. Jaggard, "Dancing robot to preserve japan's folk arts." Available: `http://news.nationalgeographic.com/news/2007/08/070814-dancing-robot.html`, Aug. 2007. [Online; last visited March 2012].

[84] M. Spong, S. Hutchinson, and M. Vidyasagar, *Robot Modelling and Control*. Wiley and Sons, 2006.

[85] L. Sciavicco and B. Siciliano, *Modelling and Control of Robot Manipulators*. London: Springer-Verlag, 2005.

[86] K. Waldron and J. Schmiedeler, "Kinematics," in *Springer Handbook of Robotics*, pp. 9–34, Springer-Verlag, 2008.

[87] C. Rocha, C. Tonetto, and A. Dias, "A comparison between the Denavit-Hartenberg and the screw-based methods used in kinematic modeling of robot manipulators," *Robotics and Computer-Integrated Manufacturing*, vol. 27, no. 4, pp. 723–728, 2011.

[88] C. Dube, M. Tsoeu, and J. Tapson, "A model of the humanoid body for self collision detection based on elliptical capsules," in *Robotics and Biomimetics (ROBIO), 2011 IEEE International Conference on*, pp. 2397–2402, Dec. 2011.

[89] "Evenly distributed points on a sphere." Available: `http://cgafaq.info/wiki/Evenly_distributed_points_on_sphere`. [Online; last visited January 2012].

[90] E. Rakhmanov, E. B. Saff, and Y. Zhou, "Minimal discrete energy on the sphere," *Mathematical Research Letters*, vol. 1, pp. 647–662, 1994.

[91] J. Ketchel and P. Larochelle, "Collision detection of cylindrical rigid bodies for motion planning," in *Robotics and Automation, 2006. ICRA 2006. Proceedings 2006 IEEE International Conference on*, pp. 1530–1535, May 2006.

[92] R. V. Patel, F. Shadpey, F. Ranjbaran, and J. Angeles, "A collision-avoidance scheme for redundant manipulators: Theory and experiments," *Journal of Robotic Systems*, vol. 22, no. 12, pp. 737–757, 2005.

[93] D. Eberly, "Distance from a point to an ellipse in 2D." Available: `http://www.geometrictools.com/Documentation/DistancePointToEllipse2.pdf`, Jan. 2004. [Online; last visited June 2011].

[94] D. Eberly, "Distance from a point to an ellipsoid." Available: `http://www.geometrictools.com/Documentation/DistancePointToEllipsoid.pdf`, Oct. 2008. [Online; last visited June 2011].

[95] "Biped humanoid robot group - WABIAN-2R (2006-)." Available: `http://www.takanishi.mech.waseda.ac.jp/top/research/wabian/index.htm`. [Online; last visited January 2012].

[96] K. Kaneko, F. Kanehiro, S. Kajita, K. Yokoyama, K. Akachi, T. Kawasaki, S. Ota, and T. Isozumi, "Design of prototype humanoid robotics platform for HRP," in *Intelligent Robots and Systems, 2002. IEEE/RSJ International Conference on*, vol. 3, pp. 2431–2436, 2002.

[97] H. Hirukawa, F. Kanehiro, K. Kaneko, S. Kajita, K. Fujiwara, Y. Kawai, F. Tomita, S. Hirai, K. Tanie, T. Isozumi, K. Akachi, T. Kawasaki, S. Ota, K. Yokoyama, H. Handa, Y. Fukase, J. ichiro Maeda, Y. Nakamura, S. Tachi, and H. Inoue, "Humanoid robotics platforms developed in HRP," *Robotics and Autonomous Systems*, vol. 48, no. 4, pp. 165–175, 2004.

[98] "Motion captue lab: System and data." Available: `http://accad.osu.edu/researchmain/research/motion_capture_lab/system_data.html`. [Online; last visited January 2010].

[99] C. Dube and J. Tapson, "Kinematics design and human motion transfer for a humanoid service robot arm," in *Robotics and Mechatronics Conference of South Africa*, Nov. 2009.